博士論文

Simulation of Magnetic Field Generation during the Collision of Counter-Streaming Plasmas

2000年3月

富山大学大学院　理工学研究科　エネルギー科学専攻

梶村好宏

博士論文

Simulation of Magnetic Field Generation during the Collision of Counter-Streaming Plasmas

梶村 好宏

Contents

Chapter 1

Introduction

1 GENERAL INTRODUCTION

1.1 Plasma Physics

'Plasma', the beginning of this word originates with Langmuir and Tonks who named 'Plasma Oscillation' when they discovered in 1920's the phenomena which charge particles oscillated in the arc discharge. Plasma corresponds to the ionized gas in widely meanings, but strictly speaking, (1) it includes negative and positive charged particles, (2) it keeps charge neutrality, (3) at least one kind of charged particles move randomly, (4) it is larger than debye length. Because of these characteristics, there are remarkable differences between plasma and normal gas. First the energy of the particles in plasma is so great to overcome the electric Coulomb force. One might think of the resulting assembly of positively and negatively charged particles as a gas. In fact the plasma is referred to as the fourth state of matter. Since plasma has collective properties and particle properties, we can see several interesting and complicated phenomena in plasma. The reason why the behavior of plasma is quite complicated consists in interaction between plasmas and electric and magnetic fields. In plasma, electric field and magnetic field coexist and interact with each other. The coexistence of them causes various kinds of instabilities which made behavior of plasma complicated.

Most of the visible matter in the universe exists as plasmas and we can see the plasma in a fluorescent light and an electric discharge of thunder. The study of plasma process is very old, but many phenomena are not yet fully understood or well explored. As to histories of plasma researches, Langmuir discovered the Plasma Oscillation in 1920 and Alfvén who is novelist, had been studying the space plasma and named 'Alfvén wave' as a wave propagating parallel to the magnetic field. Landou also got a novel prize in 1962, who is famous for Landou dumping. Landou dumping is one of the important basic physics of plasma, it occurs the resonance coupling between single particle and collective aspects of plasma behavior, and gives rise to an energy flow which is known as Landou damping.

Now we have been studying in various kinds of field, for example studies of space plasmas using observation data, plasma etching applied to devices, laser plasma interactions, etc. And as to space plasmas, they have made more clearly by development of scientific satellites and the progress of observational technology what plasmas in universe behave in far away. The understanding of characteristics of plasma can be contributed to our future in many aspects such as discovery of new physics and application of plasma techniques.

1.2 Characteristics of Electron-Positron Plasma and Electron-Ion Plasma

In previous section, we explained that plasma included negative and positive charged particles. Concerning with classification of plasma, we can classify into electron-positron plasma and electron-ion plasma. Electron-positron plasmas are produced from high energy photon. This process is called pair production ($\gamma + \gamma \rightarrow e^+ + e^-$).

It seldom happens in standard plasmas. It is well known that electron-positron plasmas may exist in pulsar magnetospheres and in active galactic nuclei(AGN) and early universe(the big bang) from 10^{-2} to 1 second. Pulsar is a neutron star rotating very high speed. And in neutron star, it is thought to be occurring particle production and annihilation such as electron-positron pair creations. And it is thought to happen the collision between these electron-positron plasma clouds radiating from binary pulsar. And high energy particles can be observed from collision regions and also observed excitation of electromagnetic waves. Accelerated electrons and positrons are found in a high energy plasma clouds near pulsar and these high energy particles may be associated with a variety of astrophysical source of synchrotron radiation. It is important to investigate the mechanism of these excitations and particle accelerations.

Since time and spatial scales associated with electron and positron are identical due to the same charge and mass ratio, electron-positron plasma may offer plasma physical properties quite different from electron-ion plasmas. So, in the study of electron-positron plasma special attention should be paid in following aspects. (1) Electron and positron have same dynamical properties since they have same mass and charge. In the case of electron-ion plasma, because of mass difference, time scales are completely different. (2) Coupling to electromagnetic waves. (3) In the presence of a magnetic field, electron and positron perform a gyromotion at the same frequency in opposite directions.

In simulation on electron-ion plasma, we consider ions are assumed to be rest. Concerning with application for electron-ion plasmas, with the development of the technique of chirped pulse amplification, which has enabled lasers to produce multiterawatt and petawatt femtosecond laser pulses,[30] many interesting new physical phenomena came within our grasps. For example, exceedingly large magnetic fields are generated in laser plasmas. They modify the interaction of ultraintense laser pulses with both overdense and underdense plasmas.[31] The self-generated magnetic fields affect the energy transport, and the overall plasma expansion[32] and leads to the bending and merging of the laser beams.[13]

Recently the experimental results on the dynamics of the plasma channel produced by a high intensity short laser pulse propagating in a plasma were reported in Ref. [33], where the self-focusing and channeling of the laser pulse, plasma channel formation, and the dynamics of ambient gas excitation and ionization were observed. Rapid surrounding gas ionization has been observed after the channel formation and it was attributed to the fast ions expelled from the laser channel and propagating radially outwards. As it has been noticed in Ref. [11] the fast ions cannot propagate alone, they carry an appropriate number of free electrons with them in order to compensate a space charge and therefore form the colliding plasmas with counterstreaming electrons and zero net electric current. The kinetic energy of the electron beams can be partly converted into magnetic field energy in the course of the beam-plasma instabilities

1.3 Particle Simulation of Colliding Plasma

1.3.1 Where can we see the Colliding Plasma?

In this thesis, I addressed the colliding plasmas in space and laser plasmas. (see Fig.1-1) I researched by using computer simulation the region where two or more plasmas clouds collide each other and what happens in these regions. We can see the colliding plasmas in space plasmas, for example near the pulsar or Sun. And in experimental plasma, for example, the interaction between plasmas accelerated by laser pulse. Concerning kinds of colliding plasmas, electron-positron plasma may exist in the region of the first stage of the universe, pulsar magnetosphere, AGN(active galactic nucleus) and so on. Electron-ion plasmas are thought to exist in the surface of solar atmosphere and the region of prominence formation and corona. And laser plasma is also electron-ion plasma. In the colliding plasmas, the intense of generated self-electric field and self-magnetic field are observed. Even if initially there is a charge quasineutrality and a compensation of the electric currents the intense electric and magnetic fields appear as a result of the electromagnetic instability development. It is important and interesting to find new physics and to understand mechanism of these phenomena which caused by plasma clouds collision. Then these results will be able to apply to developments of plasma in many aspects.

1.3.2 Why do we use the Computer Simulation?

Computer simulation, it is one of the great method of investigation to understand both linear and non-linear plasma problems. Solving the theoretical equation without contradiction, we can investigate and understand the unknown physics and interesting phenomena easily, speedily and accurately even if problems is not so easy to realize by experimental method. The development of computer simulation depends upon the progress of hardware and software of computer. Because we can do the simulations larger and larger scale going with development of machine spec. Its development is still increasing day by day.

Computer simulation of plasma physics basically comprises two general areas based on kinetic and fluid descriptions. In fluid models, plasma behaviors are described by a set of fluid equations. (MHD:magnetohydrodynamics equations) For studying the individual nature of a particle, on the other hand, particle simulation is necessary to describing the behavior by following the motion of a large number of charged particles in their self-consistent electric and magnetic fields. But comparing with fluid model, particle model is limited to looking at the phenomena in a relatively small scale and short period of time. To solve the set of equations accurately, it is required high efficient numerical techniques. Numerical schemes for particle simulations have been developed quickly. Field mover is to update electric and magnetic fields self-consistently in space and time based on Maxwell equations. Particle mover is to advance particles under the guidance of electric field and magnetic fields through solving the motion equation of particles. The leap-flog method using these simulation is common in use for simplicity of implementation and relative accuracy. At to the boundary condition of simulation code, we used periodic

boundary condition. But in simulation, proper boundary conditions for field and particles should be chosen depending upon what simulations are to aim. Periodic boundary conditions are thought of being suitable for a finite system domain from the other side of boundaries when they encounter a boundary. In space application the most relevant boundary condition for fields is that they should be able to radiate away into space and should not be reflected at the boundaries.

And now, we use computer simulations to study the physical processes in the region where plasma clouds collide. We investigate by using two-dimensional fully relativistic particle code simulation. The code used in the simulation is a successor to the TRISTAN code originally for the Cray-T and Cray X/MP developed by professor Oscar Buneman. These include:Poisson's equation and Fourier transforms have been eliminated by updating the field locally from the curl equations and depositing the particles currents according to charge conserving formulas. Filtering is done locally, that makes the code ideally suited to modern parallel mechanisms, then the code is in Fortran and fully transportable. We compared the results of simulation and the theories and the observation data of real universe plasmas. And we expect to do a new discovery and to make clear the plasma physics.

1.4 Several Instabilities Growing From Collision of Plasmas

The plasma exists the most stable in the case of conditions such as density and temperature are uniform spatially. And plasma is also stable when the velocity distribution is following to the maxwell distribution. On the other hand, if the plasma becomes unstable, it automatically occurs some kinds of instabilities in order to try to go back stable conditions. As to theoretical treatment of plasma instabilities, we often have been using the methods treating as linear problem under the assumption which perturbation occurring by unstable is small. By this method, we can find the growth rate under the condition which the perturbation is relatively small, and find the parameter condition generated some instabilities. Instabilities of plasma are generally dealt with using energy theory. But it is difficult to classify some groups simply because their phenomena and properties are quite complicated. Generally speaking, plasma instabilities are classified to macro instability(ex. MHD instability) and micro instability (kink instability). Several instabilities can be seen in colliding plasma. The characteristics of their instabilities are shown as follow:

1.4.1 Weibel Instability

The Weibel instability is expected to be one of the mechanisms at play in the generation of quasi-static magnetic fields by high intensity laser pulses propagating with relativistic amplitudes in underdense plasmas. The instability can be excited in a plasma with two electron populations: the background cold electrons and the high energy electrons accelerated by the laser radiation. The mechanism associated with the growth of the Weibel instability is near the rear part of the laser pulse and behind it fast electron beams are present,caused by breaking of the Langmuir waves

produced by the laser pulse. Due to the plasma quasi-neutrality, the average current of these electrons must be canceled by an opposite current carried by electrons of the cold plasma component. These oppositely directed currents repel each other, making the distribution of the current density in the plasma inhomogeneous in the transverse direction and producing a quasi-stationary magnetic field.

1.4.2 Diocotron Instability

The diocotron instability in a one dimensional n = n(r) nonneutral single species plasma, for example in a Penning-Malmberg trap, is an instability driven by the presence of a hollow density profile. It is well known that the l=1, k=0 mode is exponentially stable (i.e. does not have an exponentially growingmode) regardless of the hollowness of the profile, although there can be weak power law growth associated with phase mixing of modes at an endpoint of the continuum [Smith and Rosenbluth, 1990.]

This instability has nothing to do with the magnetron or diocotron fluid instability(O. Buneman, et. al. J of Applied Physics), 37(8):3203-22, July 1966. The growth of the mode produced from the collapse of cycloidal flow is faster than those of the above mentioned fluid instabilities. After the perturbation from the collapse of the cycloidal flow saturates, eventually the fastest growing fluid instability will dominate the system.

1.4.3 Counter-Streaming Instability

It is known that counter-streaming plasmas are subject to a host of instabilities. In the case of relativistic plasmas, excitation of electromagnetic modes is as important as that of electrostatic modes because the factor v/c is of the order of one. Moreover, in the case of colliding relativistic electron-positron streams in which the net electric charge and current vanish, we expect to see electromagnetic mode excitation that is similar to the Weibel instability in a plasma with anisotropic temperature (Weibel[3], 1959). Recently, counter-streaming electromagnetic instability has been the subject of a detailed investigation in the study of the generation of quasi-static magnetic fields in laser plasmas.[6] Kazimura et al.[23,24] investigated the dynamics of collisions of clouds of both electron-ion and pair plasmas. They revealed that magnetic fields are generated and high-energy particles are produced.

1.4.4 Following Instability and Current Filamentation Instability

Recently the experimental results on the dynamics of the plasma channel produced by a high intensity short laser pulse propagating in a plasma were reported in Ref. [33], where the self-focusing and channeling of the laser pulse, plasma channel formation, and the dynamics of ambient gas excitation and ionization were observed. Rapid surrounding gas ionization has been observed after the channel formation and it was attributed to the fast ions expelled from the laser channel and propagating radially outwards. As it has been noticed in Ref. [11] the fast ions cannot propagate alone, they carry an appropriate number of free electrons with them in order to

compensate a space charge and therefore form the colliding plasmas with counter-streaming electrons and zero net electric current. The kinetic energy of the electron beams can be partly converted into magnetic field energy in the course of the beam-plasma instabilities. The current is unstable for transverse perturbations, and it is called as the current filamentation instability.[34] This instability is similar to the Weibel instability[3] which occurs in a collisionless plasma with an anisotropic temperature. The linear and nonlinear aspects of the filamentation instability have been studied in [34]. Electromagnetic current filamentation-hollowing instability leads to formation of the electric current filaments with the transversal size of the order of the collisionless skin depth. The merging of current filaments correspond to the magnetic islands coalescence. Eventually this process leads to the formation of the quasi-equilibrium, stable configuration. This configuration has a form of separated electric current filaments and it is associated with the magnetic islands and vortices. The self-generated magnetic field is directed both perpendicularly and parallel to the direction to the initial plasma velocity. The distribution of the electric current has a form of cylindrical, well separated layers. The conversion rate of the electron kinetic energy into the energy of self generated magnetic field is about $10 - 20\%$.

1.5 Outline of this thesis

In this thesis, I investigate the dynamics of colliding plasma both electron-positron and electron-ion. We consider ions are assumed to be rest. I want to emphasize that several simulation results provided good agreement with electron-positron linear theory which derived by myself from extension of only electron linear theory (Califano et al[6] 1997). The theoretical growth rate of electron-positron two counter-streaming plasmas which derived from a set of linear equations using fluid approximation have not been solved yet, but in this thesis, I have succeeded to solve theoretical linear dispersion relation of 4-fluid model electron-position plasmas. [See Appendix 1]

In Chapter 1, we described the general introduction about colliding plasmas and motivations. In Chapter 2, we presented results of analytical studies and 2D3V PIC simulations of electron-positron and electron-ion plasma clouds collision. In Chapter 3, we presented the results which may be applicable to the laser-plasma interaction. And in Chapter 4, we described theoretical and simulation research into the properties of electron/electron instabilities under parameters appropriate for the polar and auroral magnetosphere and to demonstrate some observed properties. The most important result as to the plasma collision in space plasma, is the generation of the magnetic field in the direction perpendicular to the counter-stream direction from the initial state with no-magnetic field. And it provides good agreement with the linear theory. It is a new linear theory which I derived from the relativistic two-fluid model of counter-streaming electron-positron plasma. And it is also important result about interaction of laser-plasma that we investigated nonlinear development of the electromagnetic current filamentation-hollowing instability.

Chapter 2

Simulation of Colliding Plasma in Space

Introduction

There are a few kinds of plasmas in the universe, for example,electron-positron plasma and electron-ion plasma. It is known that relativistic electron-positron plasma may exist in the region of the first stage of the universe, pulsar magnetosphere,AGN(active galactic nucleus) and so on. Electron-ion plasmas are thought to exist in the surface of solar atmosphere and the region of prominence formation and corona.

Especially we concentrate on the electron-positron plasma in first section. Why electron-positron plasmas are important and interesting? One of the reason is that it is a new research field, and recently electron-positron plasmas have been realized in laboratory plasma experiments. As we said above, electron-positron plasmas exist in pulsar wind. Pulsars or more precisely radio pulsars were discovered in 1967 and almost immediately identified as rotating neutron stars.(Figure 1-2) Their mass is of order of the solar mass, and their radius is only about 10km. The fact that pulsars are recognized as the neutron stars predicted by Baade and Zwicky as far back as 1934, is rightly regarded as one of the greatest discoveries in astrophysics. Pulsars are now under study in practically all of the biggest observatories of the world.

The discovery of binary pulsar has raised an interesting question of what happens in the interaction region where two pulsar winds collide. And electron-ion plasma is observed in the region where two stellar winds (Binary star) collide . Recent observations imply that collision of electron-positron and electron-ion counter-streaming may cause high energy particles acceleration, emission of electromagnetic waves and so on.

But physical processes in this region are not well understood. Still more it is very difficult to make such a plasma state on earth with the latest technology. And now, we use computer simulations to study the physical processes in the region where two streaming clouds collide. We made a comparison among the results of simulation and the theory and the observation data of real universe plasma. And we expect to do a new discovery and to make clear the plasma physics.

Figure captions

Figure 1-1. The brief resume in this thesis.

Figure 1-2. A model of a radio pulsar as a rotating strong magnetized neutron star, showing regions of radio emission generation.

Colliding plasmas			
Space Plasma	章	実験室プラズマ	章
electron-positron plasma	2	Laser Plasma interaction	6,7
electron-ion plasma	3	(electron-ion plasma)	
collision in narrow region	4		
After plasmas collided	5		
Beam instability	8		

Figure 1-1

Parameters of real neutron stars

Mass, M	$1.2-1.6M_{\odot}$
Radius, R	8–15 km
Moment of inertia, A,	$\sim 10^{45}$ g cm^2
Magnetic field on the surface, B_0	$\sim 10^{12}$ G
Surface temperature, T	$\lesssim 10^6$ K

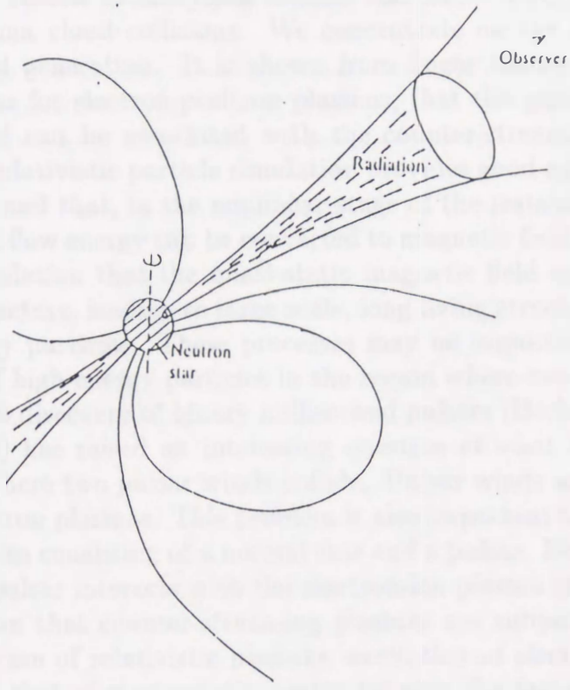

Figure 1-2

2 GENERATION OF MAGNETIC FIELD AND PARTICLE ACCELERATION DURING COLLISION OF ELECTRON POSITRON PLASMA CLOUDS

2.1 Introduction

We present results of analytical studies and 2D3V PIC simulations of electron-positron plasma cloud collisions. We concentrate on the problem of quasi-static magnetic field generation. It is shown from linear theory, using relativistic two-fluid equations for electron-positron plasmas, that the generation of a quasi-static magnetic field can be associated with the counter-streaming instability. A two-dimensional relativistic particle simulation provides good agreement with the above linear theory and that, in the nonlinear stage of the instability, about 5.3 % of the initial plasma flow energy can be converted to magnetic field energy. It is also shown from the simulation that the quasi-static magnetic field undergoes a collision-less change of structure, leading to large scale, long living structures and the production of high-energy particles. These processes may be important for understanding of production of high-energy particles in the region where two pulsar winds collide.

The recent discovery of binary millisecond pulsars (Becker et al.[1] 1996, Lorimer et al[2]. 1996) has raised an interesting question of what happens in the interaction region where two pulsar winds collide. Pulsar winds are believed to consist of electron-positron plasmas. This problem is also important to consider in the case of a binary system consisting of a normal star and a pulsar. Here the electron-positron plasma of a pulsar interacts with the electron-ion plasma of a star.

It is known that counter-streaming plasmas are subject to a host of instabilities. In the case of relativistic plasmas, excitation of electromagnetic modes is as important as that of electrostatic modes because the factor v/c is of the order of one. Moreover, in the case of colliding relativistic electron-positron streams in which the net electric charge and current vanish, we expect to see electromagnetic mode excitation that is similar to the Weibel instability in a plasma with anisotropic temperature (Weibel[3], 1959). Recently the Weibel instability has been the subject of detailed investigations in the study of quasi-static magnetic field generation in laser plasmas (see Askar'yan et al[4]. 1994, Bulanov et al[5]. 1996, Califano et al[6]. 1997). It has been shown that in electron-ion plasmas, the Weibel instability in the nonlinear stage leads to formation of large scale, long-living electron vortices associated with the magnetic fields. This provides the generic mechanism of generation of quasi-static magnetic fields in plasmas, which may be also important in the origin of cosmical magnetic field (Kronberg[7], 1993, Kulsrud et al[8]. 1997).

We investigate physical processes during the collision of counter-streaming electron-positron plasmas using a relativistic two-fluid model and a relativistic particle simulation.(Figure 2-2)

In Section 2.2 we present a linear theory derived from the relativistic two-fluid model, and show the excitation of strong electromagnetic perturbations associated

with quasi-static magnetic fields. In Section 2.3 we show results from a two-dimensional relativistic particle simulation. In the linear regime there is a good agreement between linear theory and simulations. In the nonlinear stage, the magnetic field can undergo collision-less change of structure, and a large scale structure of the magnetic field is produced. During this restructuring, simulations show that high-energy particles are created. In Section 2.4 ~2.5 we summarize our results and briefly discuss some implications of the present process.

2.2 Linear Theory of Electromagnetic Instability

The dynamics of counter-streaming electron-positron plasmas with velocities $\mathbf{v}_{ia}$, where $i = p(positron)$ and $i = e(electron)$ and $a = 1, 2$ are the two counter-streaming components of particles, is described by the equations:

$$\frac{\partial \mathrm{P}_{ea}}{\partial t} = -\mathbf{v}_{ea} \cdot \nabla \mathrm{P}_{ea} - (\mathrm{E} + \mathbf{v}_{ea} \times \mathrm{B}), \tag{1}$$

$$\frac{\partial \mathrm{P}_{pa}}{\partial t} = -\mathbf{v}_{pa} \cdot \nabla \mathrm{P}_{pa} + (\mathrm{E} + \mathbf{v}_{pa} \times \mathrm{B}), \tag{2}$$

$$\frac{\partial (n_{pa} - n_{ea})}{\partial t} + \nabla \cdot (n_{pa}\mathbf{v}_{pa} - n_{ea}\mathbf{v}_{ea}) = 0, \tag{3}$$

$$\frac{\partial \mathrm{B}}{\partial t} = -\nabla \times \mathrm{E}, \tag{4}$$

$$\frac{\partial \mathrm{E}}{\partial t} = \nabla \times \mathrm{B} - \sum_a (\mathrm{J}_{pa} + \mathrm{J}_{ea}), \tag{5}$$

$$\nabla \cdot \mathrm{E} = \sum_a (n_{pa} - n_{ea}), \tag{6}$$

$$\mathbf{v}_{ea} = \frac{\mathrm{P}_{ea}}{(1 + \mathrm{P}_{ea}{}^2)^{\frac{1}{2}}}, \tag{7}$$

$$\mathbf{v}_{pa} = \frac{\mathrm{P}_{pa}}{(1 + \mathrm{P}_{pa}{}^2)^{\frac{1}{2}}}, \tag{8}$$

$$\mathrm{J}_{ea} = -n_{ea}\mathbf{v}_{ea}, \tag{9}$$

$$\mathrm{J}_{pa} = n_{pa}\mathbf{v}_{pa}, \tag{10}$$

where the densities and the velocities are normalized by a characteristic density n, the speed of light c and the time is normalized by the plasma frequency $\omega_{pe} = (4\pi n e^2/m)^{\frac{1}{2}}$.

We consider a case in which the counter-streaming plasmas have equal velocity in the y-direction and density such as $v_{0,e1} = v_{0,p1}$, $n_{0,e1} = n_{0,p1}$, $v_{0,e2} = v_{0,p2}$, $n_{0,e2} = n_{0,p2}$.

Linearizing the above set of equations and assuming a dependence of the form

$$F(x,y,t) = f\exp(i(k_x x + k_y y - \omega t)),$$

then the time and spatial derivations can be represented by

$$\frac{\partial}{\partial t} - - - - - > -iw$$

$$\nabla - - - - - > iK$$

$$\nabla \cdot - - - -- > iK\cdot$$

$$\nabla \times - - - - > iK\times$$

When only small-amplitude perturbations are considered, the dynamic variables can be expressed in terms of their equilibrium and perturbed parts.

$$P_a = P_0 + P_1$$

$$v_a = v_0 + v_1$$

$$n_a = n_0 + n_1$$

$$E = E_1$$

$$B = B_1$$

where the subscripts 0 and 1 refer to the equilibrium and perturbed quantities.In equilibrium, $v_0 = E_0 = 0$. v and E arise from perturbing an equilibrium fluid and hence they are first-order quantities.Our interest is to retain quantities only to first-order, ignoring higher order terms. Substitute these perturbations to (1) $\sim$ (10)equation, and linearized.

[See Appendix 1]

$$\epsilon(\omega,k)\cdot E = 0 \tag{11}$$

where,$E \neq 0$ so,

$$\epsilon(\omega,k) = 0 \tag{12}$$

Then we obtain the following dispersion equation:

$$(1-\Omega_{2p}^{-2}-\Omega_{2e}^{-2})\{(1+\Omega_{4p}^{-2}+\Omega_{4e}^{-2})k_y^2 - \omega^2(1-\Omega_{1p}^{-2}-\Omega_{1e}^{-2}) - 2\omega k_y(\Omega_{3p}^{-2}+\Omega_{3e}^{-2})\}$$

$$+k_x^2\{(1+\Omega_{4p}^{-2}+\Omega_{4e}^{-2})(1-\Omega_{1p}^{-2}-\Omega_{1e}^{-2}) + (\Omega_{3p}^{-2}+\Omega_{3e}^{-2})^2\} = 0, \tag{13}$$

where

$$\Omega_{1e}^{-2} = \sum_a \frac{n_{0,ea}}{\Gamma_{ea}\Omega_{ea}^2}, \quad \Omega_{2e}^{-2} = \sum_a \frac{n_{0,ea}}{\Gamma_{ea}^3\Omega_{ea}^2},$$

$$\Omega_{3e}^{-2} = \sum_a \frac{n_{0,ea}v_{0,ea}}{\Gamma_{ea}\Omega_{ea}^2}, \quad \Omega_{4e}^{-2} = \sum_a \frac{n_{0,ae}v_{0,ae}^2}{\Gamma_{ae}\Omega_{ae}^2},$$

$$\Omega_{1p}^{-2} = \sum_a \frac{n_{0,pa}}{\Gamma_{pa}\Omega_{pa}^2}, \quad \Omega_{2p}^{-2} = \sum_a \frac{n_{0,pa}}{\Gamma_{pa}^3\Omega_{pa}^2},$$

$$\Omega_{3p}^{-2} = \sum_a \frac{n_{0,pa}v_{0,pa}}{\Gamma_{pa}\Omega_{pa}^2}, \quad \Omega_{4p}^{-2} = \sum_a \frac{n_{0,pa}v_{0,pa}^2}{\Gamma_{pa}\Omega_{pa}^2},$$

$$a = 1, 2.$$

Here the following notations are used:

$$\Omega_{pa} = \omega - k_y v_{0,pa}, \qquad \Gamma_{pa} = (1 - v_{0,pa}^2)^{-1/2},$$

$$\Omega_{ea} = \omega - k_y v_{0,ea}, \qquad \Gamma_{ea} = (1 - v_{0,ea}^2)^{-1/2},$$

$$a = 1, 2.$$

We note here that the above dispersion relation is an extension of the case derived by Califano et al[6].(1997), who investigated the development of the Weibel instability and magnetic field generation by high-intensity laser pulses propagating with relativistic amplitude in underdense plasmas. In their problem, electrons are counter-streaming, while immobile ions form a charge-neutralizing background. In our cases, both electrons and positrons are counter-streaming.

We did a numerical calculation to obtain the growth rate of the electromagnetic instability. The parameters used here coincide with those used in the simulation in the next section. We consider collision of two symmetric plasma flows with velocities, $v_0 = 0.56c$ and $-0.56c$, and with equal density.

Figure 2-3 shows the growth rate normalized by ω_{pe} versus the wave-number k_x normalized by c/ω_{pe} for the propagation angle of 27.5 degree from the y-direction. As seen in this figure, there appear three different branches, (a), (b) and (c). The branch (a) can exist for one-component counter-streams (electrons or positrons), while the other branches (b) and (c) disappear for one-component streams. Branch (a) is similar to the Weibel instability in laser plasmas (Califano et al[6].1997). On the other hand, branches (b) and (c) are caused by the instability driven by the coupling of two component counter-streams, and these two branches merge into one mode when $k_x \gg k_y$.

When the propagation direction of the excited waves approaches the y-direction, the instability tends to have the characteristics of the pure electrostatic two-stream instability. When the propagation direction approaches the x-direction, then the instability associated with branches b and c becomes with more electromagnetic, with a high growth rate.

2.3 Simulation Model

The code used here is a $2D3V$, fully relativistic electromagnetic particle-in-cell code, modified from the $3D3V$ TRISTAN code[16] (Buneman,1993). The system size is $L_x = 65\Delta$ and $L_y = 1024\Delta$, where $\Delta(= 1)$ is the grid size. Periodic boundary conditions are imposed on particles and fields. There are 1,331,200 electron- positron pairs filling the entire domain uniformly and keeping the domain charge neutral. Hence the average particle number density is about 20 per cell. The initial state is such that in the region of $Y = (1 \sim 512)\Delta$, the plasma drift velocity is $v_d = 0.56c$ (c is the light speed), with shifted Maxwellian distribution with the thermal velocity $v_{th} = 0.09366c$, and in the region, $Y = (512 \sim 1024)\Delta$, $v_d = -0.56c$. This corresponds to a Lorentz factor $\gamma = (1 - (v_d/c)^2)^{-1/2} = 1.2$. Other parameters are

as follows; the mass ratio $m_p/m_e = 1$(p:positron,e:electron), $\omega_{pe}\Delta t = 0.052$, the electron collisionless skin depth $d_e = c/\omega_{pe} = 9.6\Delta$. Thus the computation box has a size equal $\approx 6.6d_e$ in the $x-$direction and $\approx 106.6d_e$ in the $y-$direction. The initial electric and magnetic field is zero.

2.4 Simulation Results

We investigated several cases of electron-positron plasma cloud collisions, and here we show only one case of them. The most important result is the generation of the magnetic field in the direction perpendicular to the counter-stream direction from the initial state with no-magnetic field.

Figure 2-4 shows the time development of the magnetic field (B_z) structures in the x-y plane. As seen in Fig.2-4(a), initially (for $\omega_{pe}t = 10$) there appears very coherent structures with positive and negative magnetic polarities. This corresponds to the filamentation of the plasma with creation of the current sheet system with the current sheets situated where the magnetic field changes sign. The characteristic scale of the current sheet is about $0.6d_e$ in the transverse direction along the $x-$axis and about $2\pi d_e$ in the longitudinal direction along the $y-$axis, which is also consistent with the branch (c) of the linear theory shown in Fig.2-3.

As time goes on, the front of both streams propagates further and behind the front the bending and coalescence of the filaments occur as it is seen in Fig.2-4(b) where the magnetic field pattern is shown for $\omega_{pe}t = 31$. This process makes the characteristic scale length of the magnetic field larger. The coalescence process of filaments first becomes apparent after about $\omega_{pe}t = 31$. Asymptotically, at $\omega_{pe}t = 52.7$, in Fig.2-4(c), we see formation of large scale, long lived magnetic structures with the size of the order of $2\pi c/\omega_{pe}$. The alternating polarity corresponds to electric current distributions in the x, y-plane of the form of antisymmetric vortex flow.

Figure 2-5 shows the time history of electric (${E_x}^2$, ${E_y}^2$) and magnetic (${B_z}^2$) field energy. By using the final value of the magnetic energy , we can estimate the energy conversion rate from the initial kinetic flow energy. We find that the energy conversion rate is about 5.3%. Figure 2-6 shows the time history of electric (${E_x}^2$, ${E_y}^2$) and magnetic (${B_z}^2$) field energy normalized by $2VtL_x/L_xL_y$,where V is the plasma front velocity of the streams, assumed to be constant. Thus they give the dependencies of the average values of the fields v.s. time. The difference between Figs. 2-5 and Figs.2-6 is normalization of field energy. Figs. 2-5 show the total field energy of each component in system box. On the other hands Figs. 2-6 show the energy of region where two counter-streaming collide each other.

As seen in Figs. 2-6(a) and 2-6(b), almost the same amount of electrostatic wave energy is excited in the x- and y-directions. From a Fourier analysis of the wave patterns in E_x and E_y, we find that the electrostatic energy is associated with the Langmuir waves. The propagation direction in which the waves are excited is oblique and at an angle of about 45 degree from the x-direction.

As seen in Fig.2-6(c), a strong magnetic B_z component can be excited with almost the same growth rate as the Langmuir waves. The maximum magnetic energy is about twice the electric field energy. This is consistent with the Weibel

mode development. The electric field amplitude can be estimated from equation (4) as $E \approx (\omega/kc)B$. If we take ω to be of the order $\omega \approx \gamma \approx (v_0/c)\omega_{pe}$, we obtain for $v_0/c \approx 0.5$ a magnetic energy which is about twice the electric field energy.

The growth rate observed from Fig.2-6(c) agrees with the branch (c) obtained from the linear theory given in the previous section, and is about $\gamma = (v_0/c)\omega_{pe}$. The magnitude of the growth rate calculated from the dispersion relation is about 0.69 with $k_x = 1.68$ and $k_y = 3.82$ while the value of growth rate calculated from the time history of magnetic field energy is about 0.67.[See Appendix 2].

We note here that the above the value of $k_x = 1.68$ is read from the figure 2-7 and figure 2-8. At first figure 2-7 show the wave intensity of B_z as a function of ω and k_x. In that figure the value of the large intense is about $k_x = 1.6$. And figure 2-8 show the time evolution of B_z along the x direction in the center of x-y plane.

The wave number(k_x) of standing wave in fig 2-8 is about $k_x = 1.68$. Because at early time step, the wave length of standing wave is about $\lambda = 16$, and the electron collisionless skin depth is 9.6 (see section 2.3). Hence the wave number k_x is about $\lambda = 16/d_e = 16/9.6 = 1.68$. When we calculated the growth rate from linear theory, we used this k_x. The value of k_y used the same calculation method. If we study the time evolution of high-energy particle distribution, then it appears particles with significant energy after $30\omega_{pe}t$. Therefore we may conclude that the particles can be accelerated due to collision-less change of the structure of the magnetic fields associated with the induction electric field. The collision-less change of the structure of the magnetic fields occurs via annihilation of magnetic fields with opposite polarity. This induces the electric field in the x, y-plane, which in turn accelerates charged particles. In Fig.2-9, we have seen no acceleration of the electrons and positrons along the z-direction in accordance with this process.

In Fig. 2-10 we show the electron (a) and positron (b) energy spectrum in the final stage; (c) is the initial energy distribution of both particles.

We did several other cases with different counter-streaming flow velocities, and also where one cloud is at rest. From these results we found that the important parameter for magnetic field generation is the relative velocity of clouds. The next we did the case of electron-ion counter-streams, in which the ion dynamics does not affect the generation of the magnetic field. Only counter-streaming electrons contribute to the generation of the magnetic field, which is quite similar to the case discussed by Califano et al[6]. (1997).

2.5 Discussion

It is shown from linear theory using relativistic two-fluid equations for electron-positron plasmas, that the generation of a quasi-static magnetic field is associated with the counter-streaming instability of electron-positron plasmas. A two-dimensional relativistic particle simulation is in good agreement with the above linear theory and furthermore, in the nonlinear stage of the instability, shows that about 5.3 % of the initial plasma flow energy can be converted to magnetic field energy. It is also shown from the simulation that the generated quasi-magnetic field undergoes a change in structure through coalescence of magnetic filaments, leading

to large scale structures and the production of high-energy particles. These processes may be important for understanding of the production of high-energy particles in the region of two colliding pulsar winds.

2.6 Summary

We investigated electron-positron plasma cloud collisions. The most important result is the generation of the magnetic field in the direction perpendicular to the counter-stream direction from the initial state with no-magnetic field. And as time goes on,we see formation of large scale, long lived magnetic structures. The alternating polarity corresponds to electric current distributions in the x, y-plane of the form of antisymmetric vortex flow. A two-dimensional relativistic particle simulation provides good agreement with the above linear theory and that, in the nonlinear stage of the instability, about 5.3 % of the initial plasma flow energy can be converted to magnetic field energy. And we have seen acceleration of the electrons and positrons.

Figure captions

Figure 2-2. The image of counter-stream from binary pulsar and system domain.$v_1 = 0.56c$, $v_2 = -0.56c$ (c is light velocity).

Figure 2-3. Linear growth rate normalized by c/ω_{pe} vs. the wave-number $\mathbf{k_x}$ normalized by ω_{pe} for the propagation angle of 27.5 degree, with respect to the y-direction. The parameter used is $V_d = 0.56c$. Branch (a) is similar to the Weibel instability, while branches (b) and (c) are caused by the instability driven by the coupling of two component counter-streams.

Figure 2-4. Time development of the magnetic field (B_z) structures in the x-y plane. (a) $\omega_{pe}t = 10$, (b) $\omega_{pe}t = 31$, (c) $\omega_{pe}t = 52.7$.

Figure 2-5. Time history of electric field energy; (a) ${E_x}^2$, (b) ${E_y}^2$ and magnetic field energy; (c) ${B_z}^2$.

Figure 2-6. Time history of electric field energy; (a) ${E_x}^2$, (b) ${E_y}^2$ and magnetic field energy; (c) ${B_z}^2$, normalized by $2VtL_x/L_xL_y$, where V is the plasma front velocity of the streams, assumed constant.

Figure 2-7. Wave intensity of B_z as a function of ω and $\mathbf{k_x}$ are normalized to ω_{pe} and c/ω_{pe} ,respectively.In that figure, the value of the large intense is about $\mathbf{k_x} = 1.6$.

Figure 2-8. The time evolution of B_z along the x-direction in the center of x-y plane. The wave number of standing wave in that figure is $\mathbf{k_x} = 1.68$.

Figure 2-9. The election velocity distributions of particles in each direction at $\omega_{pe} \cdot t = 0$ (dashed line), $\omega_{pe} \cdot t = 52.7$(full line).
V_{th} : electron thermal velocity

Figure 2-10. 4 The electron(a) and positron(b) energy spectrum in the final state of the simulation. E normalized by the thermal energy is total kinetic energy of particles. (c) shows the initial energy distribution of both particle species.

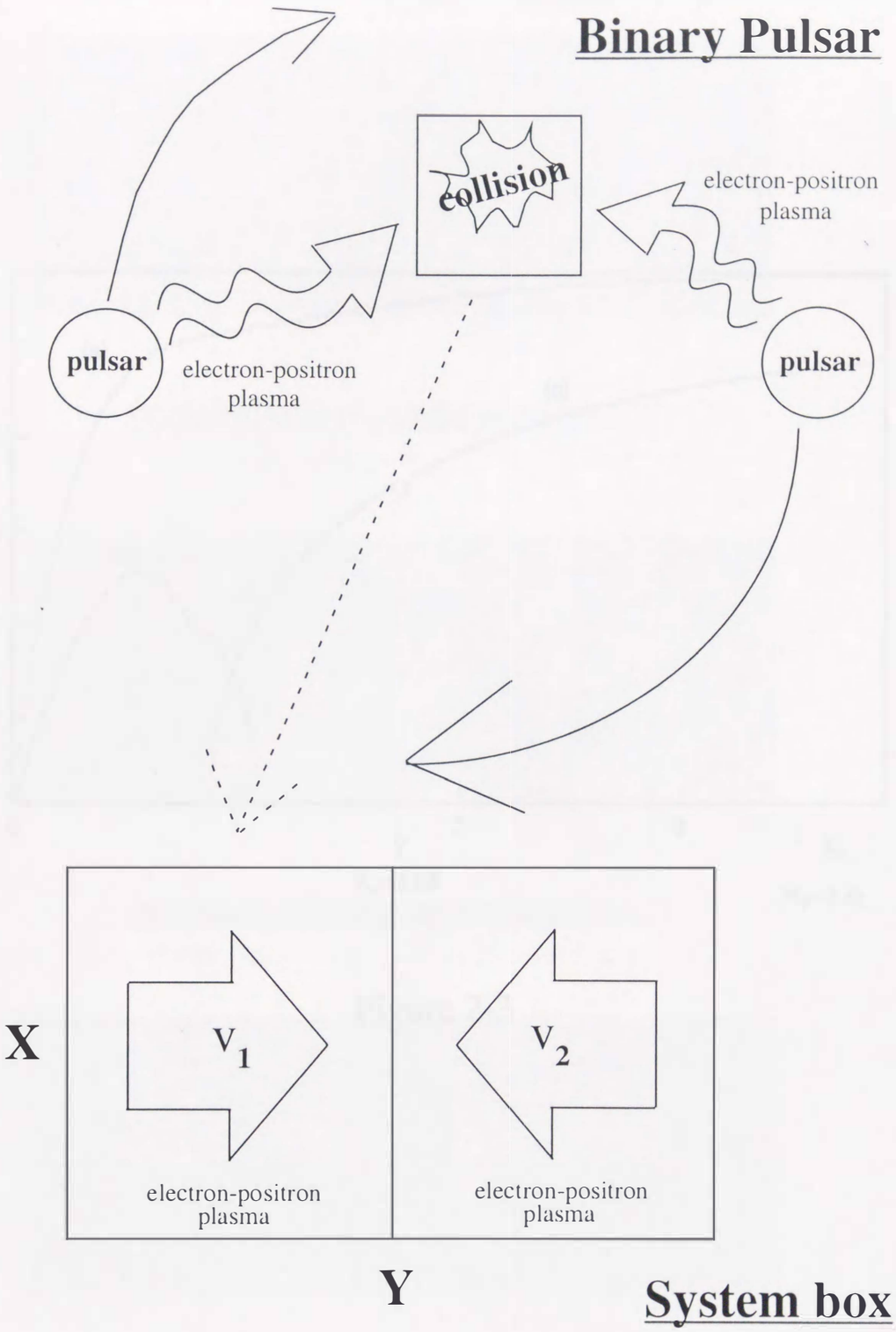
Binary Pulsar
collision
electron-positron plasma
pulsar
electron-positron plasma
pulsar
X
V_1
V_2
electron-positron plasma
electron-positron plasma
Y
System box

Figure 2-2

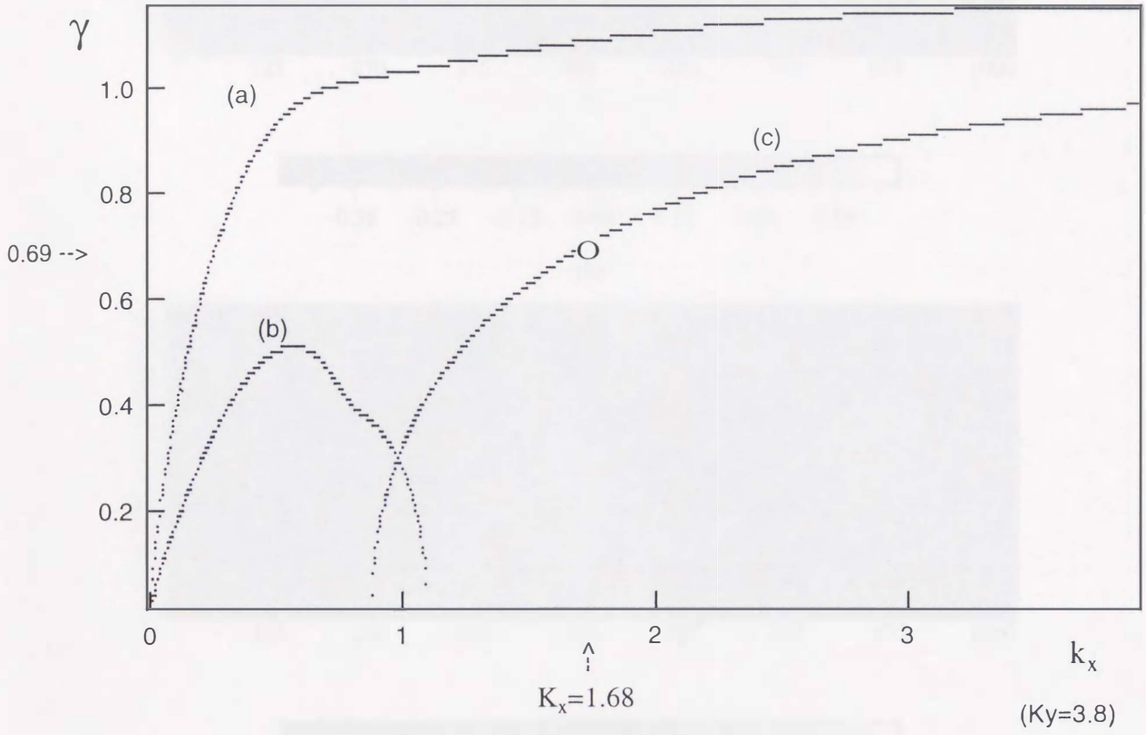

Figure 2-3

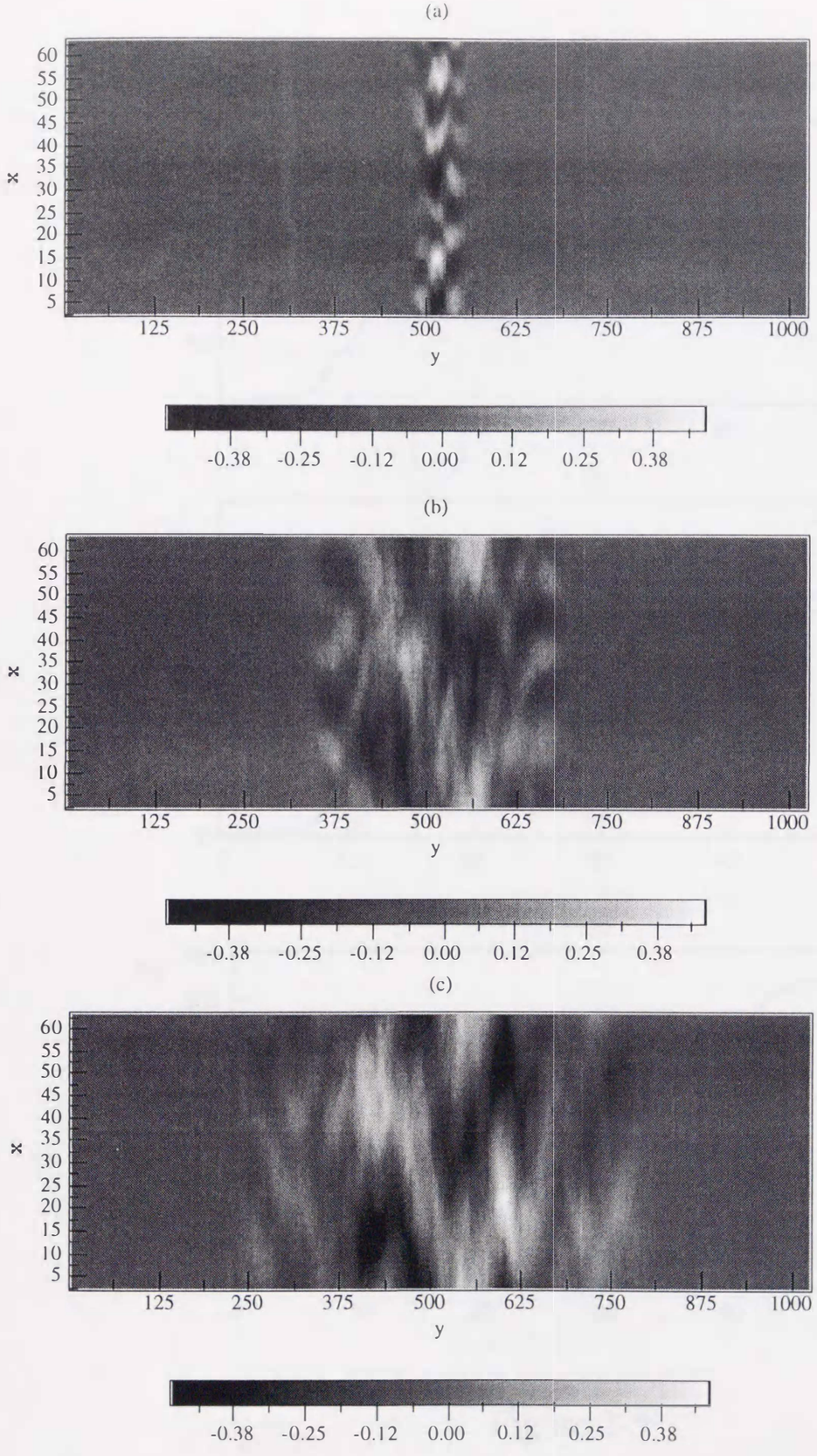
(a)
60
55
50
45
40
35
30
25
20
15
10
5
x
125
250
375
500
625
750
875
1000
y
-0.38
-0.25
-0.12
0.00
0.12
0.25
0.38
(b)
60
55
50
45
40
35
30
25
20
15
10
5
x
125
250
375
500
625
750
875
1000
y
-0.38
-0.25
-0.12
0.00
0.12
0.25
0.38
(c)
60
55
50
45
40
35
30
25
20
15
10
5
x
125
250
375
500
625
750
875
1000
y
-0.38
-0.25
-0.12
0.00
0.12
0.25
0.38

Figure 2-4

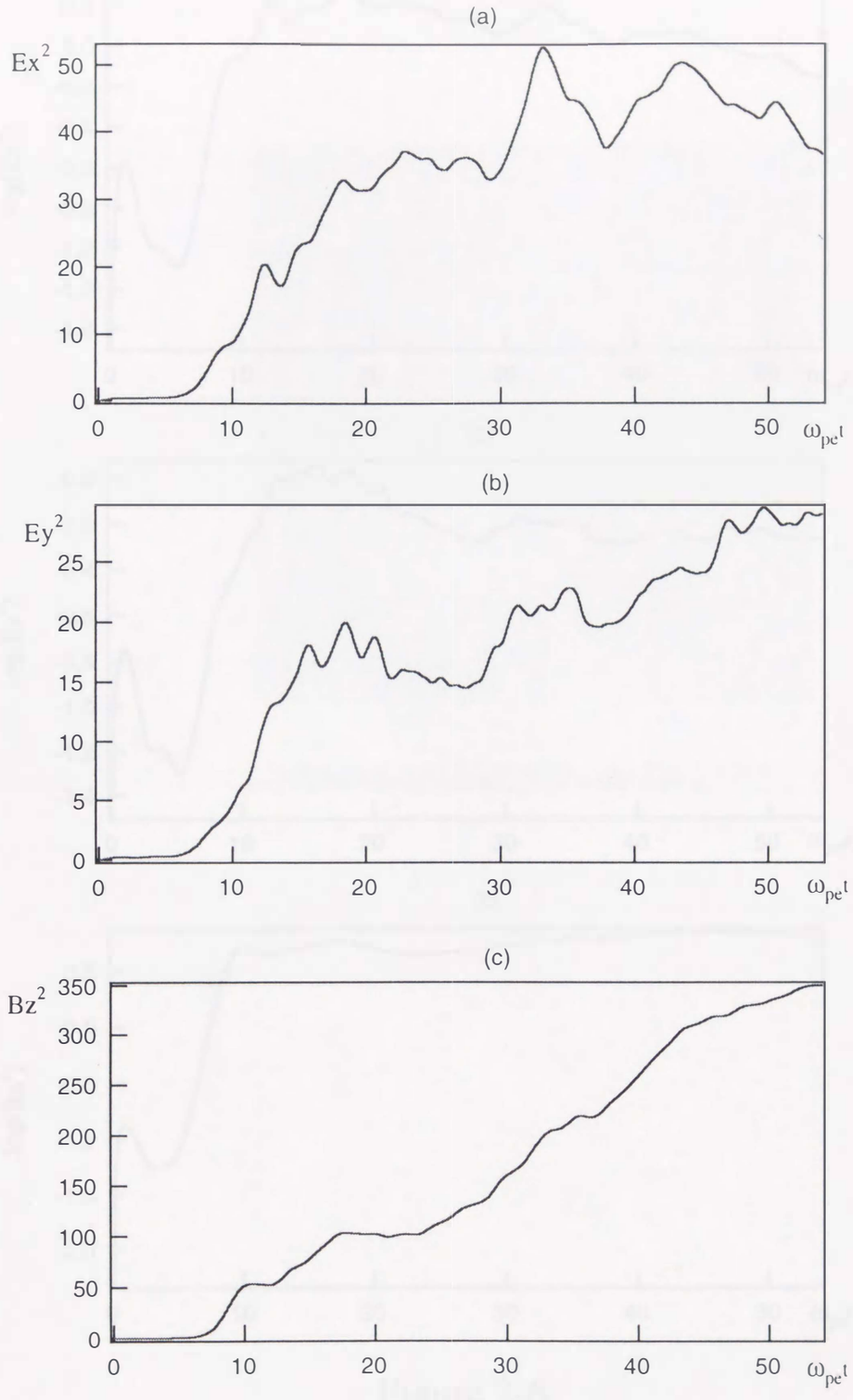
(a)
Ex^2
50
40
30
20
10
0
0
10
20
30
40
50
$\omega_{pe}t$
(b)
Ey^2
25
20
15
10
5
0
0
10
20
30
40
50
$\omega_{pe}t$
(c)
Bz^2
350
300
250
200
150
100
50
0
0
10
20
30
40
50
$\omega_{pe}t$

Figure 2-5

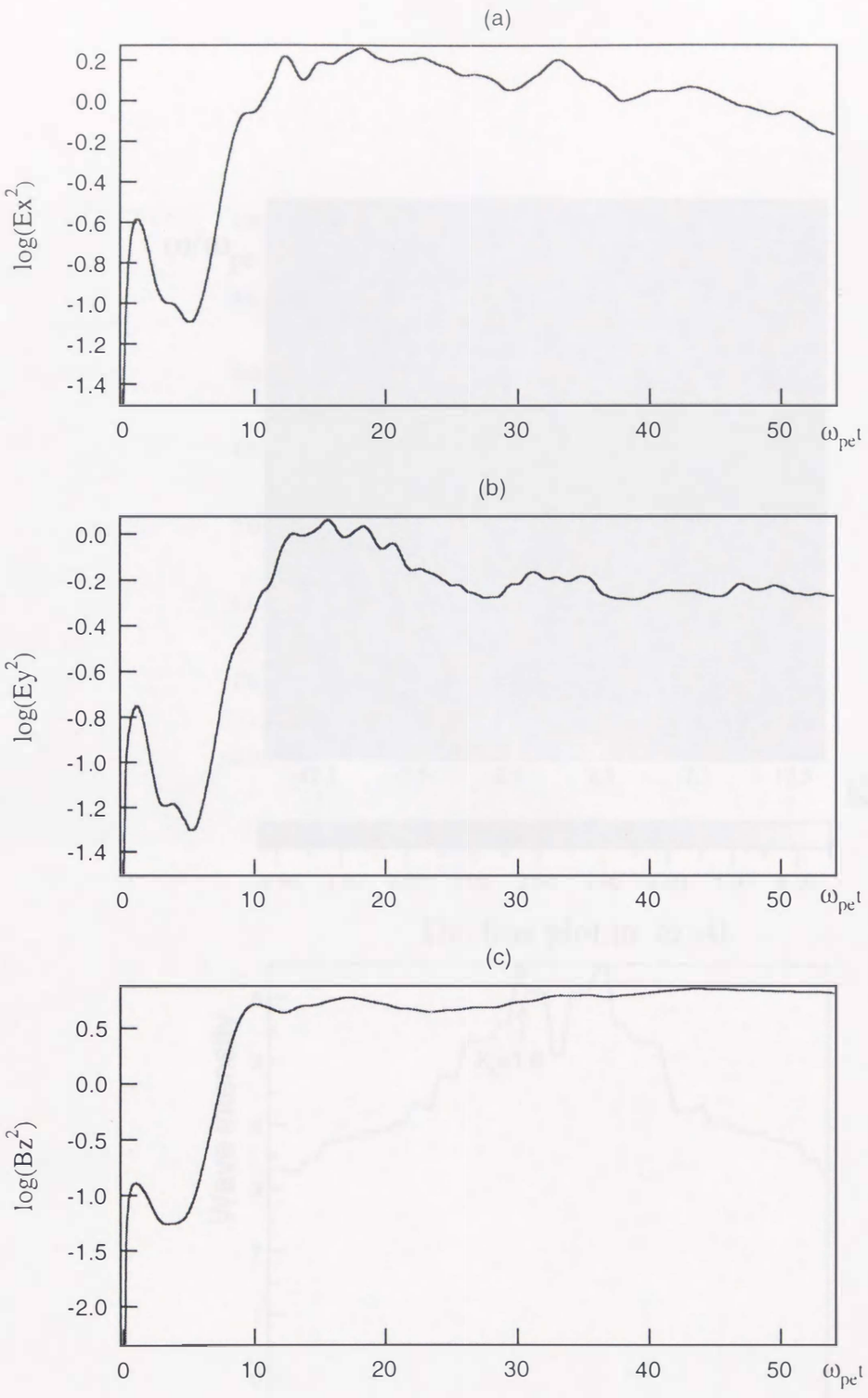
(a)
log(Ex^2)
0.2
0.0
-0.2
-0.4
-0.6
-0.8
-1.0
-1.2
-1.4
0
10
20
30
40
50
$\omega_{pe}t$
(b)
log(Ey^2)
0.0
-0.2
-0.4
-0.6
-0.8
-1.0
-1.2
-1.4
0
10
20
30
40
50
$\omega_{pe}t$
(c)
log(Bz^2)
0.5
0.0
-0.5
-1.0
-1.5
-2.0
0
10
20
30
40
50
$\omega_{pe}t$

Figure 2-6

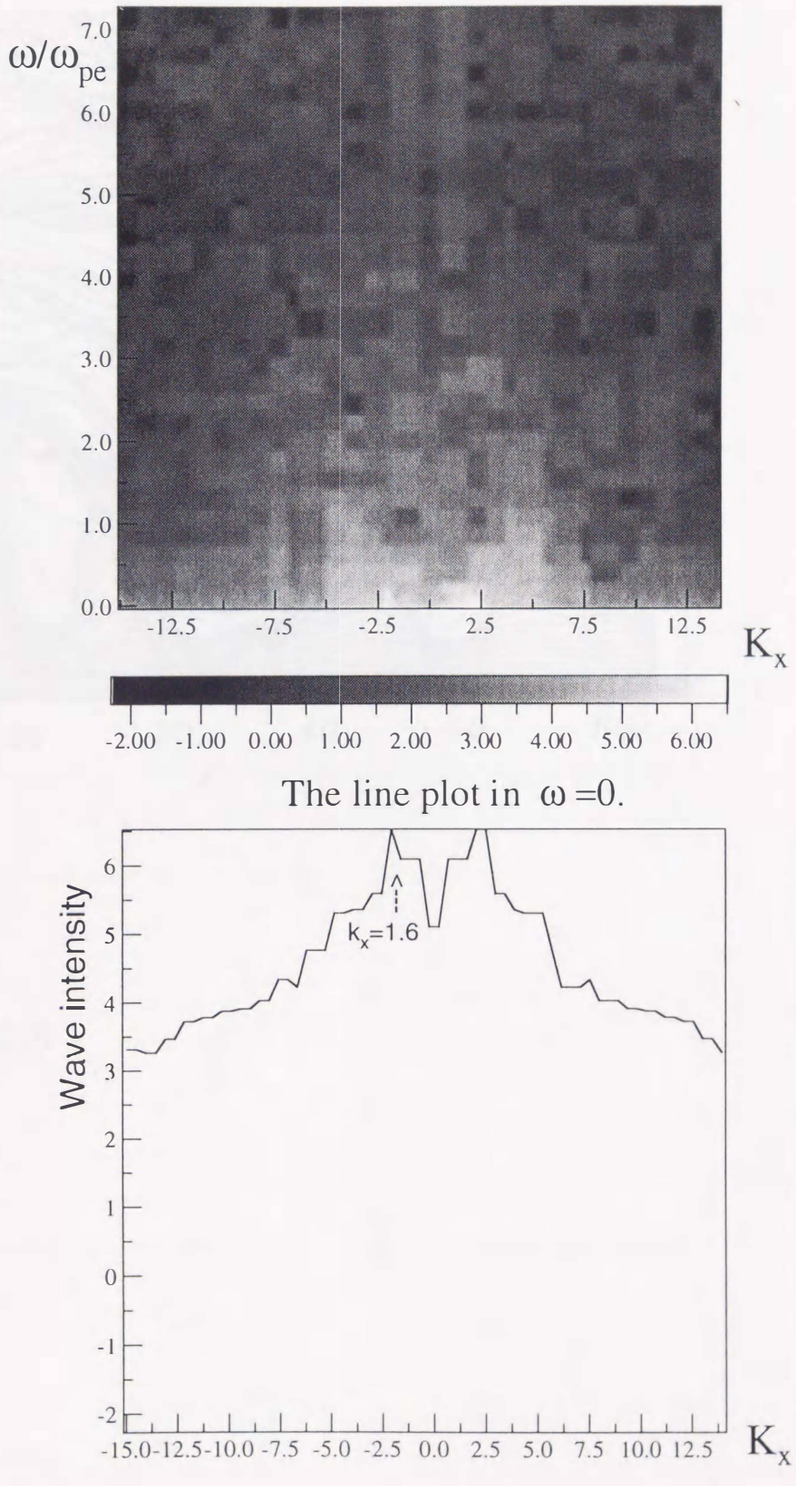
ω/ω_pe
7.0
6.0
5.0
4.0
3.0
2.0
1.0
0.0
-12.5
-7.5
-2.5
2.5
7.5
12.5
K_x
-2.00 -1.00 0.00 1.00 2.00 3.00 4.00 5.00 6.00
The line plot in ω =0.
Wave intensity
k_x=1.6
6
5
4
3
2
1
0
-1
-2
-15.0-12.5-10.0 -7.5 -5.0 -2.5 0.0 2.5 5.0 7.5 10.0 12.5
K_x

Figure 2-7

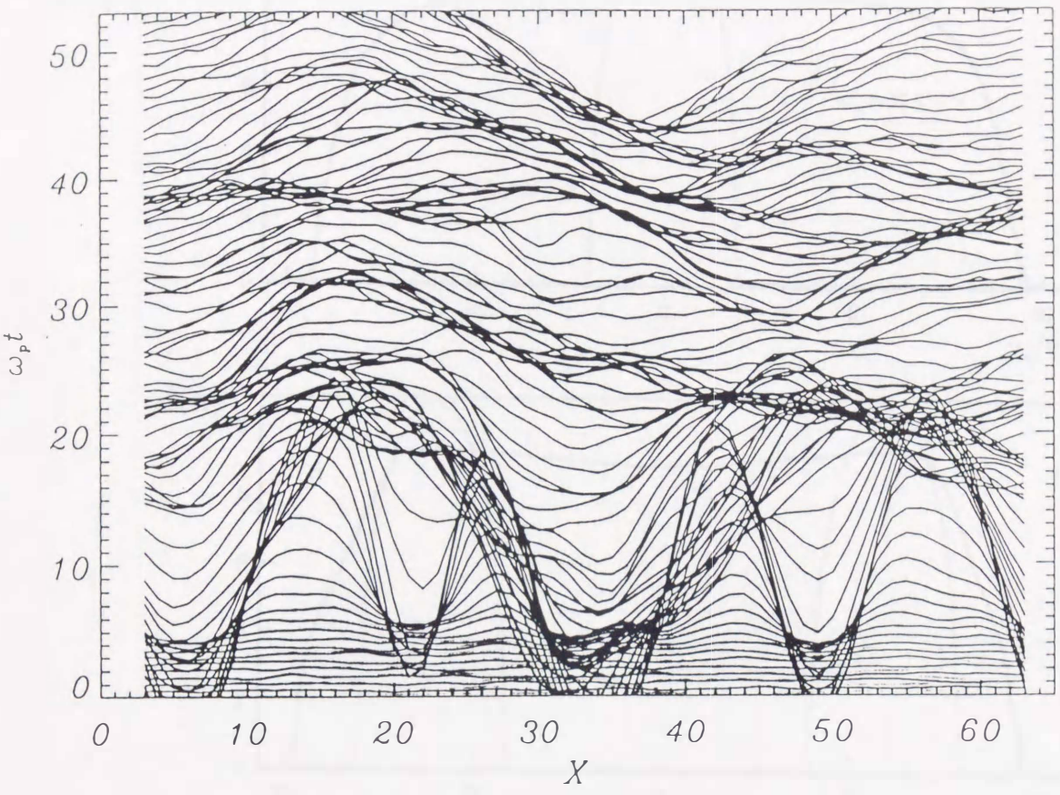

Figure 2-8

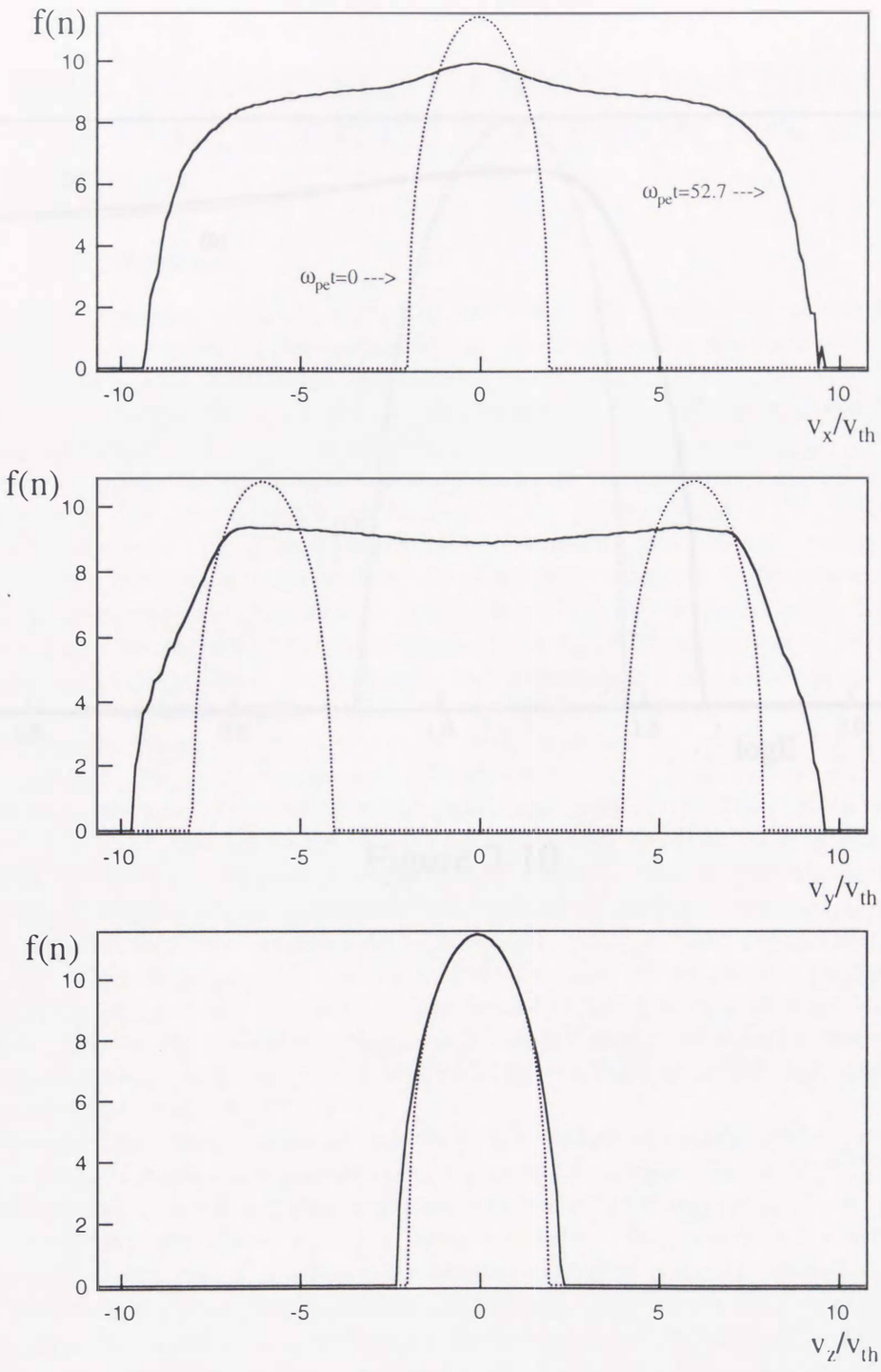
f(n)
10
8
6
4
2
0
-10
-5
0
5
10
v_x/v_{th}
$\omega_{pe}t=0$ --->
$\omega_{pe}t=52.7$ --->
f(n)
10
8
6
4
2
0
-10
-5
0
5
10
v_y/v_{th}
f(n)
10
8
6
4
2
0
-10
-5
0
5
10
v_z/v_{th}

Figure 2-9

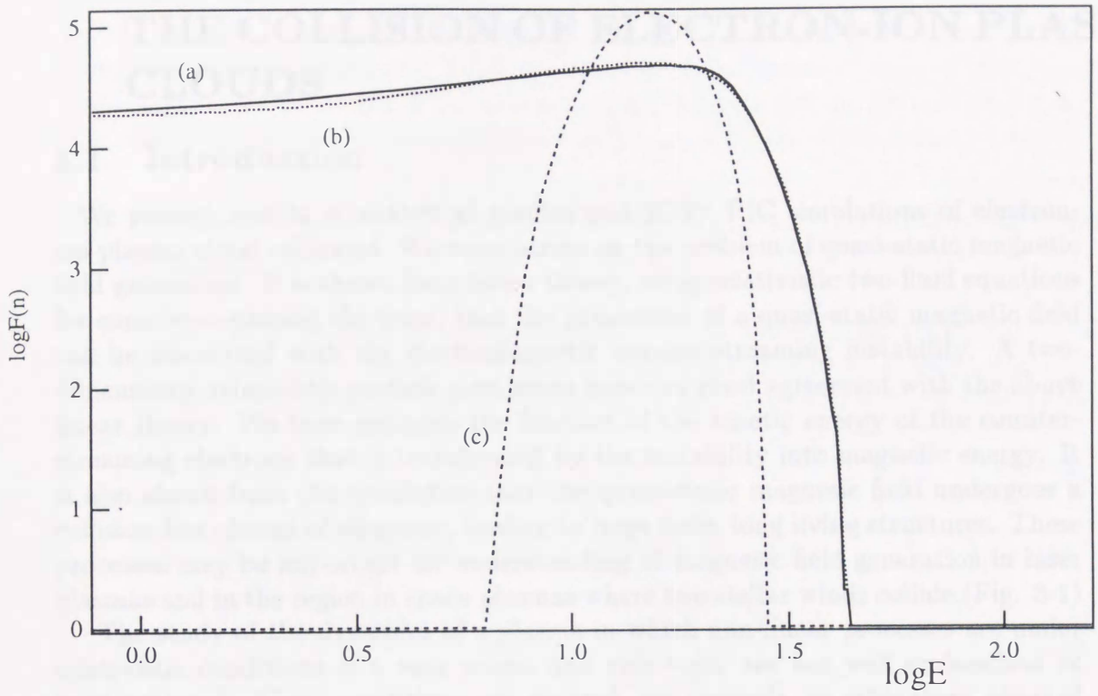

Figure 2-10

3 MAGNETIC FIELD GENERATION DURING THE COLLISION OF ELECTRON-ION PLASMA CLOUDS

3.1 Introduction

We present results of analytical studies and 2D3V PIC simulations of electron-ion plasma cloud collisions. We concentrate on the problem of quasi-static magnetic field generation. It is shown from linear theory, using relativistic two-fluid equations for counter-streaming electrons, that the generation of a quasi-static magnetic field can be associated with the electromagnetic counter-streaming instability. A two-dimensional relativistic particle simulation provides good agreement with the above linear theory. We then estimate the fraction of the kinetic energy of the counter-streaming electrons that is transformed by the instability into magnetic energy. It is also shown from the simulation that the quasi-static magnetic field undergoes a collision-less change of structure, leading to large scale, long living structures. These processes may be important for understanding of magnetic field generation in laser plasmas and in the region in space plasmas where two stellar winds collide.(Fig. 3-1)

The study of the dynamics of a plasma in which non-linear processes are under relativistic conditions is a very recent and rich topic are not well understood or even explored. These conditions are realized, for example, in laboratory plasmas interacting with subpicosecond, multi-terawatt laser pulses[10] with the intensity up to $10^{19-21}\ W/cm^2$, and are also of interest for high energy astrophysics[11,12]. For the plasmas under such conditions it is typical a presence of the fast particle streams with relatively high density. It is known that counter-streaming plasmas are subject to a host of instabilities. In the case of relativistic plasmas, excitation of electromagnetic modes is as important as that of electrostatic modes because the factor v/c is of the order of one. Moreover, in the case of colliding relativistic electron-ion streams in which the net electric charge and current vanish, we expect to see electromagnetic mode excitation that is similar to the Weibel[3] instability in a plasma with anisotropic temperature.

Recently the Weibel instability has been the subject of detailed investigations in the study of quasi-static magnetic field generation in laser plasmas[6,13,15]. The Weibel instability in the nonlinear stage leads to formation of large scale, long-living electron vortices associated with the magnetic fields. This provides the generic mechanism of generation of quasi-static magnetic fields in plasmas, which may be also important in the origin of cosmical magnetic field (Kronberg[7], Kulsrud et al.[8]).

In the previous section, we investigated the dynamics of cloud collision in electron-positron plasmas. They showed the generation of magnetic fields and production of high energy particles. In this section we investigate physical processes during the collision of counter-streaming electron-ion plasmas using a relativistic two-fluid model and a relativistic particle simulation.

In Section 3.2 we present a linear theory derived from the relativistic two-fluid model of counter-streaming electrons, and show the excitation of strong electromag-

netic perturbations associated with quasi-static magnetic fields. In Section 3.3 we show results from a two-dimensional relativistic particle simulation. In the linear regime there is a good agreement between linear theory and simulations. In the nonlinear stage, the magnetic field can undergo collision-less change of structure, and a large scale structure of the magnetic field is produced. In the section 3.5 we summarize our results and briefly discuss some implications of the present process.

3.2 Linear Theory of the Electro-Magnetic Counter-Streaming Instability

The dynamics of counter-streaming electron-ion plasmas with velocities $\mathbf{v}_{ea}$, here and below $e = (electron)$ and $a = 1, 2$ are the two counter-streaming components of particles, is described by the hydrodynamic equations with ions are assumed to be immobile:

$$\frac{\partial n_{ea}}{\partial t} + \nabla \cdot n_{ea}\mathbf{v}_{ea} = 0, \tag{14}$$

$$\frac{\partial \mathbf{P}_{ea}}{\partial t} + \mathbf{v}_{ea} \cdot \nabla \mathbf{P}_{ea} = -(\mathbf{E} + \mathbf{v}_{ea} \times \mathbf{B}), \tag{15}$$

$$\nabla \times \mathbf{E} = -\frac{\partial \mathbf{B}}{\partial t}, \tag{16}$$

$$\nabla \cdot \mathbf{E} = -\sum_a n_{ea}, \tag{17}$$

$$\nabla \times \mathbf{B} = -\frac{\partial \mathbf{E}}{\partial t} + \sum_a \mathbf{J}_{ea}, \tag{18}$$

$$\nabla \times \mathbf{B} = 0, \tag{19}$$

where

$$\mathbf{v}_{ea} = \frac{\mathbf{P}_{ea}}{(1 + \mathbf{P}_{ea}{}^2)^{\frac{1}{2}}}, \tag{20}$$

$$\mathbf{J}_{ea} = -n_{ea}\mathbf{v}_{ea}. \tag{21}$$

Here the densities and the velocities are normalized by a characteristic density n, the speed of light c and the time is normalized by the electron plasma frequency $\omega_{pe} = (4\pi ne^2/m)^{1/2}$.

We consider a case in which the counter-streaming plasmas have equal velocity in the y-direction and density such as no net electric current: $v_{0,e1} = -v_{0,e2}$, $n_{0,e1} = n_{0,e2}$. Linearizing the above set of equations and assuming a dependence of the form $F(x, y, t) = f \exp(i(k_x x + k_y y - \omega t))$, we obtain the following dispersion equation:

$$\begin{aligned}(1 - \Omega_{2e}^{-2})[(1 + \Omega_{4e}^{-2})k_y^2 - \omega^2(1 - \Omega_{1e}^{-2}) - 2\omega k_y(\Omega_{3e}^{-2})] \\ + k_x^2[(1 + \Omega_{4e}^{-2})(1 - \Omega_{1e}^{-2}) + \Omega_{3e}^{-4}] = 0,\end{aligned} \tag{22}$$

where

$$\Omega_{1e}^{-2} = \sum_a \frac{n_{0,ea}}{\Gamma_{ea}\Omega_{ea}^2}, \quad \Omega_{2e}^{-2} = \sum_a \frac{n_{0,ea}}{\Gamma_{ea}^3\Omega_{ea}^2},$$
$$\Omega_{3e}^{-2} = \sum_a \frac{n_{0,ea}v_{0,ea}}{\Gamma_{ea}\Omega_{ea}^2}, \quad \Omega_{4e}^{-2} = \sum_a \frac{n_{0,ea}v_{0,ea}^2}{\Gamma_{ea}\Omega_{ea}^2}. \tag{23}$$

Here the following notations are used:

$$\Omega_{ea} = \omega - k_y v_{0,ea}, \qquad \Gamma_{ea} = (1 - v_{0,ea}^2)^{-1/2}. \tag{24}$$

We note here that the above dispersion relation is the case derived by Califano et al.[14,15].

We did a numerical calculation to obtain the growth rate of the electromagnetic instability. The parameters used here coincide with those used in the simulation in the next section. We consider collision of two symmetric plasma flows with velocities, $v_0 = 0.56c$ and $-0.56c$, and with equal density.

Figure 3-2 shows the growth rate normalized by ω_{pe} versus the wave-number k_x normalized by c/ω_{pe} for the propagation angle of 82.9 degree from the y-direction. [See 3.4.2]

3.3 Simulation Model

We have performed two sets of numerical simulations with two different PIC codes to study nonlinear aspects of the Weibel instability in initially homogeneous counter-streaming electron flows and in the case of two colliding plasma clouds.

The first problem has been solved with a $2D3V$, fully relativistic electromagnetic particle-in-cell code, described earlier[6]. The grid is $L_x = 128\Delta$ and $L_y = 128\Delta$ with a grid size $\Delta = 0.05c/\omega_{pe}$. Periodic boundary conditions are imposed on particles and fields. The ions are assumed to be at rest. The electrons initially have two counter-streaming components with velocities $v_d = \pm 0.5c$ along the y-coordinate.

The code used to study the second problem is a $2D3V$, fully relativistic electromagnetic particle-in-cell code, modified from the $3D3V$ TRISTAN code (Buneman[16]). The system size is $L_x = 65\Delta$ and $L_y = 1024\Delta$, where $\Delta(= 1)$ is the grid size.(Fig. 3-1) Periodic boundary conditions are imposed on particles and fields. There are 1,331,200 electron-ion pairs filling the entire domain uniformly and keeping the domain charge neutral. Hence the average particle number density is about 20 per cell. The initial state is such that in the region of $Y = (1 \sim 512)\Delta$, the plasma drift velocity is $v_d = 0.56c$ (c is the light speed), with shifted Maxwellian distribution with the thermal velocity $v_{th} = 0.09366c$, and in the region, $Y = (512 \sim 1024)\Delta$, $v_d = -0.56c$. This corresponds to a Lorentz factor $\gamma = (1 - (v_d/c)^2)^{-1/2} = 1.2$. Other parameters are as follows; the mass ratio $m_i/m_e = 1836.2$ (i:ion,e:electron), $\omega_{pe}\Delta t = 0.05$, the electron collisionless skin depth $d_e = c/\omega_{pe} = 9.6\Delta$. Thus the computation box has a size equal $\approx 6.6d_e$ in the $x-$direction and $\approx 106.6d_e$ in the $y-$direction.

The initial electric and magnetic field in both cases is zero. Due to symmetry of the problems under consideration only the z-component of the magnetic field is generated during the electro-magnetic mode excitation.

3.4 Simulation Results

3.4.1 Development of Large-Scale Magnetic Structures in Homogeneous Electron Flows

The results of $2D$ PIC simulations of the electromagnetic mode development in counter-streaming electron flows are presented in Figs. 3-3 and 3-4. In Figure 3-3 the magnetic field (B_z-component) distribution in the $x-y$ plane is presented for several instants of time. Initially at $t = 0$ the small scale structures are presented due to the noise. Then long wavelength modulations with a scale length in the y-direction of the order of the collisionless skin depth d_e appear and almost uniform in the x-direction appear as it is seen for $\omega_{pe}t = 10$. At $\omega_{pe}t = 20$ the modulations in the y-direction perpendicularly to both the initial stream velocities and generated magnetic field increase. Comparison of the magnetic field structures at $\omega_{pe}t = 20$ and $\omega_{pe}t = 30$ demonstrates that long living large-scale structures are formed with the scale of the order of d_e in the y-direction and of the order of $2-3$ d_e along the x-direction. Because the electron motion related to the magnetic field structures is slow compared to the Langmuir wave period the plasma is almost quasineutral. It also is seen in the distribution of the electron density (not presented here) that the density modulations are weak. In this case by virtue of $\nabla \times \mathbf{B} \approx \mathbf{J}$ the localized regions of the magnetic field with alternating polarity correspond to the electron vortex row. The electron vortex rows similar to the von Karman rows in standard hydrodynamics have been observed in the PIC simulations of the laser pulse interaction with plasmas[17] as well as the electron vortex system stability has been investigated[18].

In Fig. 3-4 dependence of the magnetic and electric field in the computation region versus time is presented. The value of the exponential time corresponds to the inverse growth rate of the instability found above.Since initial perturbation was given to the system, it can be seen the minimum.

The PIC simulations of non-symmetric case, when $v_1 = 0.8$, $v_2 = -0.2$, $n_1 = 0.2$ and $n_2 = 0.8$ show similar structure development.

3.4.2 Evolution of the Magnetic Field Structures during Plasma Cloud Collisions

We investigated several cases of electron-ion plasma cloud collisions,by using two-dimensional fully relativistic particle code and here we show only one case of them. The most important result is the generation of the magnetic field in the direction perpendicular to the counter-stream direction from the initial state with no-magnetic field.

Figure 3-5 shows the time development of the magnetic field (B_z) structures in the $x-y$ plane. As seen in Fig.3-5(a), initially (for $\omega_{pe}t = 10$) there appears very coherent structures with positive and negative magnetic polarities. This corresponds

to the filamentation of the plasma with creation of the current sheet system with the current sheets situated where the magnetic field changes sign. The characteristic scale of the current sheet is about $\lambda_x = 0.37d_e$ in the transverse direction along the $x-$axis and about $\lambda_y = 2.1d_e$ in the longitudinal direction along the $y-$axis.

As time goes on, the front of both streams propagates further and behind the front the bending and coalescence of the filaments occur as it is seen in Fig.3-5(b) where the magnetic field pattern is shown for $\omega_{pe}t = 31$. This process makes the characteristic scale length of the magnetic field larger. The coalescence process of filaments first becomes apparent after about $\omega_{pe}t = 31$. Asymptotically, at $\omega_{pe}t = 52.7$, in Fig.3-5(c), we see formation of large scale, long lived magnetic structures with the size of the order of $2\pi c/\omega_{pe}$. The alternating polarity corresponds to electric current distributions in the x, y-plane of the form of antisymmetric vortex flow. Figure 3-6 shows the time history of electric ($E_x{}^2$, $E_y{}^2$) and magnetic ($B_z{}^2$) field energy.

By using the final value of the magnetic energy, we can estimate the energy conversion rate from the initial electron kinetic flow energy. We find that the energy conversion rate is about 3.7%.

Figure 3-7 shows the time history of electric ($E_x{}^2$, $E_y{}^2$) and magnetic ($B_z{}^2$) field energy normalized by $2VtL_x/L_xL_y$,where V is the plasma front velocity of the streams, assumed to be constant. Thus they give the dependencies of the average values of the fields v.s. time. As seen in Figs. 3-6(a) and 3-6(b), almost the same amount of electrostatic wave energy is excited in the x- and y-directions due to electron-counter stream instability. From a Fourier analysis of the wave patterns in E_x and E_y, we find that the electrostatic energy is associated with the Langmuir waves. The propagation direction in which the waves are excited is oblique from the x-direction. The magnitude of the growth rate calculated from the dispersion relation is about 0.55 with $k_x = 1.8$ and $k_y = 0.23$ while the value of growth rate calculated from the time history of magnetic field energy is about 0.446.The calculation of k_x and k_y are the same as the electron-positron case.(see section 3.4)

We did several other cases with different counter-streaming flow velocities, and also where one cloud is at rest. From these results we found that the important parameter for magnetic field generation is the relative velocity of clouds. The ion dynamics does not affect the generation of the magnetic field. Only counter-streaming electrons contribute to the generation of the magnetic field.

3.5 Discussion and Summary

It is shown from linear theory using relativistic two-fluid equations for electron-ion plasmas, that the generation of a quasi-static magnetic field is associated with the counter-streaming electro-magnetic instability of electron-ion plasmas. A two-dimensional relativistic particle simulation is in good agreement with the above linear theory and furthermore, in the nonlinear stage of the instability, shows that about 3.7 % of the initial plasma flow energy can be converted to magnetic field energy. It is also shown from the simulation that the generated quasi-magnetic field undergoes a change in structure through coalescence of magnetic filaments, leading

to large scale structures and the production of high-energy particles.(Fig. 3-8) Figure 3-8 show the electron energy spectrum in the each state of the simulation. These process may be important for understanding of the production of high-energy particles in the region of two colliding stellar winds. We notice here that discussed above dependence of the magnetic field structures on the distance from the cloud fronts can explain properties of the small scale magnetic field observed in PIC simulations of the laser pulse interaction with plasmas[17]. In this case the small scale magnetic structures were generated outside both the laser pulse and the wake plasma wave. A magnetic field with small scale structure is formed as a result of the development of the Weibel instability due to the multi-stream motion of the electrons thrown out of the wake in the transverse direction[18].

3.6 Summary

We investigated simulations of electron-positron two-streams collision and electron-ion two-streams collision, by using a two-dimensional relativistic particle code. We concentrate on the problem of quasi-static magnetic field generation. The quasi-static magnetic field undergoes a collision-less change of structure, leading to large scale, long living structures. It is shown from linear theory, using relativistic two-fluid equations for counter-streaming, that the generation of a quasi-static magnetic field can be associated with the electromagnetic counter-streaming instability. A two-dimensional relativistic particle simulations provided a good agreement with both electron-positron and electron-ion linear theory. The energy conversion rate from the initial plasma flow energy is about 5.3 % (electron-positron) and 3.7% (electron-ion). This conversion is very effective in real cosmic plasmas. And in the simulation, we could see the particle acceleration with relativistic energy in x and y direction. The production of high-energy particles is very important for understanding the region of two colliding stellar and colliding pulsar winds.

By the way, all of the cases we have simulated by computer were two-dimensional simulation. But the phenomena of real universe is three-dimensional, so after this we think that we must expand into the three-dimensional code on the simulation we had been doing.

And as the future plans, we will compare their results to simulation by using three-dimensional code. Still more we will expand the linear theory into three-dimensional equations and compare the result of their simulations to three-dimensional linear theory. That is correspond to compare in condition near the real universe space. About the point of generation of magnetic field, we want to simulate in detail not only to see the collision region, but also to see the region that particles have passed. (section 5) And we will study how much value and how structures they have, and what is the magnetic value remaining in the space, by using a two-dimensional particle code as same. So it may be possible to do a discussion about origin of magnetic fields in the universe which may be formed at early universe and we hope that their studies may contribute to development of plasma physics.

Figure captions

Figure 3-1. Linear growth rate normalized by ω_{pe} vs the wavenumber k_x normalized by c/ω_{pe} for a propagation angle of 82.9^o,with respect to the y-direction. The counter-streaming velocity is $v_o = 0.56c$.

Figure 3-2. The image of counter-stream from binary star and system domain.$v_1 = 0.56c$, $v_2 = -0.56c$ (c is light velocity).

Figure 3-3. Time development of the magnetic field (B_z) structures in the x-y plane. (a) $\omega_{pe}t = 0$, (b) $\omega_{pe}t = 10$, (c) $\omega_{pe}t = 20$,(d) $\omega_{pe}t = 30$.

Figure 3-4. Time history of mean magnetic field; (1) B_z and electric fields (2) E_x ,(3) E_y energy densities.

Figure 3-5. Time development of the magnetic field (B_z) structures in the x-y plane. (a) $\omega_{pe}t = 10$, (b) $\omega_{pe}t = 31$, (c) $\omega_{pe}t = 52.7$.

Figure 3-6. Time history of electric field energy density; (a) ${E_x}^2$, (b) ${E_y}^2$ and magnetic field energy density; (c) ${B_z}^2$.

Figure 3-7. Time history of electric field energy; (a) ${E_x}^2$, (b) ${E_y}^2$ and magnetic field energy; (c) ${B_z}^2$, normalized by $2VtL_x/L_xL_y$, where V is the plasma front velocity of the streams, assumed constant.

Figure 3-8. The electron energy spectrum in each state of the simulation. E is total kinetic energy of particles. (a) shows the initial energy distribution of electron particles species. (a) $\omega_{pe}t = 10$, (b) $\omega_{pe}t = 31$, (c) $\omega_{pe}t = 52.7$.

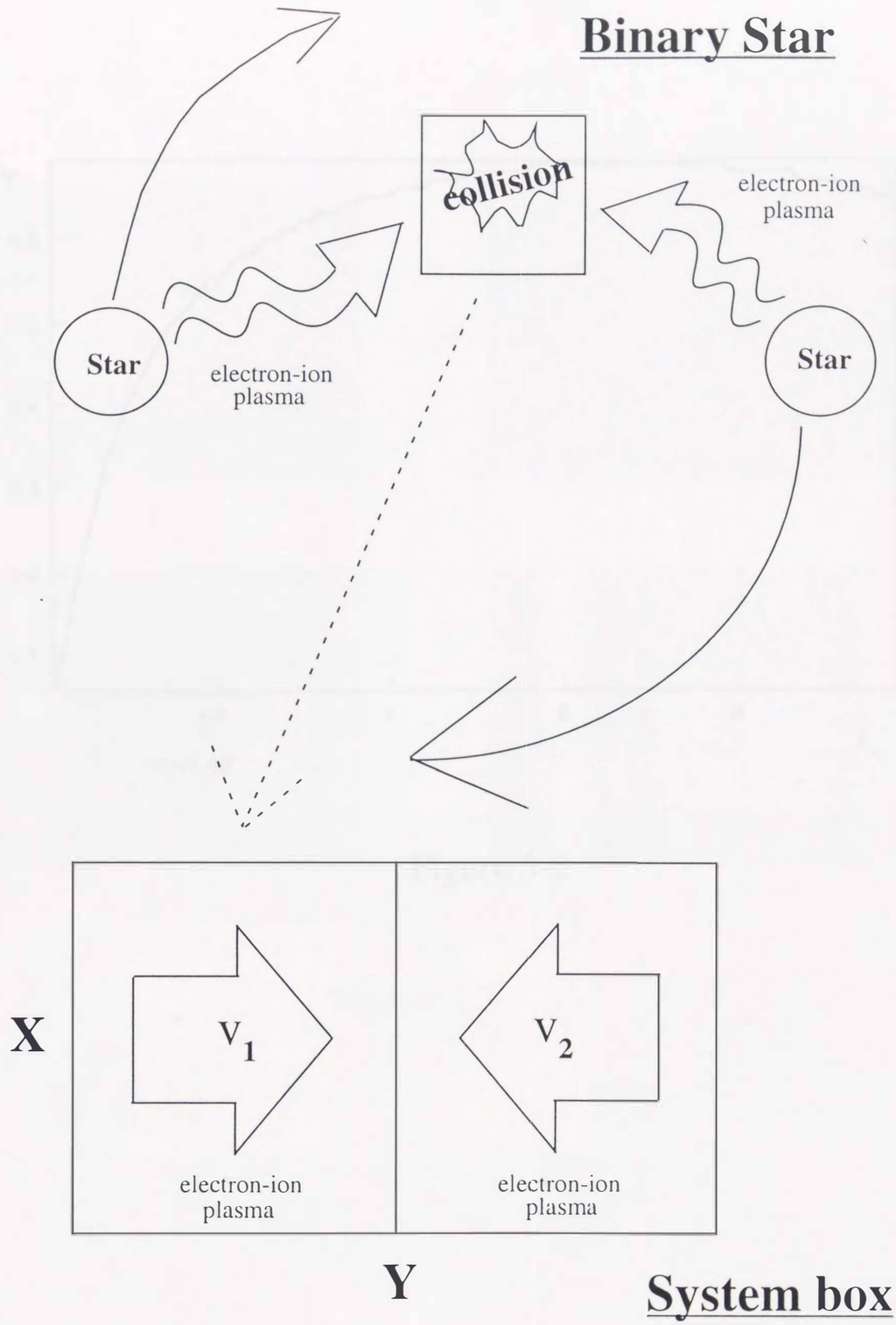
Binary Star
collision
electron-ion plasma
Star
electron-ion plasma
Star
X
V_1
V_2
electron-ion plasma
electron-ion plasma
Y
System box

Figure 3-1

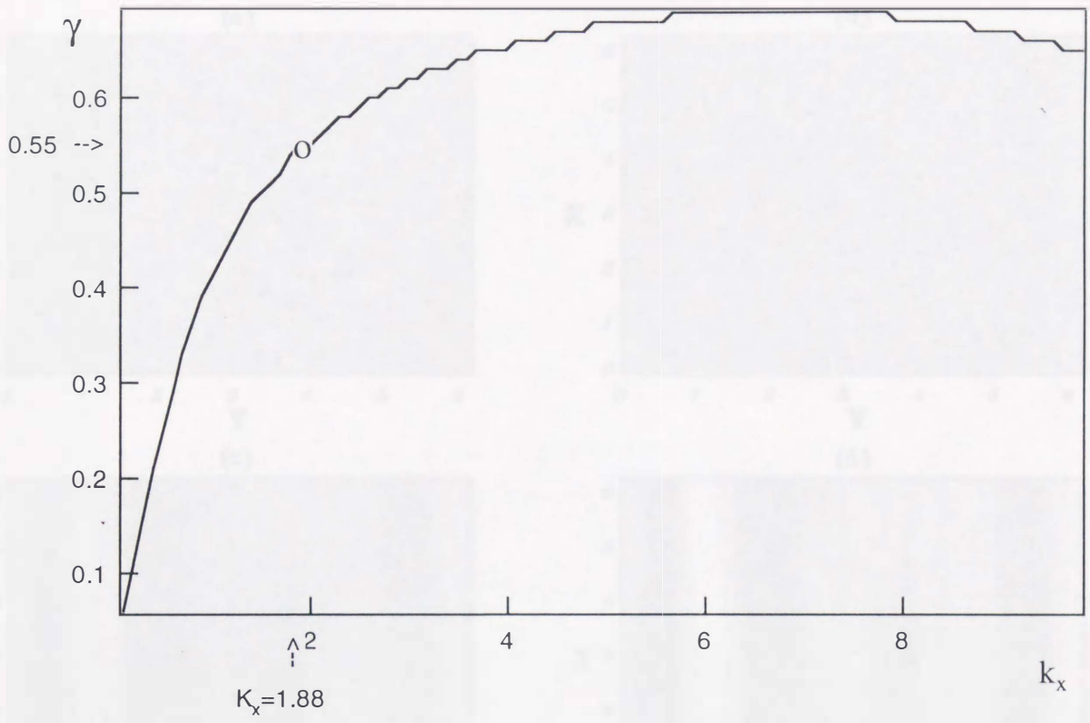

Figure 3-2

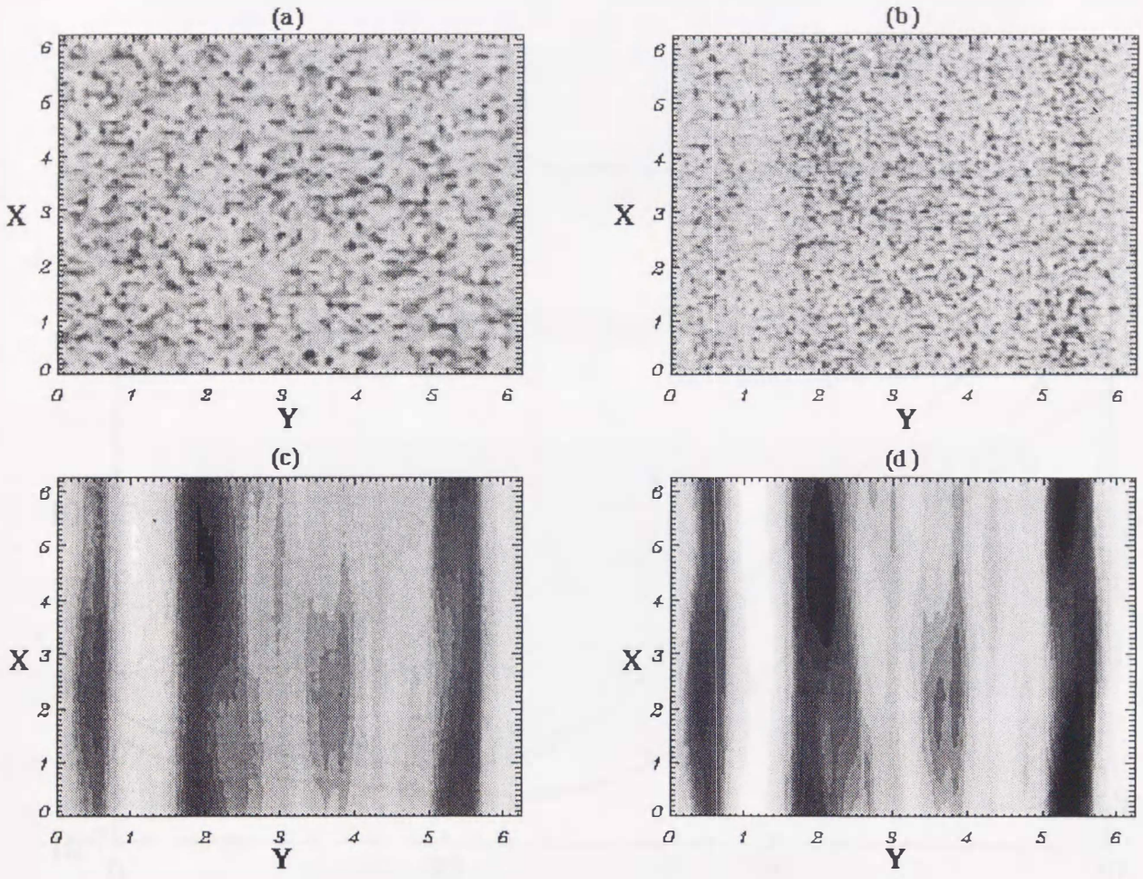

Figure 3-3

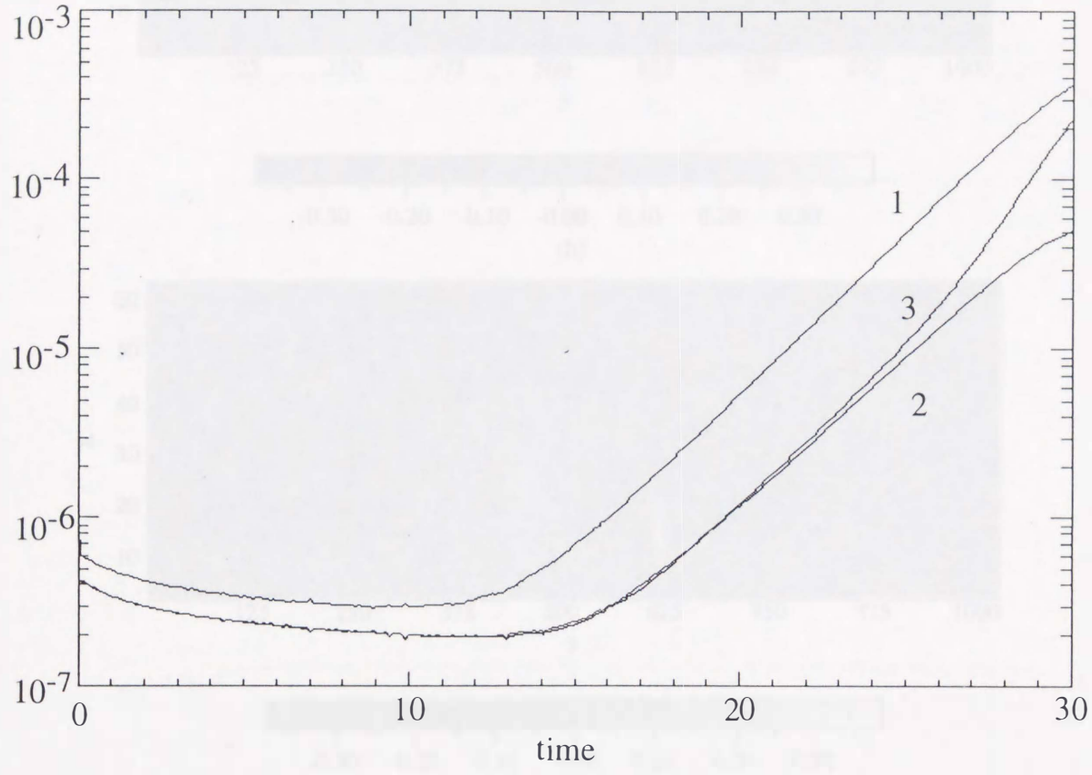

Figure 3-4

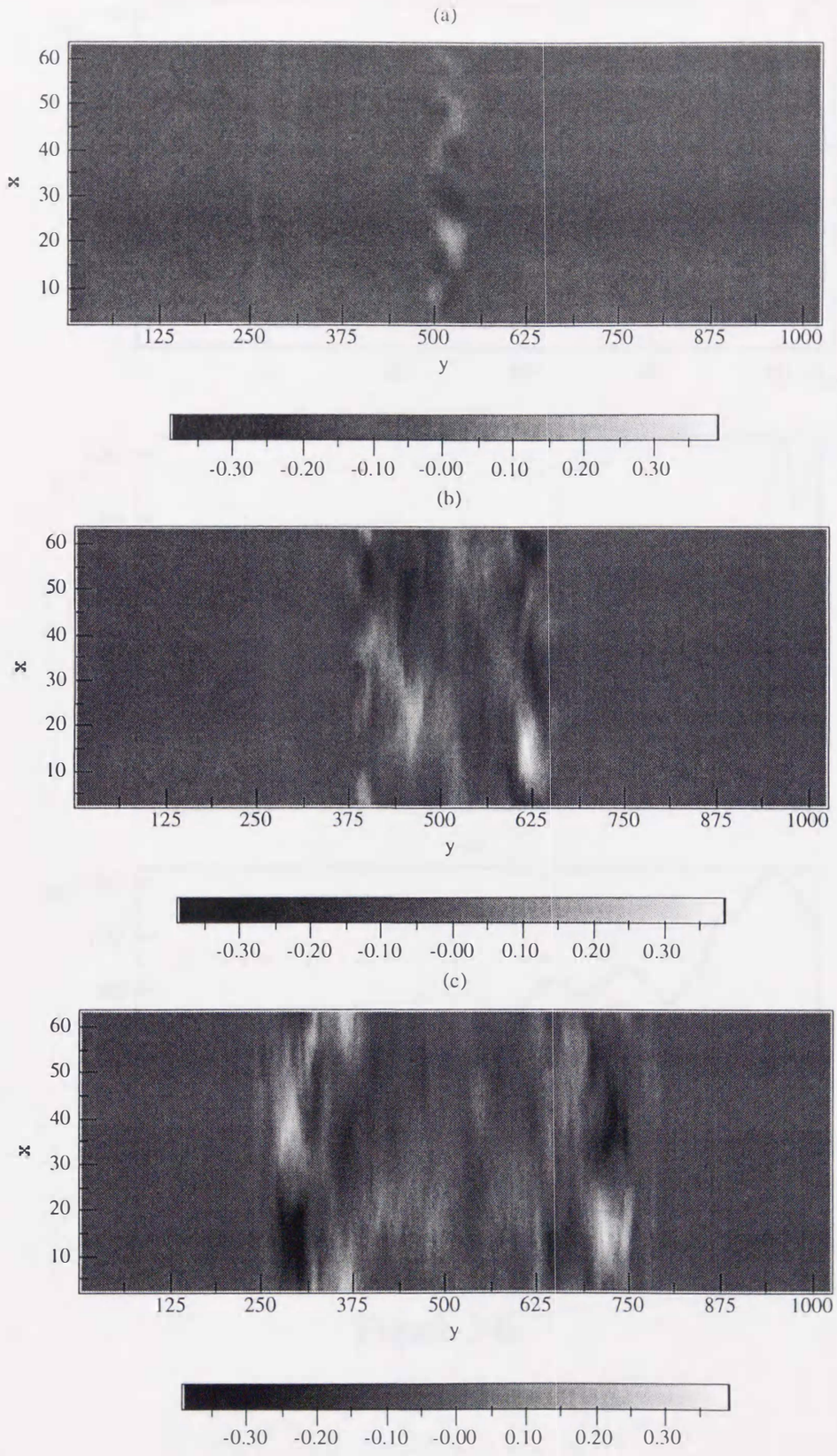
(a)
60
50
40
30
20
10
x
125
250
375
500
625
750
875
1000
y
-0.30
-0.20
-0.10
-0.00
0.10
0.20
0.30
(b)
60
50
40
30
20
10
x
125
250
375
500
625
750
875
1000
y
-0.30
-0.20
-0.10
-0.00
0.10
0.20
0.30
(c)
60
50
40
30
20
10
x
125
250
375
500
625
750
875
1000
y
-0.30
-0.20
-0.10
-0.00
0.10
0.20
0.30

Figure 3-5

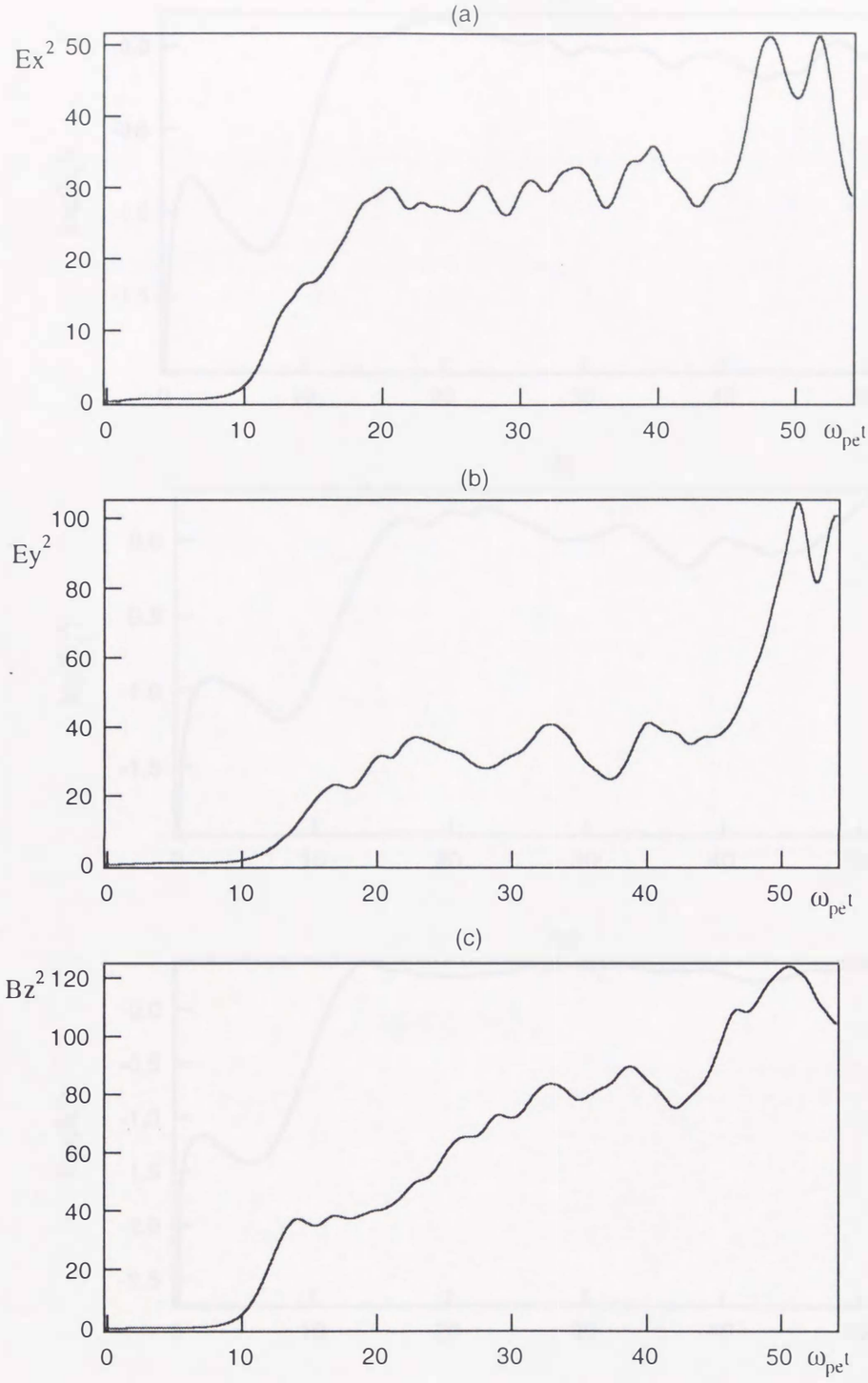
(a)
Ex^2
50
40
30
20
10
0
0
10
20
30
40
50
$\omega_{pe}t$
(b)
Ey^2
100
80
60
40
20
0
0
10
20
30
40
50
$\omega_{pe}t$
(c)
Bz^2
120
100
80
60
40
20
0
0
10
20
30
40
50
$\omega_{pe}t$

Figure 3-6

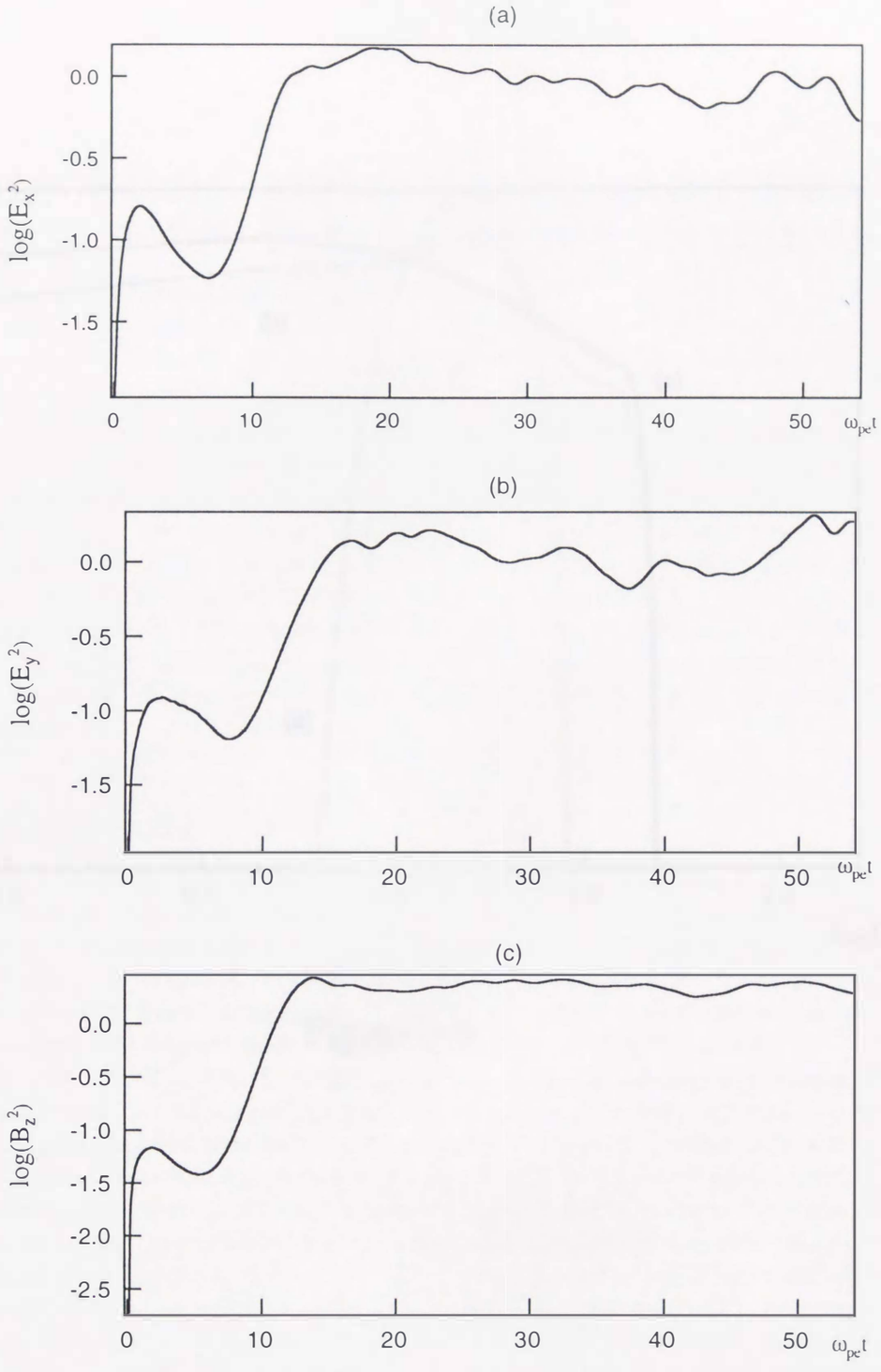
(a)
0.0
-0.5
-1.0
-1.5
log(E_x^2)
0
10
20
30
40
50
ω_pe t
(b)
0.0
-0.5
-1.0
-1.5
log(E_y^2)
0
10
20
30
40
50
ω_pe t
(c)
0.0
-0.5
-1.0
-1.5
-2.0
-2.5
log(B_z^2)
0
10
20
30
40
50
ω_pe t

Figure 3-7

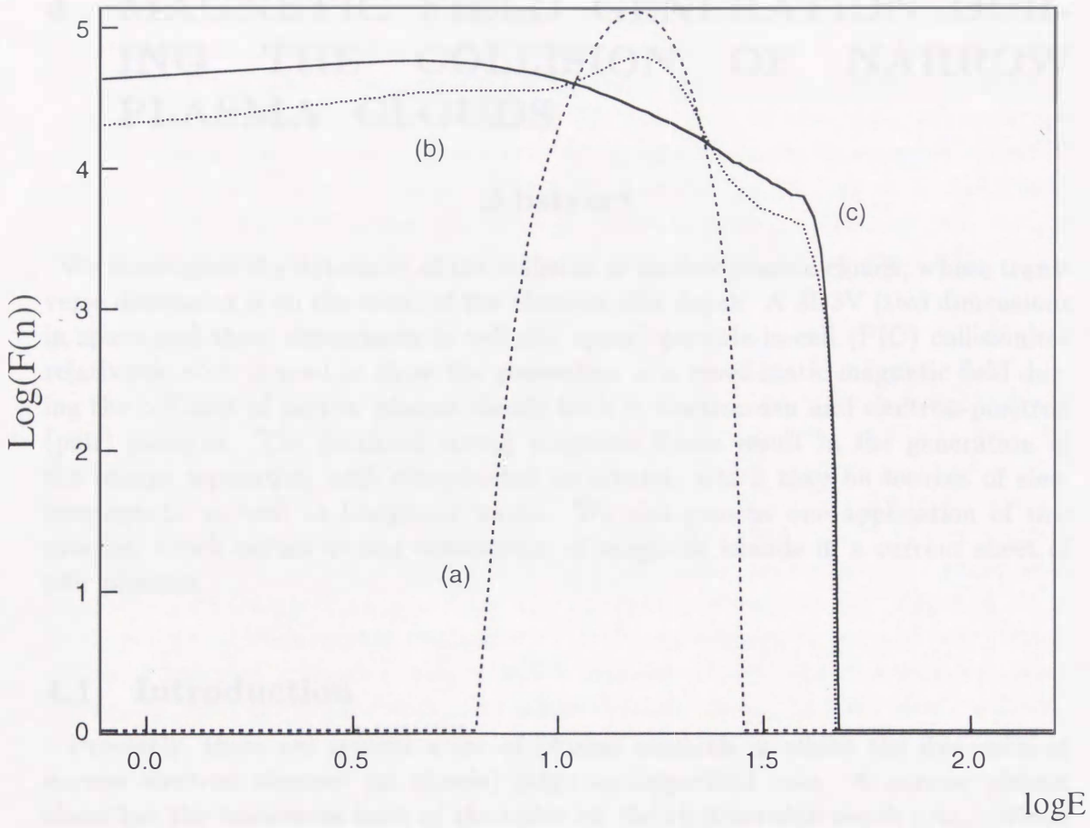

Figure 3-8

4 MAGNETIC FIELD GENERATION DURING THE COLLISION OF NARROW PLASMA CLOUDS

Abstract

We investigate the dynamics of the collision of narrow plasma clouds, whose transverse dimension is on the order of the electron skin depth. A 2D3V (two dimensions in space and three dimensions in velocity space) particle-in-cell (PIC) collisionless relativistic code is used to show the generation of a quasi-static magnetic field during the collision of narrow plasma clouds both in electron-ion and electron-positron (pair) plasmas. The localized strong magnetic fluxes result in the generation of the charge separation with complicated structures, which may be sources of electromagnetic as well as Langmuir waves. We also present one application of this process, which occurs during coalescence of magnetic islands in a current sheet of pair plasmas.

4.1 Introduction

Presently, there are several areas of plasma research in which the dynamics of narrow electron streams (or clouds) plays an important role. A narrow plasma cloud has the transverse scale of the order on the electron skin depth c/ω_{pe} (where c is the speed of light and ω_{pe} the electron plasma frequency). Some examples with such situations are found in magnetic reconnection studies,[20] dynamics of narrow electron streams,[21] satellite and rocket observations[22] and laser plasmas.[13]

On the other hand, the study of the nonlinear processes in a relativistic plasma is a very recent and rich topic that is not yet fully understood or well explored. These relativistic plasma conditions have been realized in laboratory plasmas interacting with laser pulses[13] with intensities as large as $10^{19-21}\ W/cm^2$ and are also of interest in high-energy astrophysics. In relativistic plasmas, the excitation of electromagnetic modes is as important as that of electrostatic modes because the particle velocities are of the order of the speed of light, i.e., $v/c \approx 1$. In the case of colliding relativistic electron-ion plasmas, in which the net electric charge and current vanish, we expect to see the excitation of an electromagnetic mode similar to the Weibel[3] instability that occurs in a plasma with anisotropic temperature. Recently, counter-streaming electromagnetic instability has been the subject of a detailed investigation in the study of the generation of quasi-static magnetic fields in laser plasmas.[6] Kazimura et al.[23,24] investigated the dynamics of collisions of clouds of both electron-ion and pair plasmas. They revealed that magnetic fields are generated and high-energy particles are produced.

In this paper,we focus on the dynamics of the collision of narrow plasma clouds in both electron-ion and pair plasmas, by using a 2D3V particle-in-cell (PIC) collisionless relativistic code. We show the generation of a quasi-static magnetic field during

the collision of narrow plasma clouds in both electron-ion and electron-positron (pair) plasmas. The localized strong magnetic fluxes result in the generation of the charge separation with complicated structures, which may be sources of electromagnetic as well as Langmuir waves. We also present one application of this process, which occurs during coalescence of magnetic islands in a current sheet of pair plasmas. In §4.2 we present the simulation model. In §4.3 we show the results of two-dimensional relativistic collisionless PIC simulations. We also present one application of this process. In the final section we summarize our results.

4.2 Simulation Model

The code used here is $2D3V$ (two dimensions in space and three dimensions in velocity space) ,a fully relativistic electromagnetic particle-in-cell code, modified from the $3D3V$ TRISTAN code[16] (Buneman). The system size is $L_x = 100\Delta$ and $L_y = 200\Delta$, where $\Delta = 1.0$ is the grid size. Periodic boundary conditions are imposed on the particles and the fields. We investigate both cases of electron-ion and pair plasmas. The average particle number density in background plasmas is approximately 20 particles per cell. The electron collisionless skin depth is $d_e = c/\omega_{pe} = 9.48\Delta$. We consider two cases in which the transverse scale of two plasma clouds is 10Δ with a number density of 100 particles per cell and 20Δ with a number density of 200 particles per cell. The plasma cloud velocity is fixed as $\mathbf{v}_0 = 0.5c\mathbf{e}_y$ ($\mathbf{e}_y$ is unit vector) with a shifted Maxwellian distribution with thermal velocity $v_{th} = 0.2c$ in the region $45\Delta < x < 55\Delta$ and $20\Delta < y < 40\Delta$, while in the region $45\Delta < x < 55\Delta$ and $160\Delta < y < 180\Delta$, with $\mathbf{v}_0 = -0.5c\mathbf{e}_y$. The other parameters are as follows: the mass ratio for the electron-ion case is $m_i/m_e = 64$, $\omega_{pe}\Delta t = 0.052$, where Δt is the integration time step. Due to the symmetry of the configuration in both cases, only the z-component of the magnetic field is generated during the electromagnetic mode excitation.

4.3 Simulation Results

4.3.1 Magnetic Field Generation

We present the simulation results on quasi-static magnetic field generation during collision of two clouds for both pair plasmas and electron-ion plasmas. The physical mechanism of the generation of the magnetic fields is due to the electromagnetic counter-streamings instability discussed by Kazimura et al.[6,23,24] Figure 4-1 shows the case of pair plasmas. Figures 4-1(a) and 4-1(b) show the electron spatial distributions in the x-y plane at $\omega_{pe}t = 0$, and $\omega_{pe}t = 15$, respectively. Figure 4-1 (c) presents the time history of the magnetic field energy $\int\int dxdyB_z(x,y)^2/2\mu_0$ (where μ_0 is taken as $\mu_0 = 4$) in the system. As seen in this figure, strong enhancement of the magnetic field B_z appears just after collision of the two clouds. As the time change of the spatial distribution of the generated magnetic field is slow compared with ${\omega_{pe}}^{-1}$, we may refer to the magnetic field as quasi-static evolution.

Figure 4-2 shows the case of electron-ion plasmas, using the mass ratio $m_i/m_e = 64$. Figures 4-2(a) and 4-2(b) show the electron spatial distributions in the x-y plane

at $\omega_{pe}t = 0$, and $\omega_{pe}t = 15$, respectively. Figure 4-2(c) presents the time history of the magnetic field energy $\int\int dxdyB_z(x,y)^2/2\mu_0$ in the system. As seen in Fig. 4-2(c), the magnetic field generation in electron-ion plasmas is different from the case of pair plasmas. The magnetic field generation occurs before the collision of the two clouds. As the initial cloud electron temperature is equal to the ion cloud temperature, a fraction of the cloud electrons begins to move faster than the ions. But within approximately the plasma oscillation period, the electrons are forced to return to cancel the charge separation. These transient relative motions create an electric current along the cloud, which results in the magnetic field generation B_z around the boundary of the cloud before the cloud collision. However, this transient current generation in the clouds of pair plasmas does not occur, and the magnetic field generation only appears after cloud collisions. Because of this physical difference, in the time history of energy, there is the minimum in the case of electron-ion plasma. We note here that the total energy (kinetic energy + field energy) conservation rate during the simulation is about 3% for the pair plasma and about 0.02% for the electron-ion plasma, respectively.

In order to study the spatial structure of the generated quasi-static magnetic field, we simulated two cases with different transverse widths, 10Δ with a number density of 100 particles per cell and 20Δ with a number density of 200 particles per cell. Figure 4-3 shows the case of pair plasmas. Figure 4-3(a) and 4-3(b) show the spatial distributions of the generated magnetic field at $\omega_{pe}t = 15$ for transverse width 10Δ with a number density of 100 particles per cell and transverse width 20Δ with a number density of 200 particles per cell, respectively. As seen in Fig. 4-3(a), the strongest localized magnetic field B_z with a negative polarity is produced near the center of the coalesced cloud. When the transverse scale of the clouds is twice as large as that in the previous case, a pair of magnetic polarities appear in the coalesced cloud as seen in Fig. 4-3(b). These quasi-periodic structures of magnetic field generation were confirmed by theory as well as simulation by Kazimura et al.[7,8] When the transverse scale of the colliding clouds is on the order of the electron skin depth, a pair of the magnetic fields occurs.

Figure 4-3(c) and 4-3(d) show the spatial distributions of the charge density $(\rho_+ - \rho_-)$ for transverse width 10Δ with number density of 100 particles per cell and transverse width 20Δ with a number density of 200 particles per cell, respectively. As seen in Fig. 4-3(c), a quadrupole-like structure appears in the charge density. While in Fig. 4-3(d), a pair of the quadrupole structures appears for the case of the coalesced cloud with a width twice as larger as that in the previous case. The origin of the quadrupole-like charge separation can be understood by the Larmor motions of charged particles due to the strong localized magnetic fields, whose Larmor radius is order of the cloud transverse scale.

Figures 4-4(a) and 4-4(b) for the electron-ion plasmas show the spatial distributions of the generated magnetic field at $\omega_{pe}t = 15$ for transverse width 10Δ with a number density of 100 particles per cell and transverse width 20Δ with a number density of 200 particles per cell. The structure of generated magnetic fields is in contrast with the case of pair plasmas. As seen in Fig. 4-4(a), a quadrupole-like structure occur in the magnetic field. Figure 4-4(c) shows the spatial distributions

of the charge density $(\rho_+ - \rho_-)$ for transverse width 10Δ with a number density of 100 particles per cell. The charge density distribution is also different from the case of the pair plasmas. Figure 4-4(b) and 4-4(d) show the spatial distributions of the magnetic field and the charge density for transverse width 20Δ with a number density of 200 particles per cell, respectively. The structure of the charge density becomes more complicated than the case of the pair plasmas.

We note here that the conversion rate from the stream kinetic energy to the magnetic field energy for the pair plasmas is more effective than the case of the electron-ion plasma. This is due to the fact that the electric field along the stream direction becomes stronger than the case of the pair plasmas; then,the stream kinetic energy of the electron-ion plasma can be converted to the plasma heating rather than to the magnetic energy. Figure 4-6,4-7 show the electron velocity distribution function in the whole system at initial and final time step. As seen in figures, the heating of the electron-ion plasma is more larger than that of pair plasma. The energy of only ion can be converted to electron and magnetic field energy in the case of electron-ion plasma. On the other hand, both electron and positron can be converted to field energy in the case of pair plasma.

4.3.2 Magnetic Field Generation during Coalescence of Magnetic Islands in Pair Plasmas

In this section we present one example of quasi-static magnetic field generation associated with charge separation in pair plasmas. It is well known that a current sheet in plasmas is unstable against the tearing instability, and in its nonlinear stage, there appears coalescence of magnetic islands, which tends to form a large magnetic island. Recently, Haruki et al. (1998)[25] investigated the dynamics of coalescence of magnetic islands in pair plasmas and found that there wave emissions of high frequency electromagnetic waves and Alfvén waves occur during coalescence of magnetic islands. They concluded that the origin of the wave emissions is due to the generation of a localized strong magnetic flux associated with quadrupole-like charge separation during coalescence of magnetic islands.

Figure 4-5(a),4-5(c) show the time development of the electron distribution in the current sheet, in which only a fraction of 1/500 of total electrons is plotted. As seen in Fig. 4-5(a), there are three clumps of electrons, corresponding to three magnetic islands. As time passes, the three islands merge into one, as seen in Fig.4-5(c). Figure 4-5(d) shows the vector plots of the magnetic field, which corresponds to Fig. 4-5(c). During coalescence of two magnetic islands from the time period of Fig. 4-5(b) to Fig. 4-5(c), a collision of two plasma blobs (or clouds) occurs, just as discussed in the previous section. Therefore,a strong localized magnetic flux appears,as shown in Fig. 4-5(e), and at the same time a quadrupole-like charge separation occurs as shown in Fig. 4-5(f). In this simulation, the width of the current sheet is on the order of the electron skin depth. When the width of the current sheet becomes larger than the electron skin depth, more pairs of magnetic fluxes associated with more complicated charge density appear,as discussed in the previous section. Strong wave emissions occur during the decay phase of the magnetic flux as well as

during the charge separation. The same phenomena discussed here can occur during coalescence of magnetic islands in a current sheet of electron-ion plasmas.

4.4 Summary

We investigated the dynamics of the collision of narrow plasma clouds, whose transverse dimension is on the order of the electron skin depth. By using a 2D3V PIC code,we showed that during the collision of narrow plasma clouds, generation of a quasi-static magnetic flux occurs in both pair plasmas and electron-ion plasmas. It is also shown that the localized strong magnetic fluxes result in the generation of a charge separation with complicated structures, depending on the width of the transverse scale of the clouds. We presented an application of this process, which occurs during coalescence of magnetic islands in a current sheet of pair plasmas. We emphasize that the generation of strong localized magnetic fluxes associated with the charge separation causes strong emissions of high- and low-frequency electromagnetic waves in plasmas.

Figure Captions

Figure4-1. The spatial distribution of electrons in the x-y plane at (a) $\omega_{pe}t = 0$ and (b) $\omega_{pe}t = 15$. (c) time history of the magnetic field energy $\int\int dxdyB_z(x,y)^2/2\mu_0$ in the system for pair plasmas. The counter-streaming velocity of two clouds with transverse width 10Δ is $v_o = 0.5c$.

Figure4-2. The spatial distribution of electrons in the x-y plane at (a) $\omega_{pe}t = 0$ and (b) $\omega_{pe}t = 15$. (c) time history of the magnetic field energy ${B_z}^2$ in the system for electron-ion plasmas. The counter-streaming velocity of two clouds with transverse width 10Δ is $v_o = 0.5c$.

Figure 4-3. The spatial distribution of generated magnetic field B_z at $\omega_{pe}t = 15$ for pair plasmas: (a) for transverse width 10Δ with a number density of 100 particles per cell and (b) transverse width 20Δ with a number density of 200 particles per cell, respectively. (c) and (d) show the spatial distributions of the charge density $(\rho_+ - \rho_-)$ for transverse width 10Δ with a number density of 100 particles per cell and transverse width 20Δ with a number density of 200 particles per cell, respectively.

Figure 4-4. The spatial distribution of generated magnetic field B_z at $\omega_{pe}t = 15$ for electron-ion plasmas: (a) for transverse width 10Δ with a number density of 100 particles per cell and (b) transverse width 20Δ with a number density of 200 particles per cell, respectively. (c) and (d) show the spatial distributions of the charge density $(\rho_+ - \rho_-)$ for transverse width 10Δ with a number density of 100 particles per cell and transverse width 20Δ with a number density of 200 particles per cell, respectively.

Figure 4-5. Coalescence dynamics of magnetic islands in pair plasmas. The time development of the spatial electron distributions in a current sheet: (a) $\omega_{pe}t = 21.08$, (b) $\omega_{pe}t = 26.35$, (c) $\omega_{pe}t = 31.62$. (d) Vector plots of magnetic fields B_x and B_y at $\omega_{pe}t = 31.62$. (e) The spatial distribution of generated magnetic flux B_z at $\omega_{pe}t = 31.62$. (f) The spatial distribution of the charge density at $\omega_{pe}t = 31.62$.

Figure 4-6. The velocity distributions of electron particles in each direction at $\omega_{pe}t = 0$ (dashed line) ,$\omega_{pe}t = 52.7$ (full line).(electron-positron plasma) V_{th}:electron thermal velocity

Figure 4-7. The velocity distributions of electron particles in each direction at $\omega_{pe}t = 0$ (dashed line) ,$\omega_{pe}t = 52.7$ (full line).(electron-ion plasma)

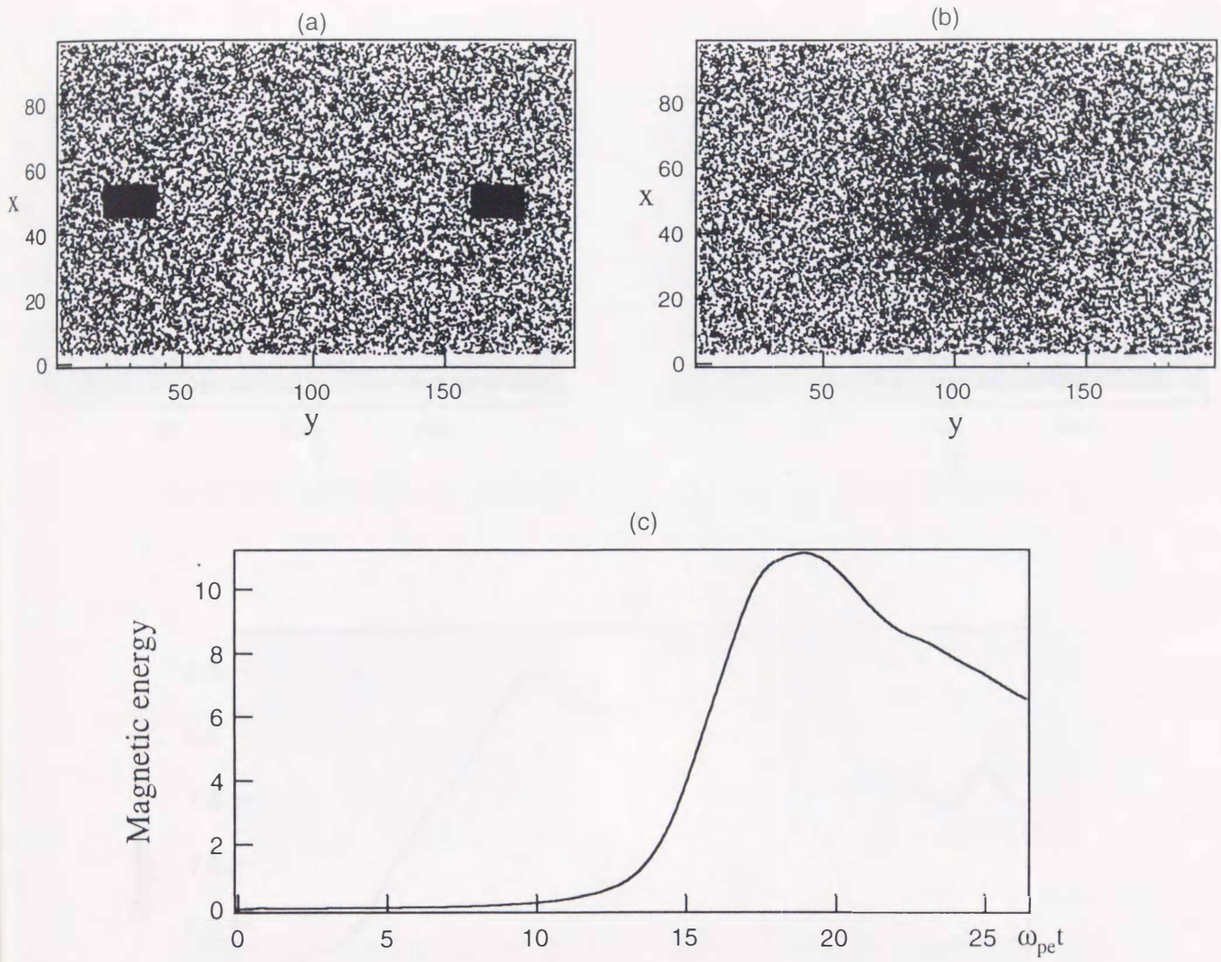
(a)
(b)
(c)
x
y
80
60
40
20
0
50
100
150
Magnetic energy
10
8
6
4
2
0
5
15
20
25
$\omega_{pe}t$

Figure 4-1

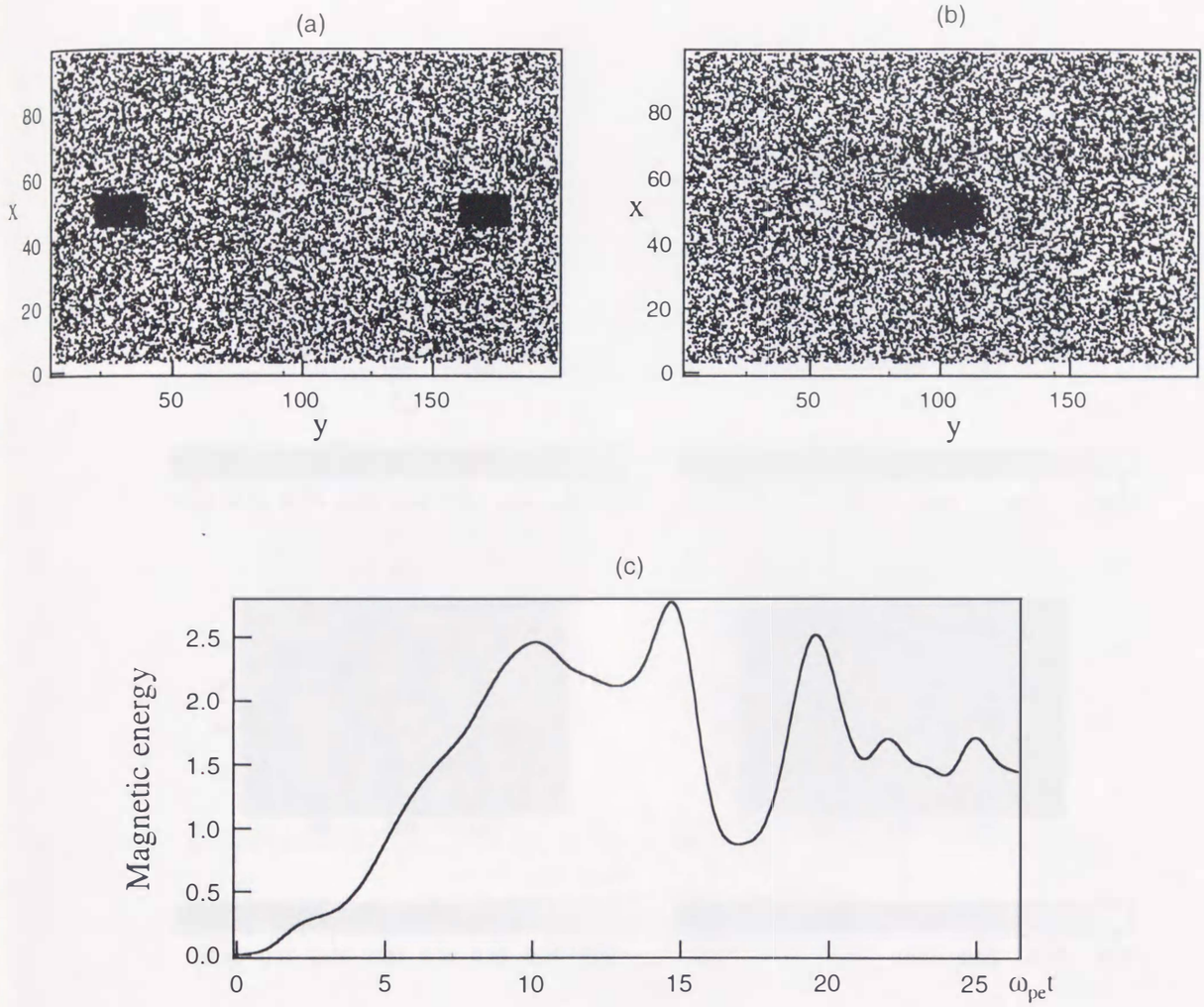
(a)
(b)
(c)
80
60
40
20
0
X
x
50
100
150
y
Magnetic energy
2.5
2.0
1.5
1.0
0.5
0.0
0
5
10
15
20
25
$\omega_{pe}t$

Figure 4-2

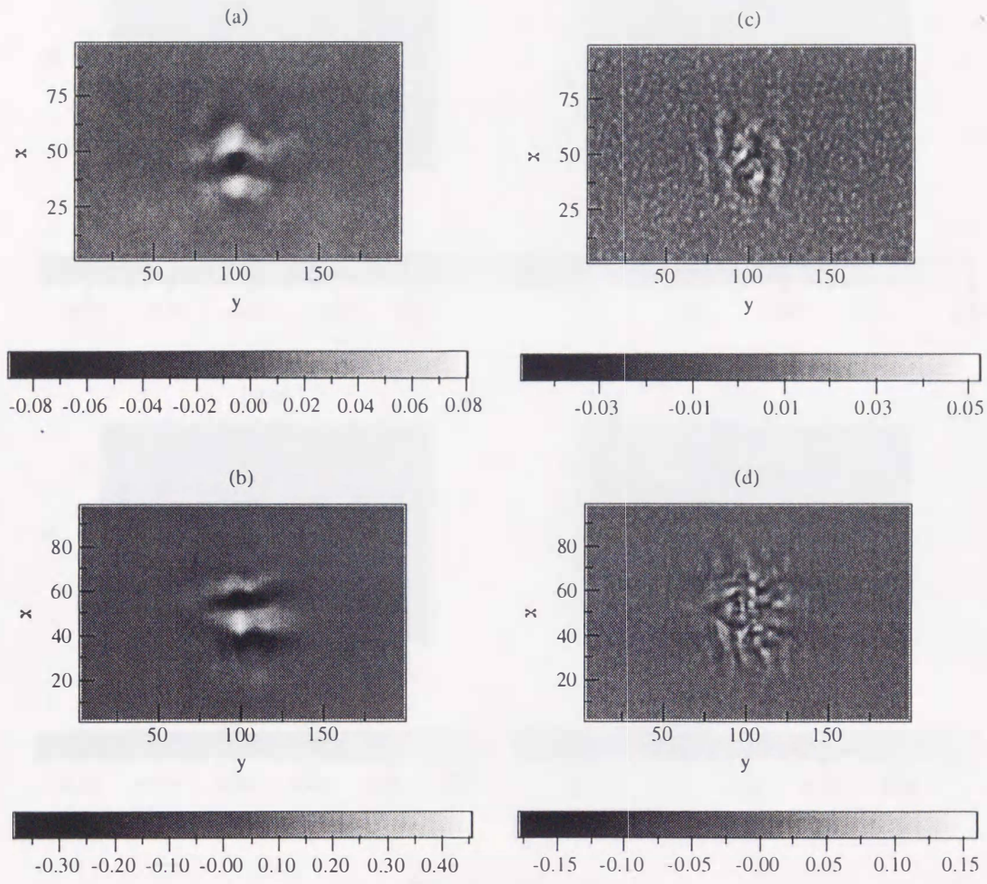
(a)
75
50
25
x
50
100
150
y
-0.08 -0.06 -0.04 -0.02 0.00 0.02 0.04 0.06 0.08
(c)
75
50
25
x
50
100
150
y
-0.03 -0.01 0.01 0.03 0.05
(b)
80
60
40
20
x
50
100
150
y
-0.30 -0.20 -0.10 -0.00 0.10 0.20 0.30 0.40
(d)
80
60
40
20
x
50
100
150
y
-0.15 -0.10 -0.05 -0.00 0.05 0.10 0.15

Figure 4-3

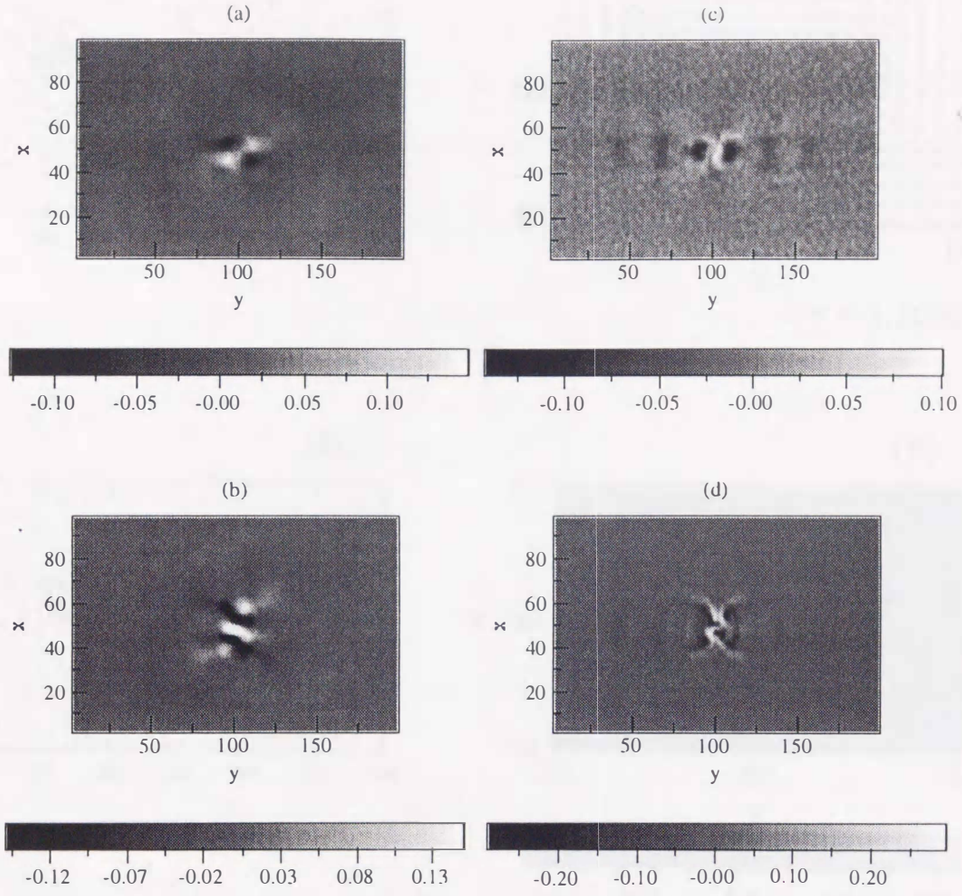
(a)
(c)
(b)
(d)
x
y
80
60
40
20
50
100
150
-0.10
-0.05
-0.00
0.05
0.10
-0.12
-0.07
-0.02
0.03
0.08
0.13
-0.20
-0.10
-0.00
0.10
0.20

Figure 4-4

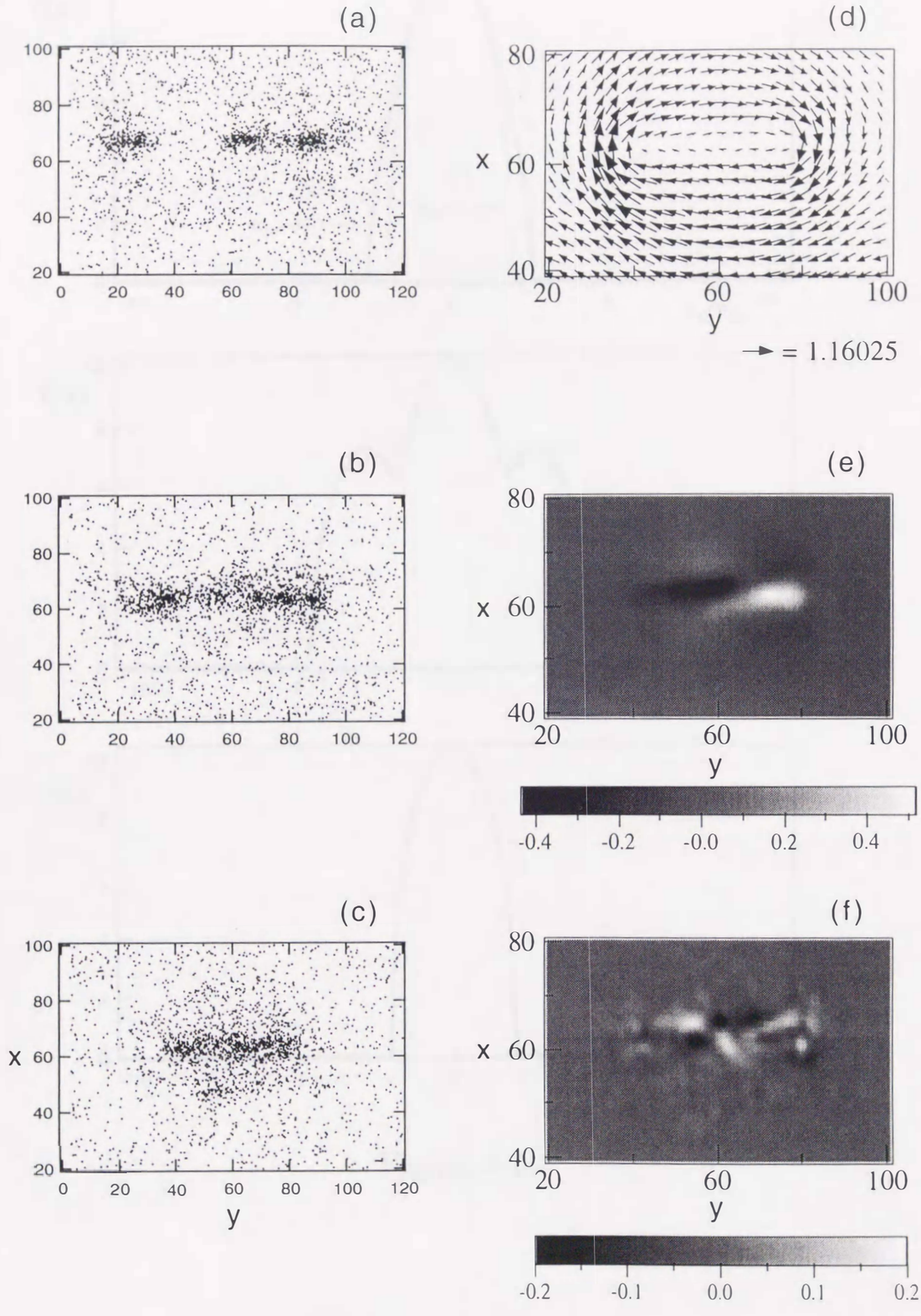

Figure 4-5

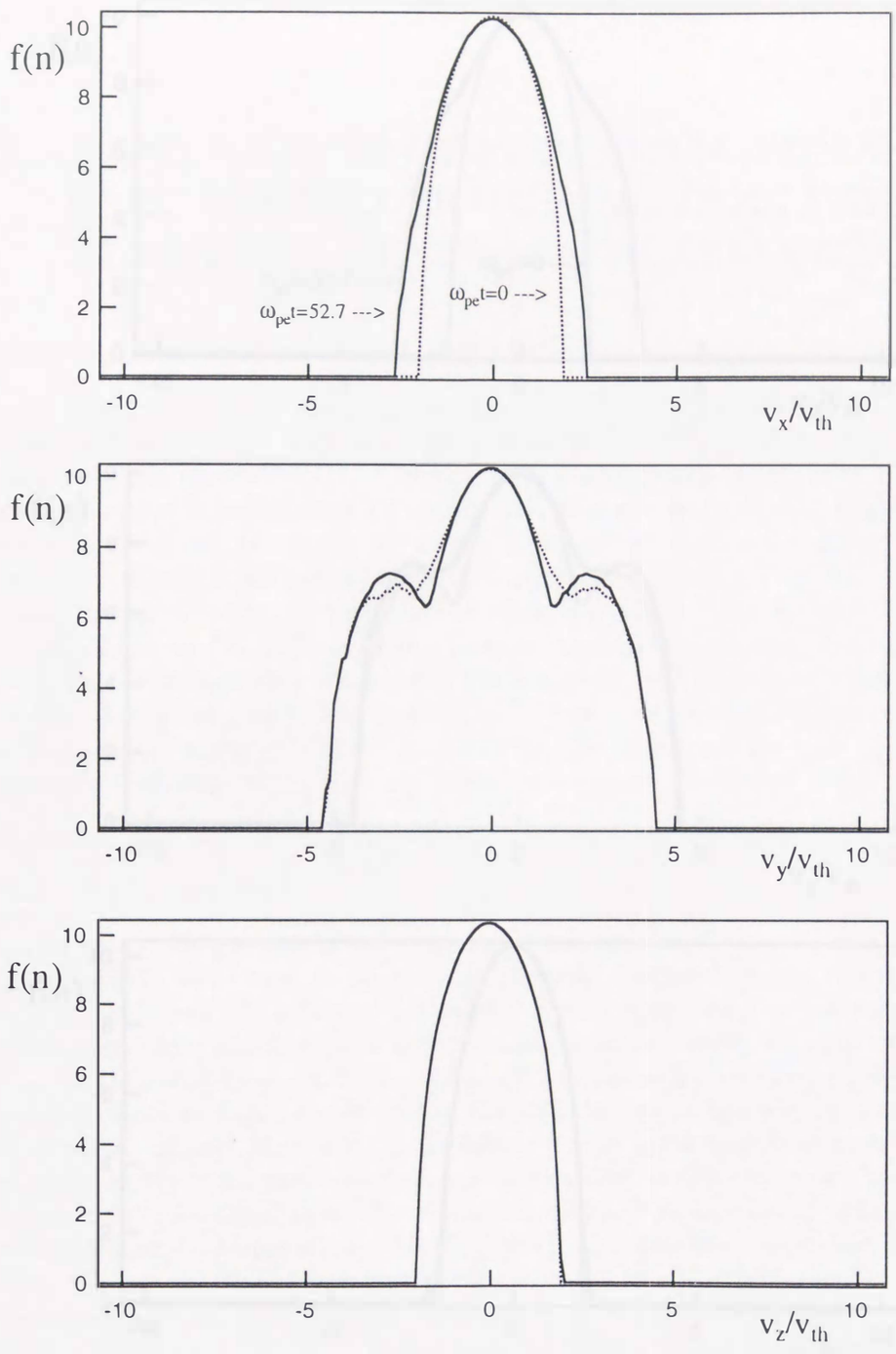
f(n)
10
8
6
4
2
0
-10
-5
0
5
10
v_x/v_{th}
$\omega_{pe}t$=52.7 --->
$\omega_{pe}t$=0 --->
f(n)
v_y/v_{th}
f(n)
v_z/v_{th}

Figure 4-6

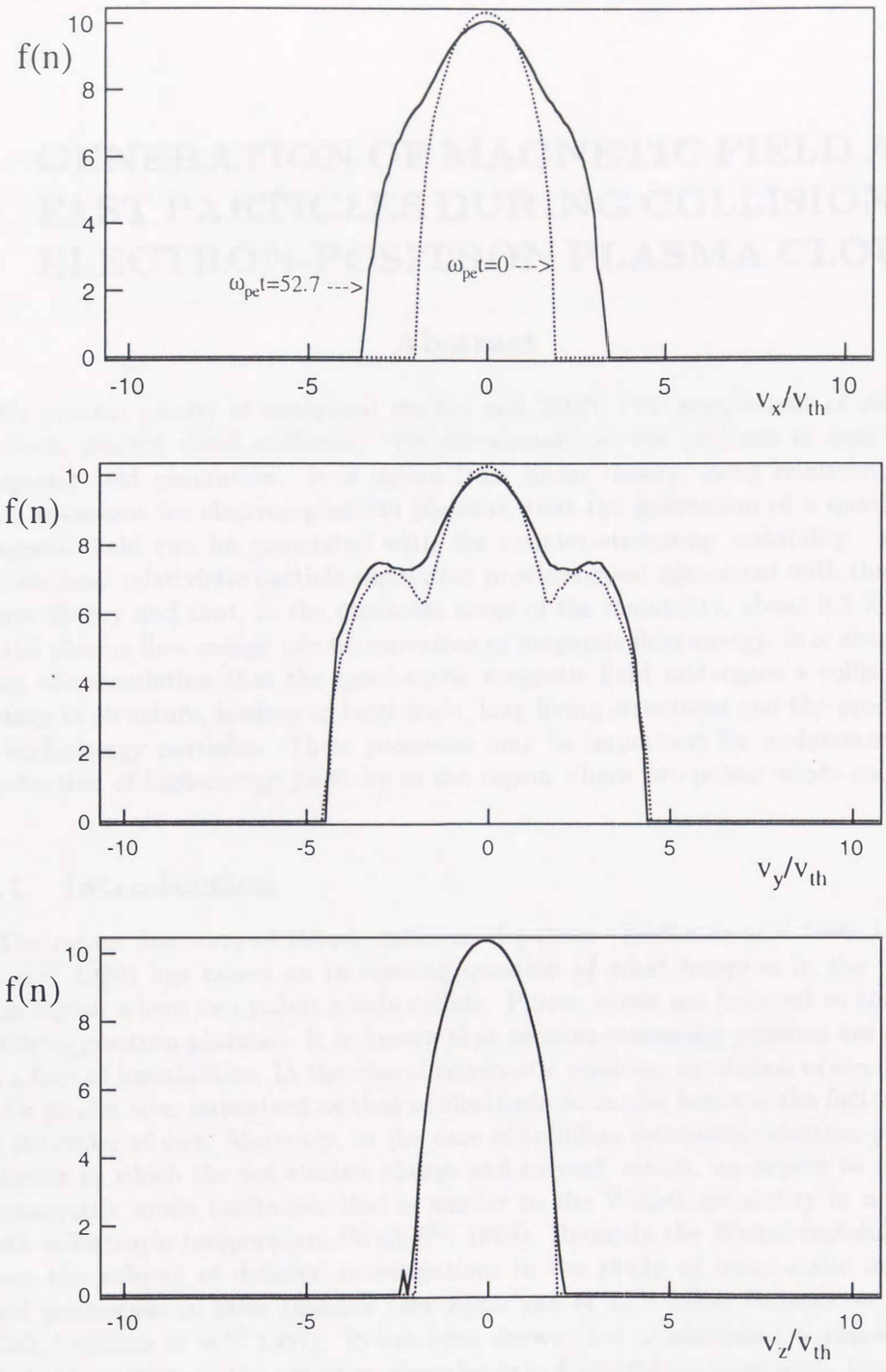
f(n)
10
8
6
4
2
0
-10
-5
0
5
10
v_x/v_{th}
$\omega_{pe}t=52.7$ --->
$\omega_{pe}t=0$ --->
f(n)
v_y/v_{th}
f(n)
v_z/v_{th}

Figure 4-7

5 GENERATION OF MAGNETIC FIELD AND FAST PARTICLES DURING COLLISION OF ELECTRON-POSITRON PLASMA CLOUDS

Abstract

We present results of analytical studies and 2D3V PIC simulations of electron-positron plasma cloud collisions. We concentrate on the problem of quasi-static magnetic field generation. It is shown from linear theory, using relativistic two-fluid equations for electron-positron plasmas, that the generation of a quasi-static magnetic field can be associated with the counter-streaming instability. A two-dimensional relativistic particle simulation provides good agreement with the above linear theory and that, in the nonlinear stage of the instability, about 5.3 % of the initial plasma flow energy can be converted to magnetic field energy. It is also shown from the simulation that the quasi-static magnetic field undergoes a collision-less change of structure, leading to large scale, long living structures and the production of high-energy particles. These processes may be important for understanding of production of high-energy particles in the region where two pulsar winds collide.

5.1 Introduction

The recent discovery of binary millisecond pulsars (Becker et al.[1] 1996, Lorimer et al.[2] 1996) has raised an interesting question of what happens in the interaction region where two pulsar winds collide. Pulsar winds are believed to consist of electron-positron plasmas. It is known that counter-streaming plasmas are subject to a host of instabilities. In the case of relativistic plasmas, excitation of electromagnetic modes is as important as that of electrostatic modes because the factor v/c is of the order of one. Moreover, in the case of colliding relativistic electron-positron streams in which the net electric charge and current vanish, we expect to see electromagnetic mode excitation that is similar to the Weibel instability in a plasma with anisotropic temperature (Weibel[3], 1959). Recently the Weibel instability has been the subject of detailed investigations in the study of quasi-static magnetic field generation in laser plasmas (see Askar'yan et al.[4] 1994, Bulanov et al.[17,18] 1996, Califano et al.[6] 1997). It has been shown that in electron-ion plasmas, the Weibel instability in the nonlinear stage leads to formation of large scale, long-living electron vortices associated with the magnetic fields.

In this paper we investigate physical processes during the collision of counter-streaming electron-positron plasmas using a relativistic two-fluid model and a relativistic particle simulation. In Section 5.2 we present a linear theory derived from the relativistic two-fluid model, and show the excitation of strong electromagnetic perturbations associated with quasi-static magnetic fields. In Section 5.3 we show results from a two-dimensional relativistic particle simulation. In the linear regime there is a good agreement between linear theory and simulations. In the nonlinear

stage, the magnetic field can undergo collision-less change of structure, and a large scale structure of the magnetic field is produced. In the final section we summarize our results.

5.2 Linear Theory of Electromagnetic Instability

The dynamics of counter-streaming cold electron-positron plasmas with velocities $\mathbf{v}_{ia}$, where $i = p(positron)$ and $i = e(electron)$ and $a = 1, 2$ are the two counter-streaming components of particles, is described by the equations:

$$\frac{\partial \mathbf{P}_{ea}}{\partial t} = -\mathbf{v}_{ea} \cdot \nabla \mathbf{P}_{ea} - (\mathbf{E} + \mathbf{v}_{ea} \times \mathbf{B}), \tag{25}$$

$$\frac{\partial \mathbf{P}_{pa}}{\partial t} = -\mathbf{v}_{pa} \cdot \nabla \mathbf{P}_{pa} + (\mathbf{E} + \mathbf{v}_{pa} \times \mathbf{B}), \tag{26}$$

$$\frac{\partial (n_{pa} - n_{ea})}{\partial t} + \nabla \cdot (n_{pa}\mathbf{v}_{pa} - n_{ea}\mathbf{v}_{ea}) = 0, \tag{27}$$

$$\frac{\partial \mathbf{B}}{\partial t} = -\nabla \times \mathbf{E}, \tag{28}$$

$$\frac{\partial \mathbf{E}}{\partial t} = \nabla \times \mathbf{B} - \sum_a (\mathbf{J}_{pa} + \mathbf{J}_{ea}), \tag{29}$$

$$\nabla \cdot \mathbf{E} = \sum_a (n_{pa} - n_{ea}), \tag{30}$$

where $\mathbf{v}_{ea} = \mathbf{P}_{ea}(1 + \mathbf{P}_{ea}{}^2)^{-\frac{1}{2}}$, $\mathbf{v}_{pa} = \mathbf{P}_{pa}(1 + \mathbf{P}_{pa}{}^2)^{-\frac{1}{2}}$, $\mathbf{J}_{ea} = -n_{ea}\mathbf{v}_{ea}$, $\mathbf{J}_{pa} = n_{pa}\mathbf{v}_{pa}$. The densities and the velocities are normalized by a characteristic density n, the speed of light c and the time is normalized by the plasma frequency $\omega_{pe} = (4\pi n e^2/m)^{\frac{1}{2}}$. We consider a case in which the counter-streaming plasmas have equal velocity in the y-direction and density such as $v_{0,e1} = v_{0,p1}$, $n_{0,e1} = n_{0,p1}$, $v_{0,e2} = v_{0,p2}$, $n_{0,e2} = n_{0,p2}$. Linearizing the above set of equations and assuming a dependence of the form $F(x, y, t) = f \exp(i(k_x x + k_y y - \omega t))$, we obtain the following dispersion equation:

$$(1 - \Omega_{2p}^{-2} - \Omega_{2e}^{-2})\{(1 + \Omega_{4p}^{-2} + \Omega_{4e}^{-2})k_y^2 - \omega^2(1 - \Omega_{1p}^{-2} - \Omega_{1e}^{-2}) - 2\omega k_y(\Omega_{3p}^{-2} + \Omega_{3e}^{-2})\}$$

$$+k_x^2\{(1 + \Omega_{4p}^{-2} + \Omega_{4e}^{-2})(1 - \Omega_{1p}^{-2} - \Omega_{1e}^{-2}) + (\Omega_{3p}^{-2} + \Omega_{3e}^{-2})^2\} = 0, \tag{31}$$

where

$$\Omega_{1e}^{-2} = \sum_a \frac{n_{0,ea}}{\Gamma_{ea}\Omega_{ea}^2}, \quad \Omega_{2e}^{-2} = \sum_a \frac{n_{0,ea}}{\Gamma_{ea}^3\Omega_{ea}^2},$$

$$\Omega_{3e}^{-2} = \sum_a \frac{n_{0,ea}v_{0,ea}}{\Gamma_{ea}\Omega_{ea}^2}, \quad \Omega_{4e}^{-2} = \sum_a \frac{n_{0,ae}v_{0,ae}^2}{\Gamma_{ae}\Omega_{ae}^2},$$

$$\Omega_{1p}^{-2} = \sum_a \frac{n_{0,pa}}{\Gamma_{pa}\Omega_{pa}^2}, \quad \Omega_{2p}^{-2} = \sum_a \frac{n_{0,pa}}{\Gamma_{pa}^3\Omega_{pa}^2},$$

$$\Omega_{3p}^{-2} = \sum_a \frac{n_{0,pa}v_{0,pa}}{\Gamma_{pa}\Omega_{pa}^2}, \quad \Omega_{4p}^{-2} = \sum_a \frac{n_{0,pa}v_{0,pa}^2}{\Gamma_{pa}\Omega_{pa}^2},$$

$$a = 1, 2,$$

where the following notations are used: $\Omega_{pa} = \omega - k_y v_{0,pa}, \Gamma_{pa} = (1 - v_{0,pa}^2)^{-1/2}, \Omega_{ea} = \omega - k_y v_{0,ea}, \Gamma_{ea} = (1 - v_{0,ea}^2)^{-1/2}$.

We note here that the above dispersion relation is an extension of the case derived by Califano et al.[6](1997), who investigated the development of the Weibel instability in the study of interaction between high-intensity laser pulses and plasmas.

We consider collision of two symmetric plasma flows with velocities, $v_0 = 0.56c$ and $-0.56c$, and with equal density. Figure 5-1 shows the growth rate normalized by ω_{pe} versus the wave-number k_x normalized by c/ω_{pe} for the propagation angle of 27.5 degree from the y-direction. As seen in this figure, there appear three different branches, (a), (b) and (c). The branch (a) can exist for one-component counter-streams (electrons or positrons), while the other branches (b) and (c) disappear for one-component streams. Branch (a) is similar to the Weibel instability in laser plasmas (Califano et al.[6]1997). On the other hand, branches (b) and (c) are caused by the instability driven by the coupling of two component counter-streams, and these two branches merge into one mode when $k_x \gg k_y$.

5.3 Simulation Model

The code used here is a $2D3V$, fully relativistic electromagnetic particle-in-cell code, modified from the $3D3V$ TRISTAN code[16] (Buneman,1993). The system size is $L_x = 65\Delta$ and $L_y = 1024\Delta$, where $\Delta(= 1)$ is the grid size. Periodic boundary conditions are imposed on particles and fields. There are 1,310,720 electron- positron pairs filling the entire domain uniformly and keeping the domain charge neutral. Hence the average particle number density is about 20 per cell. The initial state is such that in the region of $y = (1 \sim 512)\Delta$, the plasma drift velocity is $v_d = 0.56c$ (c is the light speed, which is taken as 0.5), with shifted Maxwellian distribution with the thermal velocity $v_{th} = 0.09366c$, and in the region, $y = (512 \sim 1024)\Delta$, $v_d = -0.56c$. This corresponds to a Lorentz factor $\gamma = (1 - (v_d/c)^2)^{-1/2} = 1.2$. Other parameters are as follows; the mass ratio $m_p/m_e = 1$, $\omega_{pe}\Delta t = 0.052$, the electron collisionless skin depth $d_e = c/\omega_{pe} = 9.6\Delta$. Thus the computation box has a size equal $\approx 6.6d_e$ in the $x-$direction and $\approx 106.6d_e$ in the $y-$direction. The initial electric and magnetic field, which is normalized by c is zero.

5.4 Simulation Results

We investigated several cases of electron-positron plasma cloud collisions. The most important result is the generation of the magnetic field in the direction perpendicular to the counter-stream direction from the initial state with no-magnetic field.

Figure 5-2 shows the time development of the magnetic field (B_z) structures in the x-y plane. As seen in Fig.5-2(a), initially (for $\omega_{pe}t = 10$) there appears very coherent structures with positive and negative magnetic polarities. This corresponds to the filamentation of the plasma with creation of the current sheet system with the current sheets situated where the magnetic field changes sign. The characteristic scale of the current sheet is about $0.6d_e$ in the transverse direction along the

$x-$axis and about $2\pi d_e$ in the longitudinal direction along the $y-$axis, which is also consistent with the branch (c) of the linear theory shown in Fig.5-1.

As time goes on, the front of both streams propagates further and behind the front the bending and coalescence of the filaments occur as it is seen in Fig.5-2(b) where the magnetic field pattern is shown for $\omega_{pe}t = 31$. This process makes the characteristic scale length of the magnetic field larger. The coalescence process of filaments first becomes apparent after about $\omega_{pe}t = 31$. Asymptotically, at $\omega_{pe}t = 52.7$, in Fig.5-2(c), we see formation of large scale, long lived magnetic structures with the size of the order of $2\pi c/\omega_{pe}$. The alternating polarity corresponds to electric current distributions in the x, y-plane of the form of antisymmetric vortex flow.

Figure 5-3 shows the time history of electric ($E_x{}^2$, $E_y{}^2$) and magnetic ($B_z{}^2$) field energy normalized by $2VtL_x/L_xL_y$,where V is the plasma front velocity of the streams, assumed to be constant. Thus they give the dependencies of the average values of the fields v.s. time. As seen in Figs. 5-3(a) and 5-3(b), almost the same amount of electrostatic wave energy is excited in the x- and y-directions. From a Fourier analysis of the wave patterns in E_x and E_y, we find that the electrostatic energy is associated with the Langmuir waves. The propagation direction in which the waves are excited is oblique and at an angle of about 45 degree from the x-direction.

As seen in Fig.5-3(c), a strong magnetic B_z component can be excited with almost the same growth rate as the Langmuir waves. The maximum magnetic energy is about twice the electric field energy. This is consistent with the Weibel mode development. The electric field amplitude can be estimated from equation (4) as $E \approx (\omega/kc)B$. If we take ω to be of the order $\omega \approx \gamma \approx (v_0/c)\omega_{pe}$, we obtain for $v_0/c \approx 0.5$ a magnetic energy which is about twice the electric field energy. The growth rate observed from Fig.5-3(c) agrees with the branch (c) obtained from the linear theory given in the previous section, and is about $\gamma = (v_0/c)\omega_{pe}$. The magnitude of the growth rate calculated from the dispersion relation is about 0.69 with $k_x = 1.68$ and $k_y = 3.82$ while the value of growth rate calculated from the time history of magnetic field energy is about 0.67. By using the final value of the magnetic energy, we can estimate the energy conversion rate from the initial kinetic flow energy. We find that the energy conversion rate is about 5.3%. If we study the time evolution of high-energy particle distribution, then it appears particles with significant energy after $30\omega_{pe}t$. Therefore we may conclude that the particles can be accelerated due to collision-less change of the structure of the magnetic fields associated with the induction electric field. The collision-less change of the structure of the magnetic fields occurs via annihilation of magnetic fields with opposite polarity. This induces the electric field in the x, y-plane, which in turn accelerates charged particles. We have seen no acceleration of the electrons and positrons along the z-direction in accordance with this process. In Fig. 5-4 we show the electron (a) and positron (b) energy spectrum in the final stage; (c) is the initial energy distribution of both particles.

In the question whether the magnetic field remains in a plasma when the clouds had passed, we did another simulation, where we have two regions; in one region ($0 < y < 928$) plasma is in rest, while in the other region ($928 < y < 1024$) the

colliding cloud with the initial velocity $v = 0.6c$ is imposed. The colliding cloud size is $L_x = L_y = 96$. Figure 5-5 shows the time development of magnetic field (B_z) in the $x - y$ plane. At $\omega_{pe}t = 100$ (Fig.5-5 (d)), the cloud front approaches nearly at $y = 300$, passing through the region of $400 < y < 800$. From this figure we find that a quasi-static magnetic field could remain in the region where the cloud passed. The generated magnetic field tends to become large scale with maximum intensity of about 25% of the initially generated magnetic field.(see Fig.5-5 (a) and (d))

5.5 Summary

It is shown from linear theory using relativistic two-fluid equations for electron-positron plasmas, that the generation of a quasi-static magnetic field is associated with the counter-streaming instability of electron-positron plasmas. A two-dimensional relativistic particle simulation is in good agreement with the above linear theory and furthermore, in the nonlinear stage of the instability, shows that about.5.3 % of the initial plasma flow energy can be converted to magnetic field energy. It is also shown from the simulation that the generated quasi-magnetic field undergoes a change in structure through coalescence of magnetic filaments, leading to large scale structures and the production of high-energy particles. These processes may be important for understanding of the production of high-energy particles in the region of two colliding pulsar winds.

Figure Captions

Figure 5-1. Linear growth rate normalized by ω_{pe} vs. the wave-number k_x normalized by c/ω_{pe} for the propagation angle of 27.5 degree, with respect to the y-direction. The parameter used is $v_d = 0.56c$. Branch (a) is similar to the Weibel instability, while branches (b) and (c) are caused by the instability driven by the coupling of two component counter-streams.

Figure 5-2. Time development of the magnetic field (B_z) structures in the x-y plane.
(a) $\omega_{pe}t = 10$, (b) $\omega_{pe}t = 31$, (c) $\omega_{pe}t = 52.7$.

Figure 5-3. Time history of electric field energy; (a) ${E_x}^2$, (b) ${E_y}^2$ and magnetic field energy; (c) ${B_z}^2$, normalized by $2VtL_x/L_xL_y$, where V is the plasma front velocity of the streams, assumed constant.

Figure 5-4. The electron(a) and positron(b) energy spectrum in the final state of the simulation. E normalized by the thermal energy is total kinetic energy of particles. (c) shows the initial energy distribution of both particle species.

Figure 5-5. The time development of magnetic field (B_z) in the $x - y$ plane.

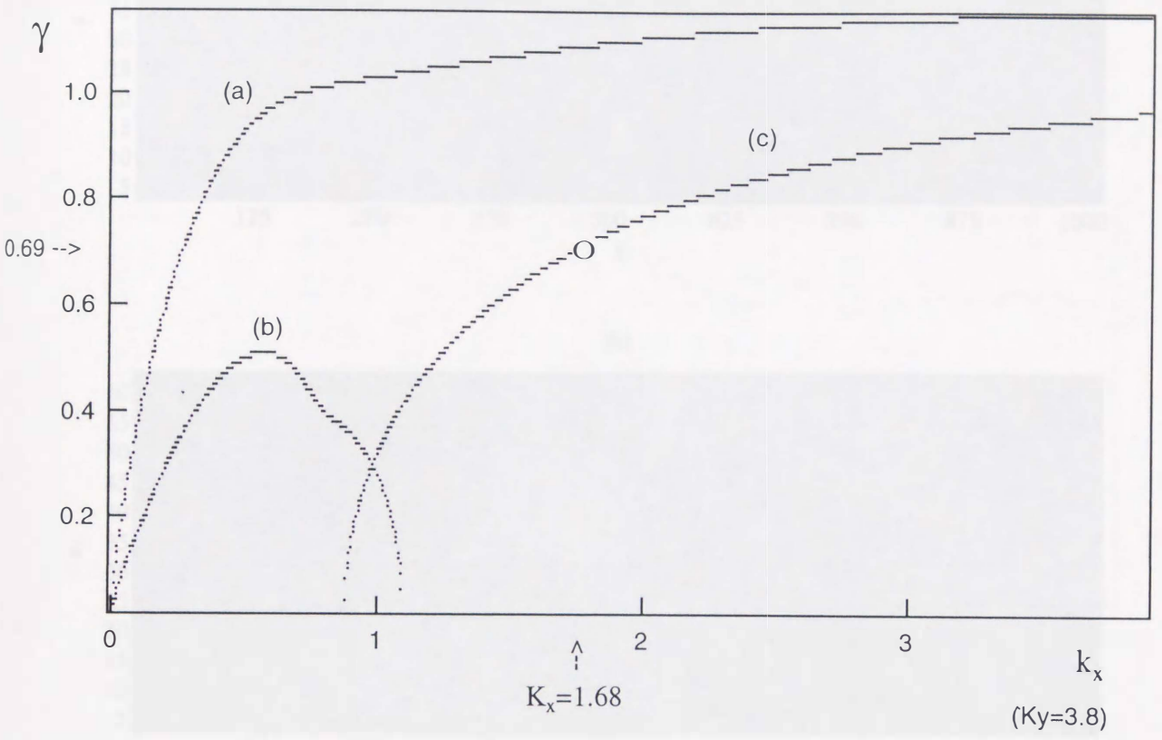

Figure 5-1

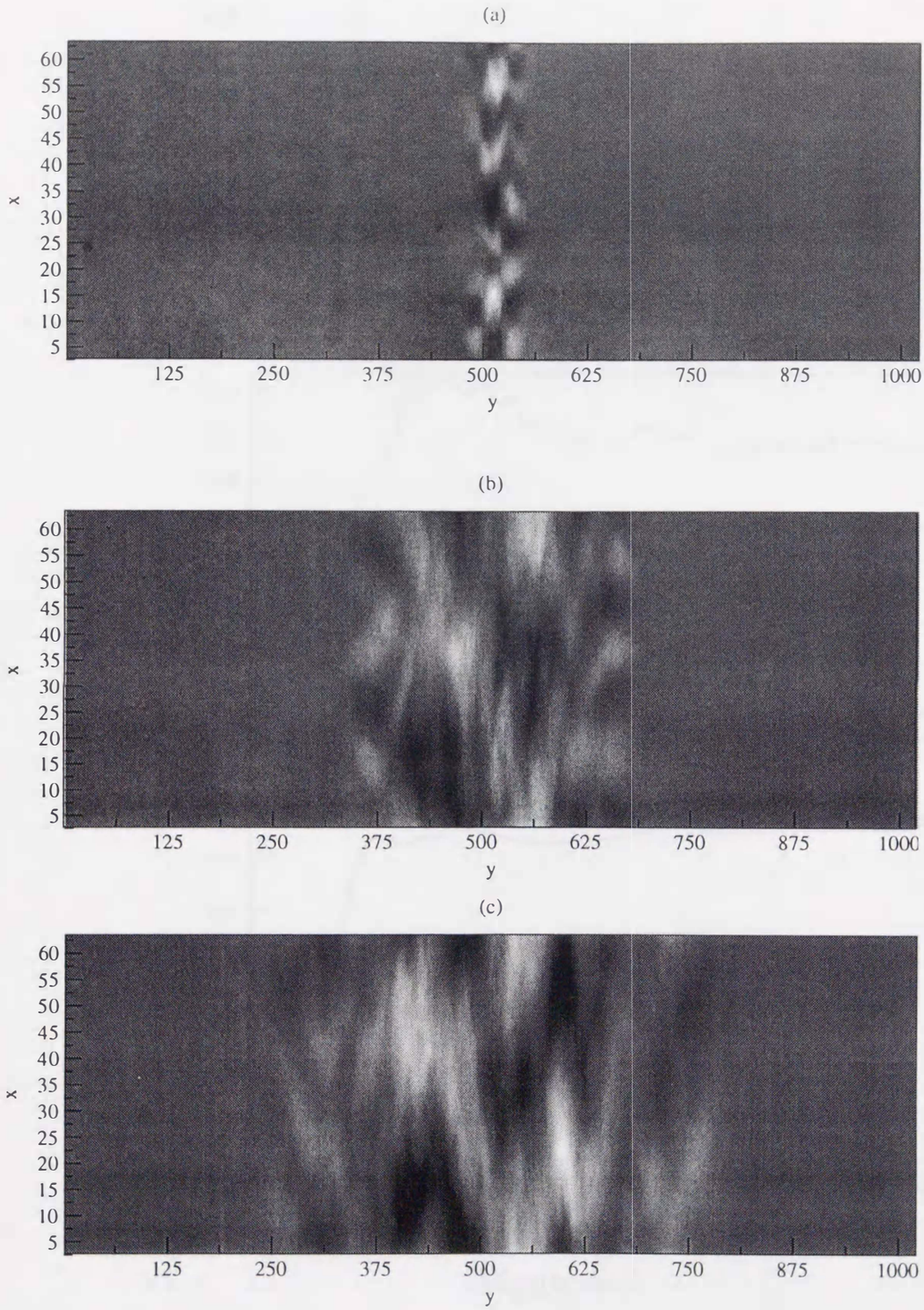
(a)
60
55
50
45
40
35
30
25
20
15
10
5
x
125
250
375
500
625
750
875
1000
y
(b)
60
55
50
45
40
35
30
25
20
15
10
5
x
125
250
375
500
625
750
875
1000
y
(c)
60
55
50
45
40
35
30
25
20
15
10
5
x
125
250
375
500
625
750
875
1000
y
-0.38
-0.25
-0.12
0.00
0.12
0.25
0.38

Figure 5-2

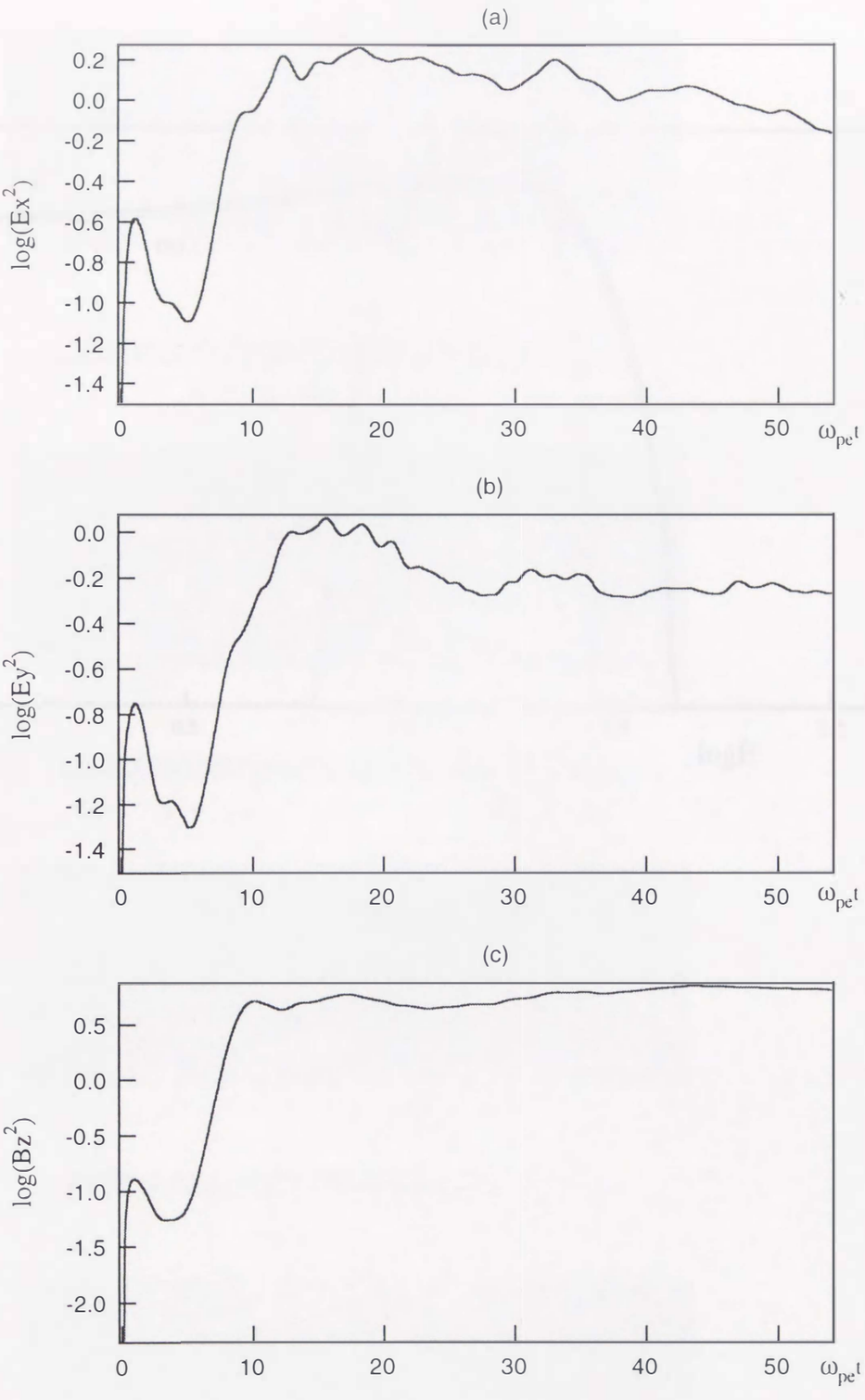
(a)
log(Ex^2)
0.2
0.0
-0.2
-0.4
-0.6
-0.8
-1.0
-1.2
-1.4
0
10
20
30
40
50
$\omega_{pe}t$
(b)
log(Ey^2)
0.0
-0.2
-0.4
-0.6
-0.8
-1.0
-1.2
-1.4
0
10
20
30
40
50
$\omega_{pe}t$
(c)
log(Bz^2)
0.5
0.0
-0.5
-1.0
-1.5
-2.0
0
10
20
30
40
50
$\omega_{pe}t$

Figure 5-3

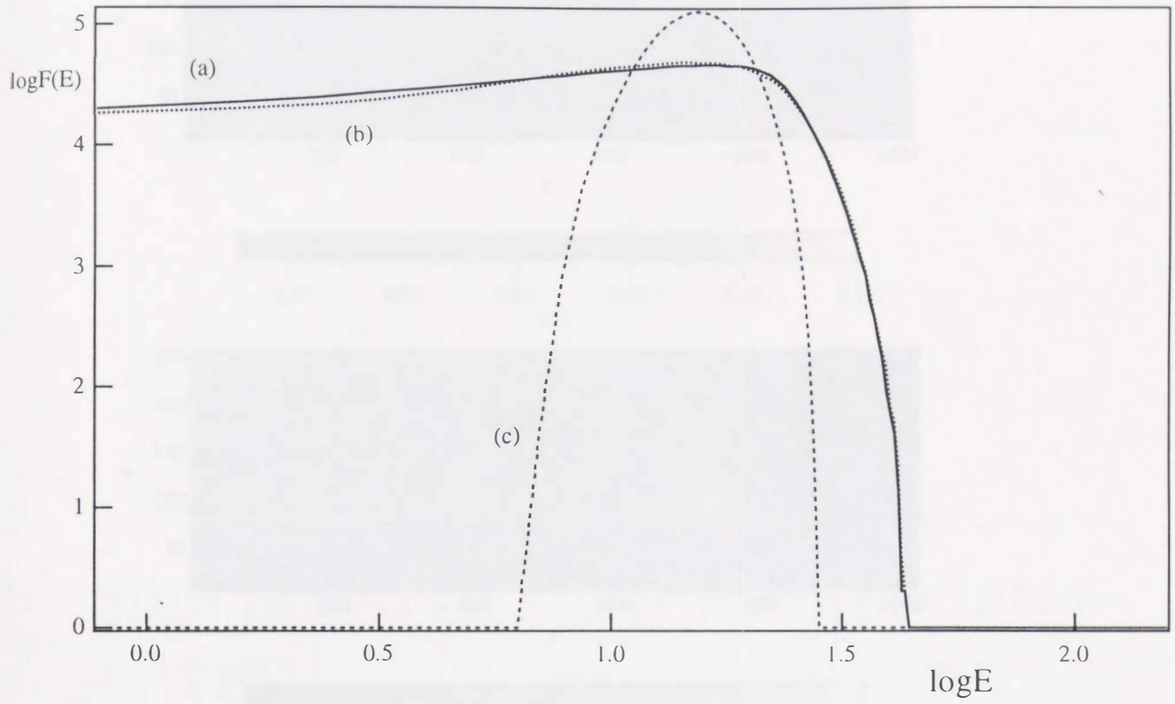

Figure 5-4

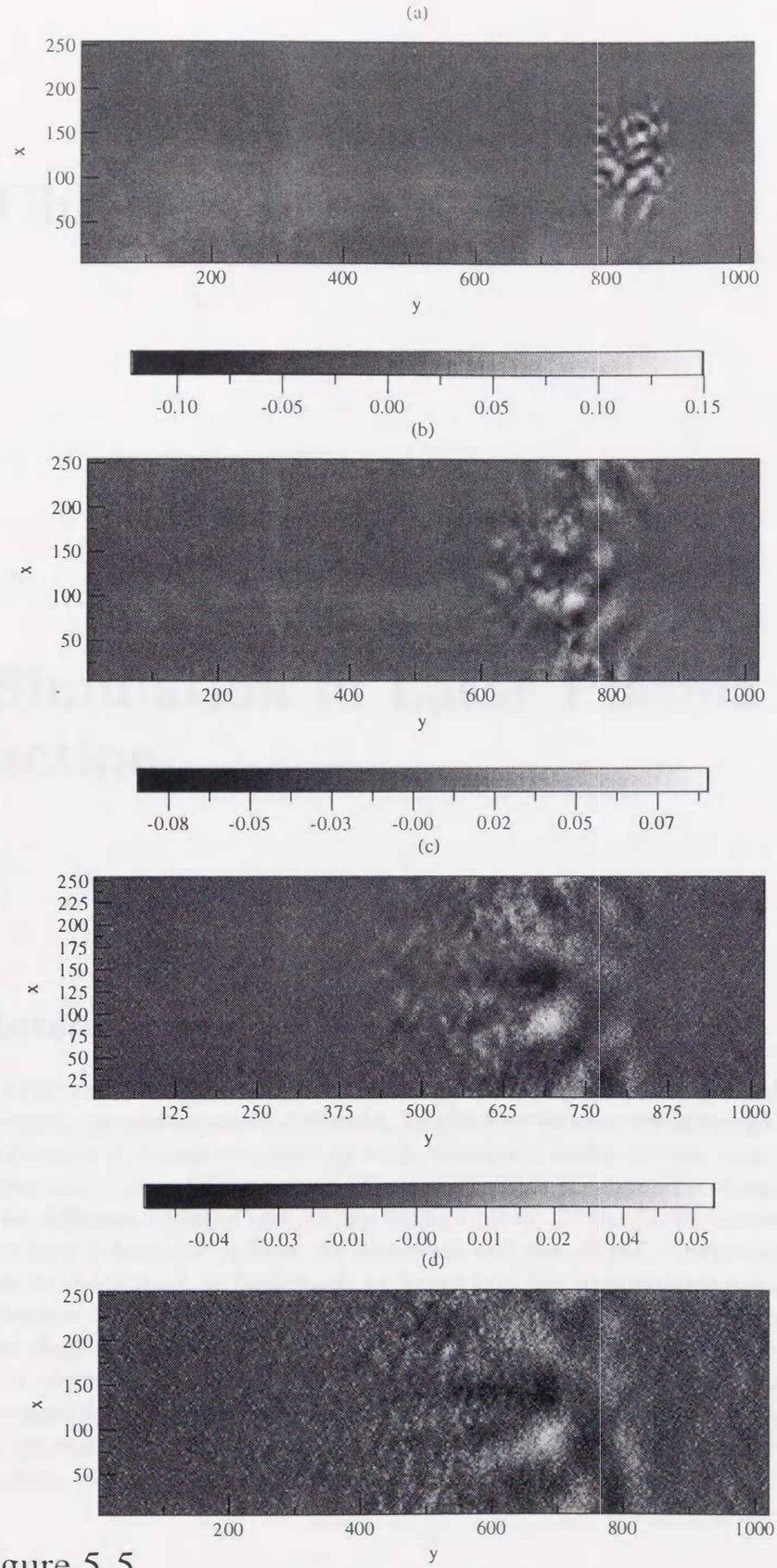

Figure 5-5

The time development of magnetic field(Bz) structures in x-y plane. (a)=25ω_{pet}, (b)=50ω_{pet}, (c)=75ω_{pet}, (d)=100ω_{pet}.

Chapter 3

Simulation of Laser Plasma Interaction

Introduction

In this chapter, we present the results of two dimensional PIC (Particle-in-Cell) simulations of plasma cloud collisions. In the first section, we investigate the collision dynamics of counter-streamings with cylindrical configuration. And we found that there occur two different kinds of instabilities: In the second section, we investigate two different types of the plasma configuration: in the first one the initial configuration is assumed to have the slab form and the second configuration has a form of the cylindrical. In both cases we found that the counter-streaming motion of the plasmas is unstable with respect to the electromagnetic mode excitation with the developing of the hollow structures in the electron density distribution, the formation of the electric current filaments and the merging of the filaments and quasistatic magnetic field generation. These processes may be important for understanding of magnetic field generation and its structures in plasmas interacting with strong laser pulses.

6 MAGNETIC FIELD GENERATION DURING THE COLLISION OF COUNTER STREAMING FLOWS

6.1 Introduction

We present results of 2D3V PIC simulations of electron-ion plasma clouds collision, which are obtained by modifying the $3D3V$ TRISTAN code (Buneman[16]). In our recent papers [23][24], we investigated that a quasi-static magnetic field can be generated associated with the counter-streaming instability. In that simulation, we found that the magnetic field is produced in the direction perpendicular to streams and it develops to a large scale structure in the nonlinear stage.

In the present paper, we investigate the collision dynamics of counter-streamings with cylindrical configuration. We found that there occur two different kinds of instabilities: one looks like the Weibel [3] instability that occurs in a plasma with anisotropic temperature, the other is the Diocotron instability. When the velocity, electric field, and magnetic field are mutually perpendicular, the unstable mode is known as the Diocotron instability. As an application like this plasma, we mention the plasma around fuel pellet carrying out the direct drive implosion, which is the heating method of the fusion material. In the plasma, some particles can be accelerated by laser pulse irradiating to the fusion material. Company with the particle acceleration, a current which direction is opposite to the propagation of laser can be produced. So the particles in the plasma interacts with the laser pulse, and cause some instabilities. In this kind of interaction process, it is essential to consider the relativistic effect owing to the relativistic electron acceleration.

6.2 Simulation Model

The system size used in the simulation is $L_x = 256\Delta$ and $L_y = 256\Delta$. Periodic boundary conditions on the fields and particles are used in both x and y directions. The particle number density is about 20 particles per cell. $\Delta = 1.0$ is a grid size.

The ions are assumed to be at rest. Initially the electrons have two counter-streaming components with different velocities and densities. We give the electron velocity distribution as shifted Maxwellian with $v_{1e} = 0.3c$ and $v_{2e} = -0.6c$ in the z-direction and each density is $n_{1e} = 2n_{0e}/3$ and $n_{2e} = n_{0e}/3$, where the condition $\sum n_{ea} v_{ea} = 0$ is satisfied. c is the light velocity and n_{0e} is the initial electron number density. Those particles are distributed with cylindrical configuration in the center of the system. The radius of cylindrical configuration is 64Δ. The other parameters are as follows: the mass ratio $m_i/m_e = 64$, $\omega_{pe}\Delta t = 0.05$, where Δt is the integration time step, the electron collision-less skin depth is $d_e = c/\omega_{pe} = 9\Delta$.

6.3 Simulation Results

The main result is the generation of magnetic fields B_x and B_y perpendicular to the stream direction. We study the structure of the electric currents in the nonlinear stage which are associated with the quasi-static magnetic field.The electric fields E_x and E_y also appear in the perpendicular direction to the initial flow owing to the instability. The electrons which have a drift velocity in z-direction are accelerated or decelerate by the electric field produced in x-y plane. So we think that the formation of electric current J_z from the current-less stream is the result of interaction between charged particles and laser pulse.

At first Fig.6-1 shows the development of current J_z which is obtained from the rotation of generated magnetic fields B_x and B_y. Initially, there appear structures which characteristic scale is about the electron skin depth. This instability corresponds to the Weibel-type instability, which is investigated in the literatures [6][24]. The thermal velocity in all directions are the same. But we set a drift velocity in z-direction, so there is the anisotropy between the z-direction and other directions. Therefore we called it Weibel-type instability. The structures which scale are electron skin depth appear by Weibel-type instability. But in the nonlinear stage, the electric current structure becomes large scale as time goes on owing to $\mathbf{J}\times\mathbf{B}$ force of the current filaments with the same current directions.

Fig.6-2 shows the vector plots of the electric fields E_x and E_y in the x-y plane. We find that the electric field appears in perpendicular direction to the magnetic field, by comparing the magnetic field vectors in Fig.6-1-c and the electric field vectors, in Fig.6-2 at the same points in the plane. We also find that the direction of these vectors is perpendicular to the stream velocity. The characteristics that the velocity, electric field, and magnetic field are mutually perpendicular, is known as the Diocotron instability. Fig.6-3 shows the time history of magnetic field energy in the direction perpendicular to the streams. The structure of the magnetic field also develops to a large scale as well as the current structure.

By using the final value of magnetic field energy, we can estimate the energy conversion rate from the initial flow energy. We find that the energy conversion rate is about 20%. The other energy almost converted to electron and ion energy. Fig.6-4 and Fig.6-5 show the structure of density distribution and charge density at the final time, respectively. The structure of density distribution is very similar to the structure of charge density. It is also characteristics of the Diocotron instability. On the other hand, the structure of density distribution is different from the current structure, as seen Fig.6-1-c.

In order to study the energy flow in the wave number space, we performed a 2-D Fourier transformation of current J_z in the x and y direction. As shown in Fig.6-6, there occurs the energy flow from large wave-number to small wave number region, which is called as the "Inverse cascade" process. That is to say, it means that the structure of current J_z becomes larger.

6.4 Summary

We present results of 2D3V PIC simulations of electron-ion plasma clouds collision. There occur two different instabilities: one is the Weibel-type instability and the other is the Diocotron instability, which is characterized that flow velocity, electric field, and magnetic field are mutually perpendicular. The most important result is the generation of magnetic fields in the direction perpendicular to streams and its structure develops to a large scale. These processes may be important for understanding magnetic field generation in plasmas interacting with strong laser pulses.

Figure captions

Figure 6-1. Time development of current (J_z) structures in the $x-y$ plane: (a) $\omega_{pe}t = 10$, (b) $\omega_{pe}t = 20$, and (c) $\omega_{pe}t = 50$, with $B_x - B_y$ vector plots.

Figure 6-2. The vector plots of electric field $E_x - E_y$ at $\omega_{pe}t = 50$.

Figure 6-3. The time history of magnetic field energy in the direction perpendicular to the streams.

Figure 6-4. The electron density distribution at $\omega_{pe}t = 50$.

Figure 6-5. The structure of charge density at $\omega_{pe}t = 50$.

Figure 6-6. Intensity of J_z as a function of k_x and k_y: (a) $\omega_{pe}t = 10$, (b) $\omega_{pe}t = 50$.

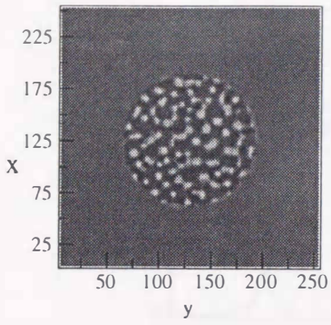

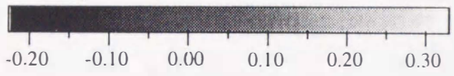

Figure 6-1-a

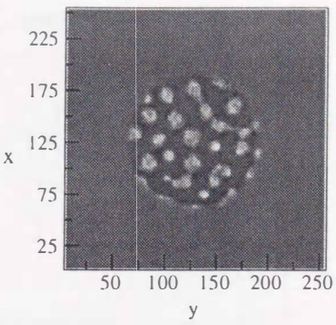

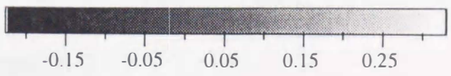

Figure 6-1-b

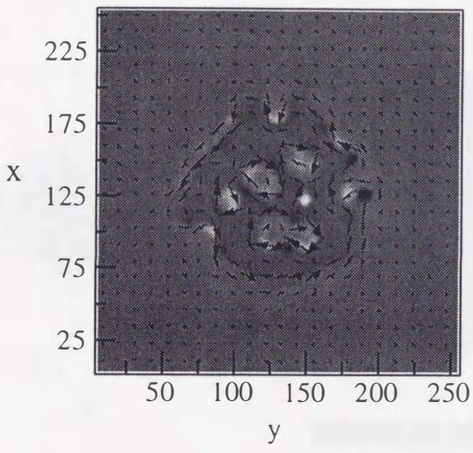

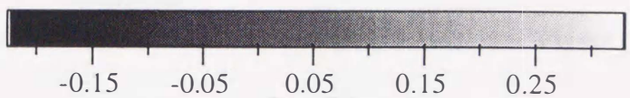

Figure 6-1-c

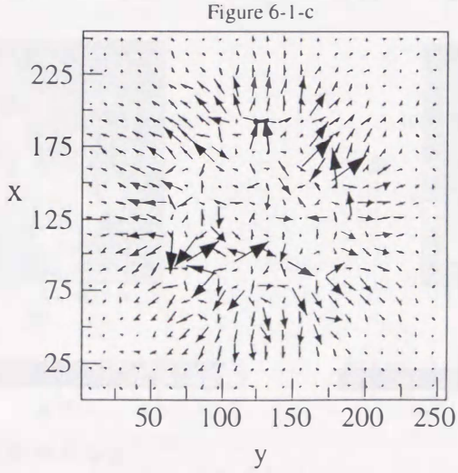

Figure 6-2

→ = 0.13212

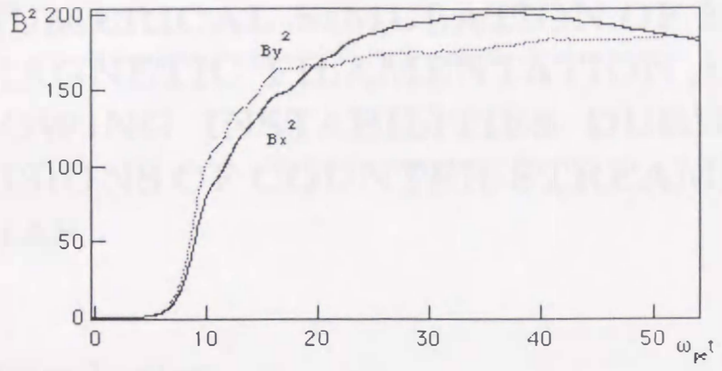

Figure 6-3

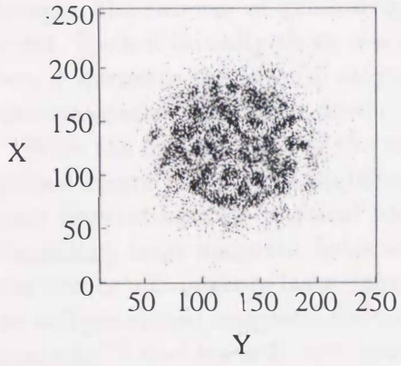

Figure 6-4

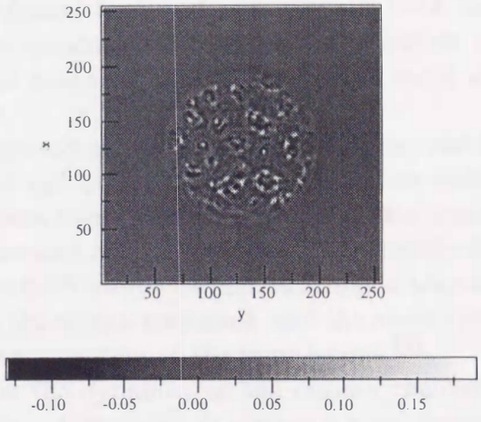

Figure 6-5

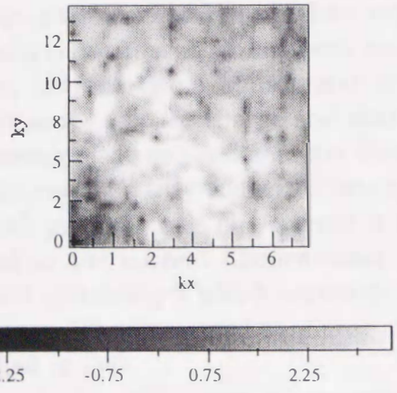

Figure 6-6-a

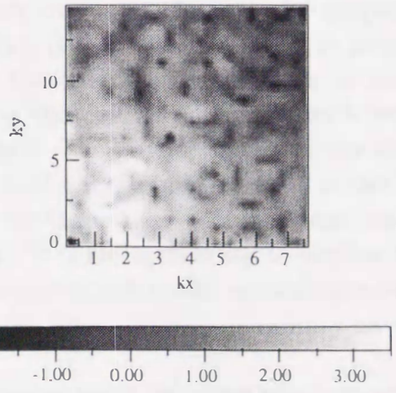

Figure 6-6-b

7 NUMERICAL SIMULATION OF ELECTROMAGNETIC FILAMENTATION AND HOLLOWING INSTABILITIES DURING COLLISIONS OF COUNTER-STREAMING PLASMAS

7.1 Introduction

Studies of colliding plasmas since a long time have had relation to the problems ranging from the applications of intense charged particle beams in high-current accelerators[26,27,28] to the problems of astrophysical plasmas.[11,12,29] In the colliding plasmas, the intense of generated self-electric field and self-magnetic field are observed. Even if initially there is a charge quasineutrality and a compensation of the electric currents the intense electric and magnetic fields appear as a result of the electromagnetic instability development.

With the development of the technique of chirped pulse amplification, which has enabled lasers to produce multiterawatt and petawatt femtosecond laser pulses,[30] many interesting new physical phenomena came within our grasps. For example, exceedingly large magnetic fields are generated in laser plasmas. They modify the interaction of ultraintense laser pulses with both overdense and underdense plasmas.[31] The self-generated magnetic fields affect the energy transport, and the overall plasma expansion[32] and leads to the bending and merging of the laser beams.[13]

Recently the experimental results on the dynamics of the plasma channel produced by a high intensity short laser pulse propagating in a plasma were reported in Ref. [33], where the self-focusing and channeling of the laser pulse, plasma channel formation, and the dynamics of ambient gas excitation and ionization were observed. Rapid surrounding gas ionization has been observed after the channel formation and it was attributed to the fast ions expelled from the laser channel and propagating radially outwards. As it has been noticed in Ref. [11] the fast ions cannot propagate alone, they carry an appropriate number of free electrons with them in order to compensate a space charge and therefore form the colliding plasmas with counter-streaming electrons and zero net electric current. The kinetic energy of the electron beams can be partly converted into magnetic field energy in the course of the beam-plasma instabilities. The current is unstable for transverse perturbations, and it is called as the current filamentation instability.[34] This instability is similar to the Weibel instability[3] which occurs in a collisionless plasma with an anisotropic temperature. The linear and nonlinear aspects of the filamentation instability have been studied in [34].

In the present paper, we investigate the dynamics of colliding plasmas with the two dimensional in real space and three dimensional in velocity space fully relativistic electromagnetic PIC code, which has been obtained by modifying the $3D3V$

-TRISTAN code.[16] We investigate two different types of the plasma configuration: in the first one the initial configuration is assumed to have the form of a slab and is the second moving plasma has cylindrical form. In both cases we found that the counter-streaming motion of the plasmas is unstable with respect to the electromagnetic mode excitation with the developing of the hollow structures in the electron density distribution, formation and merging of the electric current filaments and quasistatic magnetic field generation.

7.2 Simulation Model

We used the 2D3V fully relativistic electromagnetic PIC code. The net electric charge and electric current are initially compensated. The electrons form two counter-streaming components moving along the z-axis in opposite direction with different velocities and densities. The electron velocity distribution is given by the shifted Maxwellian

$$f_{ea}(\mathbf{v}) = \frac{n_{ea}}{(2\pi v_{tha}^2)^{3/2}} \exp\left(-\frac{v_x^2 + v_y^2 + (v_z - v_{ea})^2}{2v_{tha}^2}\right), \quad a = 1, 2 \tag{32}$$

with $v_{e1} = 3v_{th}$ and $v_{e2} = -6v_{th}$. The electron thermal velocity v_{th} is $0.1c$, where c s speed of light in vacuum. The density is $n_{e1} = 2n_0/3$ and $n_{e2} = n_0/3$ for the electrons moving in the positive and negative direction along the z-axis, respectively. The conditions $\sum n_{ea} v_{ea} = 0$ and $\sum n_{ea} = n_0$ are satisfied. Here n_0 is the total ion density. The ion temperature is the same as the electron temperature. The ion velocity distribution is also given by the Maxwellian without drift velocity.

We consider two configurations of the colliding plasma clouds.

In the first configuration the clouds initially are in the slab region of which width is 50Δ in the $y-$direction. Here the mesh size is equal to $\Delta = d_e/9$, where the collisionless skin depth is $d_e = c/\omega_{pe}$. The integration time step is $\Delta t = 0.05\omega_{pe}^{-1}$. Here the Langmuir frequency is $\omega_{pe} = (n_0 e^2/\varepsilon_0 m_e)^{1/2}$,$(\varepsilon_0 = 1)$.

The simulation region in this case has the length $L_x = 200\Delta$ in the x-direction and $L_y = 100\Delta$ in the y-direction. The periodic boundary conditions for the electromagnetic fields and particles were imposed in the $x-$ and $y-$ directions. The particle number density is about 20 particles per cell.

In the second configuration, the counter-streaming plasma clouds are initially inside the cylinder with radius equal to 64Δ. We consider two cases; the case that we have a vacuum outside the cylindrical column of the plasma and the other case that the counter-streaming plasmas are embedded into the plasma with initial zero velocity and the density of n_0 outside the cylinder. The simulation size in this case has the length $L_x = 256\Delta$ in the x-direction and $L_y = 256\Delta$ in the y-direction. Other parameters are the same as those in the case of the slab geometry.

The ion to electron mass ratio is equal to $m_i/m_e = 1836$.

7.3 The Plasma Cloud Collision in the Slab Configuration

We consider the collision of two counter-moving plasma clouds in a slab configuration as shown in Fig. 7-1 ,where the distribution of the $z-$component of the electric

current density and the vector plot of the magnetic field in the $x, y-$plane are presented at different time. Here and below the size is normalized by the collisionless skin depth c/ω_{pe}. The current density in this figure is normalized by $J_0 = (\mu_0 c\Delta)^{-1}$,$(\mu_0 = 4, c = 0.5)$. No plasma is assumed to be outside the slab in the initial configuration. We see in Fig. 7-1 (a) that at time $16\omega_{pe}^{-1}$ the filamentation of the electric current density appears. The typical transverse size of the filaments is about the collisionless skin depth c/ω_{pe}, in accordance with the linear theory of the current filamentation instability.[34] Then at time $80\omega_{pe}^{-1}$ the filaments merge and form the large scale configuration of the electric current and the magnetic field in Fig. 7-1 (b). At this time just several electric current filaments with the size of the order of c/ω_{pe} remain at the plasma-vacuum interface. Eventually, at time $240\omega_{pe}^{-1}$ the quasi-homogeneous configuration in the $x-$direction is formed as it is seen in Fig. 7-1 (c). Intense magnetic field is generated in the vicinity of the plasma-vacuum interface in the direction perpendicular to the plasma cloud velocity. The magnetic field is mainly located between two layers at the plasma boundaries with wide neutral region in the center of the slab. This configuration is stable.

The analysis of the velocity distribution of electrons shows the isotropization and formation of qusithermal configuration with the temperature equal to the kinetic energy of the electron motion in the initial configuration.

The analysis of the linear regime of the instability shows that the estimated growth rate of the instability is of the order of $0.41\omega_{pe}^{-1}$. The maximum of the growth rate calculated analytically[34] is about $0.33\omega_{pe}^{-1}$ at the wave number $k_y = 0.84\omega_{pe}/c$. The efficiency of the conversion of the electron kinetic energy to the energy of the magnetic field energy is about 11%.

The filamentation of the plasma flows also lead to the excitation of magnetic field in the longitudinal direction. In Fig. 7-2 the $z-$component of the magnetic field is presented in the $x, y-$plane. The intensity of the magnetic field in this figure is normalized by $B_0 = (c \cdot B)$. We see in Fig. 7-2 (a) that at time $40\omega_{pe}^{-1}$ the regions of opposite polarity of the magnetic field appear. They correspond to the chains of the electron vortices with the size about the collisionless skin depth c/ω_{pe}. Then at time $80\omega_{pe}^{-1}$ when the electric current filaments merge the $z-$component of the magnetic field forms smoother configuration (see Fig. 7-2 (b)). At time $240\omega_{pe}^{-1}$ only one large scale electron vortex can be identified in Fig. 7-2 (c).

In Fig. 7-3 we present the electron phase plane (v_z, y). In Fig. 7-3 (a) we see two counter-propagating electron beams which corresponds to the initial configuration. The phase plane develops then into the plane shown in Fig. 7-3 (b). We see that the low density and faster beam is expelled from the slab and also we see large gradients of the electric current density at the periphery of the slab at $y = 30\Delta \sim 3.33c/\omega_{pe}$ and $y = 70\Delta \sim 7.77c/\omega_{pe}$. Since magnetic field are generated like surrounding particles, electric field in z-direction are generated as seen Figure Ez-structure. That is why the energy of the high density and slower beam particles located in center decreased.

7.4 The Plasma Cloud Collision in the Cylindrical Configurations

We simulated two different types of cylindrical configurations: the first one is the case that we have a vacuum in outside the cylinder column of the plasma. The second one is the case of the effects of the ambient plasma on collision of two cylindrical plasma clouds. We consider the first case of the collision of two counter-stream plasma clouds in a cylindrical configuration as it is shown in Fig. 7-4 ,where the distribution of the z-component of the electric current density and the vector plot of the magnetic field in the $x, y-$plane are presented at different time. We see that at time $50\omega_{pe}^{-1}$ the filamentation of the electric current density appears. The typical transverse size of the filaments is about the collisionless skin depth c/ω_{pe}, as in the case of the slab geometry discussed above. At this time we see strong modulation of the plasma-vacuum interface. The filamentation of the electric current is accompanied by the magnetic islands distinctively seen in Fig. 7-4 (a) and the filamentation seen in the $x, y-$distribution of the electron (a),(b) and ion (c) density presented in Figs. 7-5. Finally the quasi-equilibrium configuration is formed at time $150\omega_{pe}^{-1}$ (see Fig. 7-4 (b)), when the coalescence of the magnetic islands completed. This configuration has hollow structure seen in the distribution of the electric current and the magnetic field in Fig. 7-4 (b). The magnetic field directed perpendicularly to the plasma cloud velocity has the form of coaxial rings with the opposite direction of the field inside the rings and circular neutral line in between of the rings. The structure of the generated $z-$component of the magnetic field (see Figs. 7-6 (a) and (b)) correlates with the structure of the filamentation and hollowing of the $z-$component of the electric current. The magnetic flux is almost confined in current filament and hollowing electric current. This configuration is stable. We notice that the analytical description of the hollowing instability of intense electron beams in plasmas has been presented in Ref. [28]. The efficiency of the conversion of the electron kinetic energy to the energy of the magnetic field energy is about 20%. We consider the next case. In this case we assume the counter-streaming plasmas to be embedded into the plasma with initial zero velocity and the density equal to n_0 outside of the cylinder. Other initial conditions are the same as those in the case considered above.

In Fig. 7-7, we present the distribution of the $z-$component of the electric current density and the vector plot of the magnetic field in the $x, y-$plane at different time. The patterns of the electric current distribution is different to those which are shown in Fig. 7-4. We see in Fig. 7-7 (a) that in the initial stage of the instability development at $t = 25\omega_{pe}^{-1}$ the electric filaments are generated. Their transverse size is about the collisionless skin depth c/ω_{pe} and there is no any evident regular structure. Then at $t = 50\omega_{pe}^{-1}$ the self-organization occurs with two large filaments in center (the radius $\approx 3c/\omega_{pe}$) encircled by eight smaller filaments with the radius of each of them $\approx c/\omega_{pe}$ (see Fig. 7-7 (b)). The small filaments are localized approximately on the circle with the radius $\approx 10c/\omega_{pe}$, which is fairly larger than the initial radius of the moving plasma. Finally at $t = 150\omega_{pe}^{-1}$ the distance between two central filaments increases and they break the symmetry as it is seen in Fig.

7-7 (c). This pattern is apparent also in the distribution of the $z-$component of the magnetic field shown in Fig. 7-8. We see in Fig. 7-8,the patterns of the magnetic field structure which size is initially about collisionless skin depth c/ω_{pe}, coalesced and developed large scale structures. In Fig. 7-8 (c), comparing with Fig. 7-7(c) the direction of two large current filaments are the same. But in Fig. 7-8, in the same place where two current structures are stable, the component of z-direction magnetic field has opposite polarity. So to say, we see that the $z-$component of the magnetic field has opposite polarity inside large filaments. The magnetic configuration in this case corresponds to the counter-helicity magnetic field.

7.5 Discussion

In conclusion, we observed nonlinear development of the electromagnetic current filamentation-hollowing instability. This instability leads to formation of the electric current filaments with the transversal size of the order of the collisionless skin depth. The merging of current filaments correspond to the magnetic islands coalescence. Eventually this process leads to the formation of the quasi-equilibrium, stable configuration. This configuration has a form of separated electric current filaments and it is associated with the magnetic islands and vortices. The self-generated magnetic field is directed both perpendicularly and parallel to the direction to the initial plasma velocity. The distribution of the electric current has a form of cylindrical, well separated layers. The conversion rate of the electron kinetic energy into the energy of self generated magnetic field is about $10-20\%$.

Figure Captions

Figure 7-1. Distribution of the z-component of the electric current density (in frames (a), (b) and (c)) and the vector plot of the magnetic field (in frames (b), and (c)) in the $x, y-$ plane in the slab configuration: (a) $t = 16\omega_{pe}^{-1}$, (b) $t = 80\omega_{pe}^{-1}$, (c) $t = 240\omega_{pe}^{-1}$.

Figure 7-2. The $z-$component of the magnetic field in the $x, y-$plane at $t = 40\omega_{pe}^{-1}$,(a), $t = 80\omega_{pe}^{-1}$, (b), and $t = 240\omega_{pe}^{-1}$, (c).

Figure 7-3. Electron phase plane (v_z, y) in the slab geometry at $t = 0$, (a) and $t = 240\omega_{pe}^{-1}$, (b).

Figure 7-4. The $z-$component of the electric current density and the vector plot of the magnetic field in the $x, y-$plane at $t = 50\omega_{pe}^{-1}$,(a), and $t = 150\omega_{pe}^{-1}$,(b).

Figure 7-5. Distribution of the electron and ion density in the $x, y-$ plane: $t = 0$, electron density (a), $\omega_{pe}t = 150$, electron density (b) and $\omega_{pe}t = 150$ ion density (c).

Figure 7-6. The $z-$component of the magnetic field in the $x, y-$plane at $t = 50\omega_{pe}^{-1}$,(a), and $t = 150\omega_{pe}^{-1}$,(b).

Figure 7-7. The $z-$component of the electric current density and the vector plot of the magnetic field in the $x, y-$plane at $t = 25\omega_{pe}^{-1}$,(a), $t = 50\omega_{pe}^{-1}$, (b), and $t = 150\omega_{pe}^{-1}$, (c).

Figure 7-8. The $z-$component of the magnetic field in the $x, y-$plane at $t = 25\omega_{pe}^{-1}$,(a), $t = 50\omega_{pe}^{-1}$, (b), and $t = 150\omega_{pe}^{-1}$, (c).

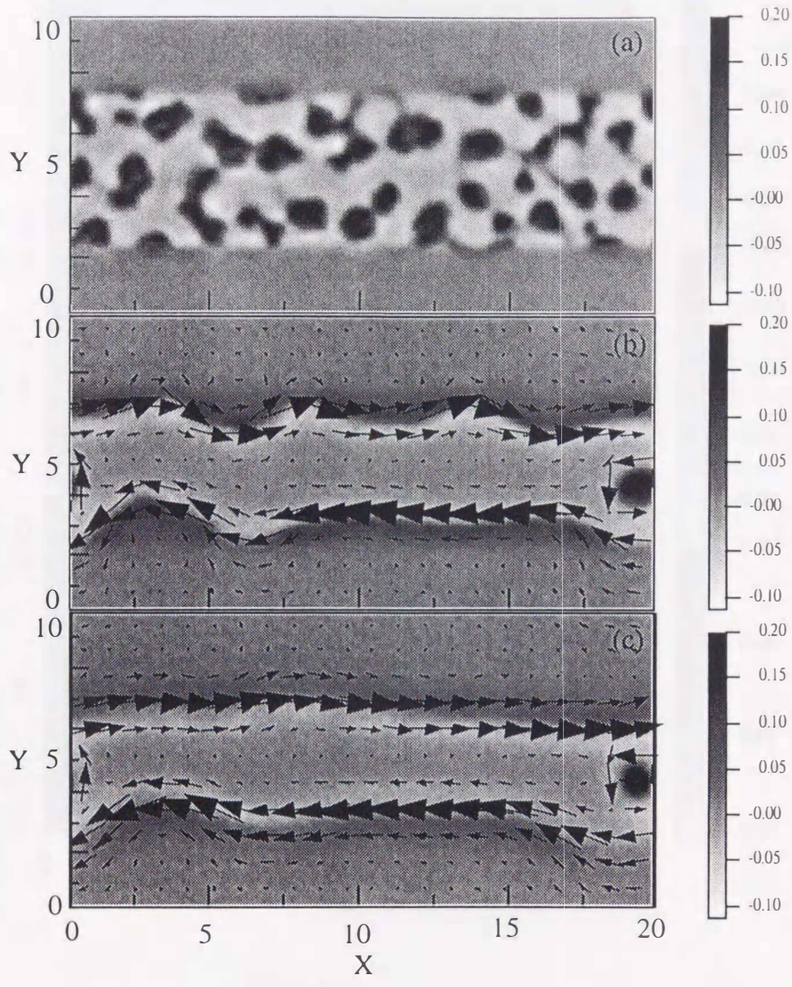

Figure. 7-1

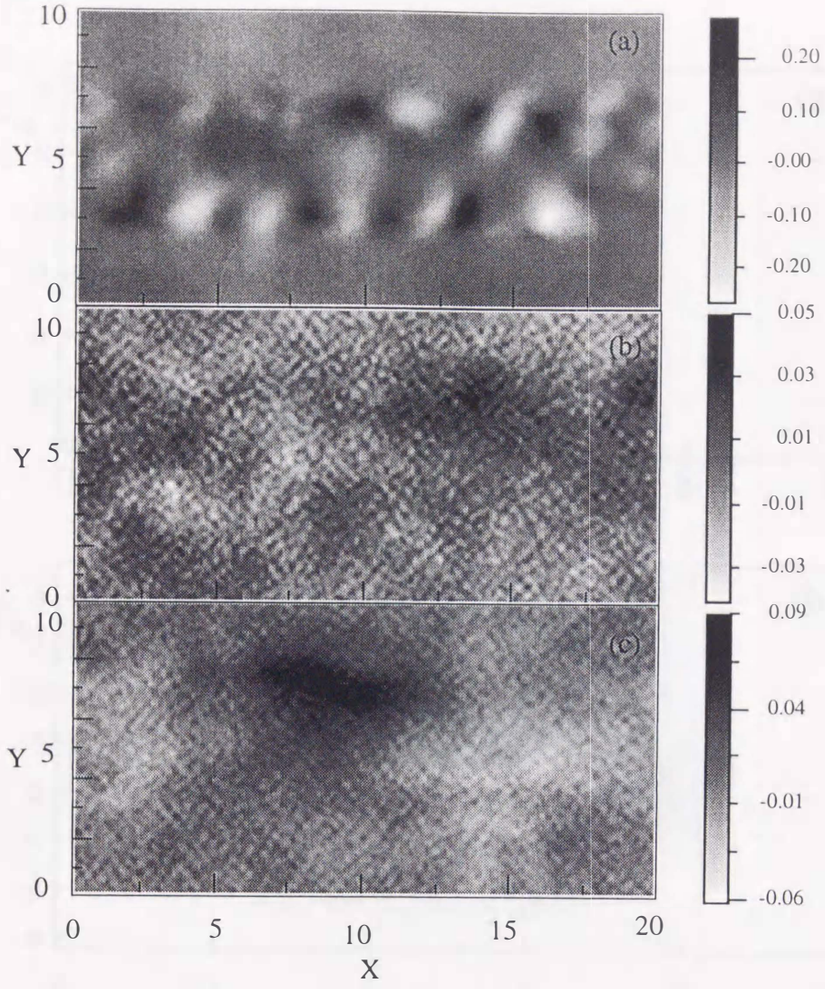
10
(a)
Y 5
0
0.20
0.10
-0.00
-0.10
-0.20
10
(b)
Y 5
0
0.05
0.03
0.01
-0.01
-0.03
10
(c)
Y 5
0
0.09
0.04
-0.01
-0.06
0
5
10
15
20
X

Figure. 7-2

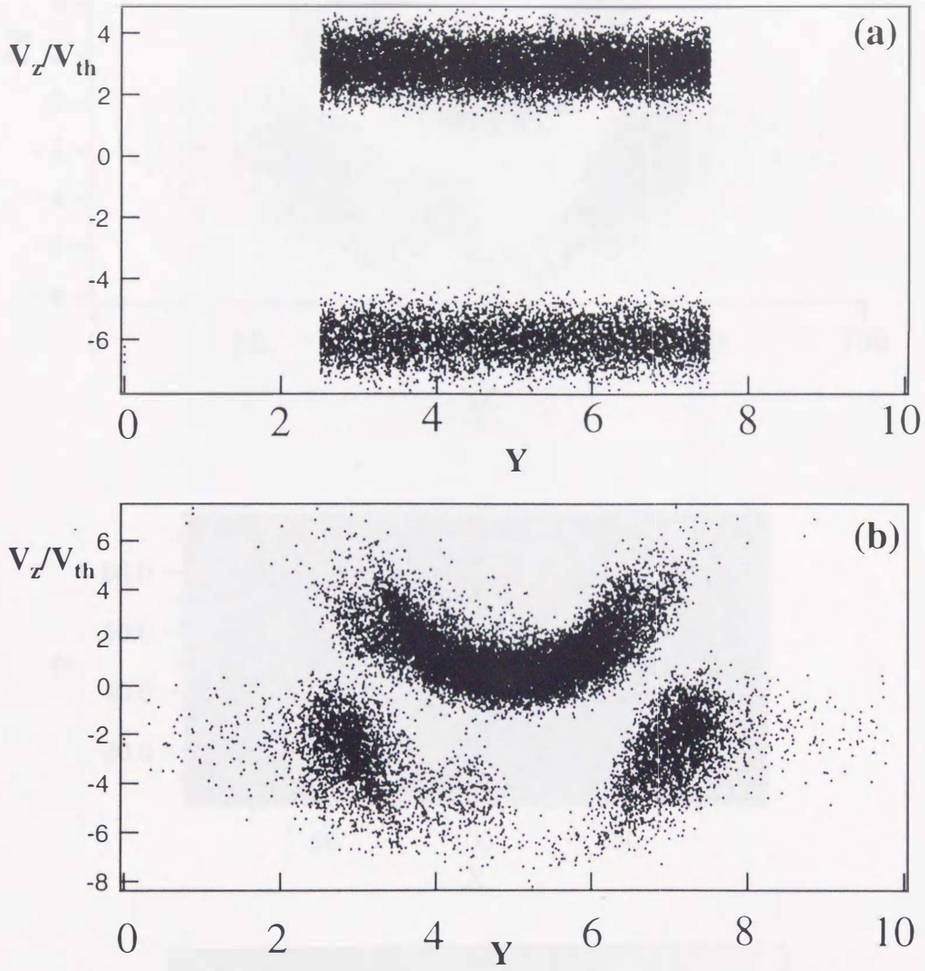

Figure. 7-3

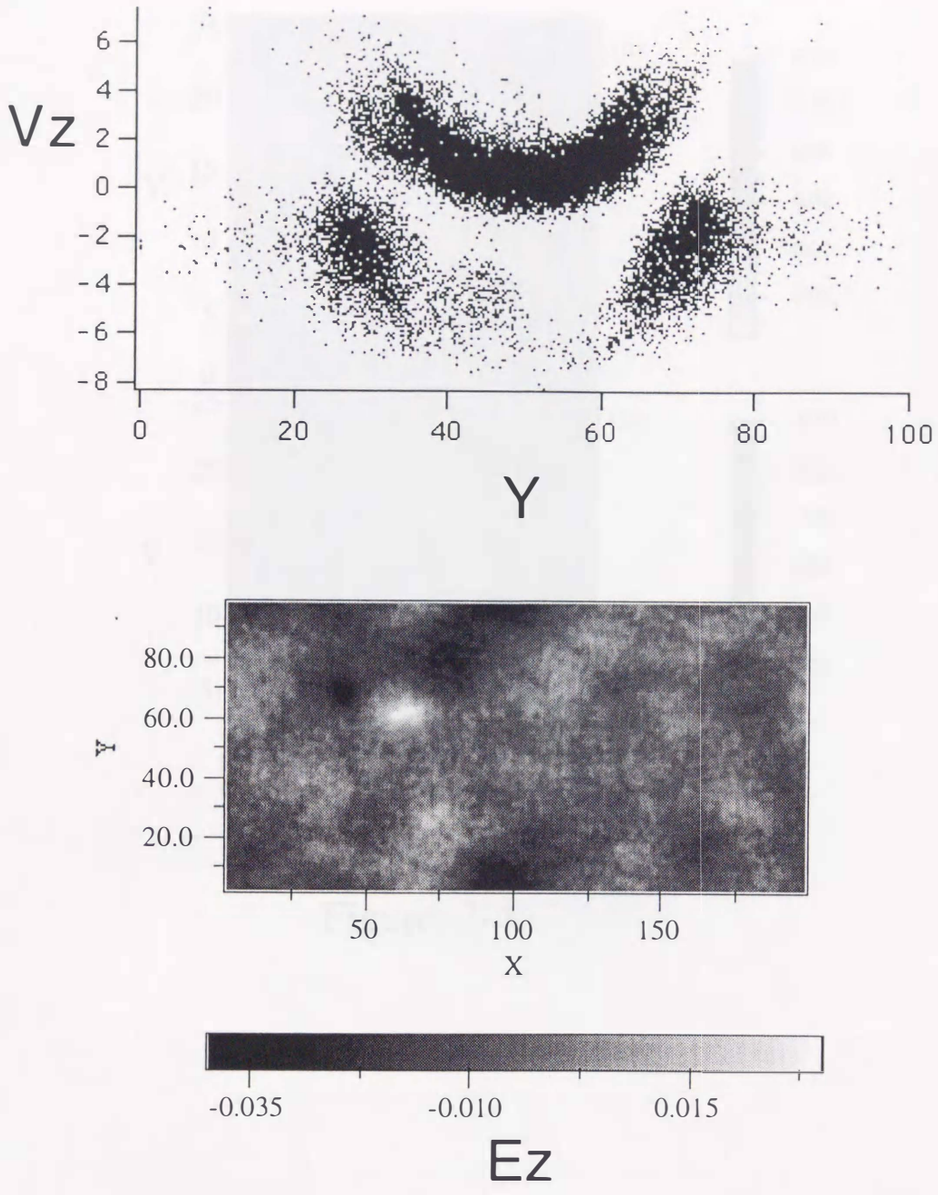
Vz
6
4
2
0
-2
-4
-6
-8
0
20
40
60
80
100
Y
80.0
60.0
40.0
20.0
Y
50
100
150
X
-0.035
-0.010
0.015
Ez

Figure 7-3-2

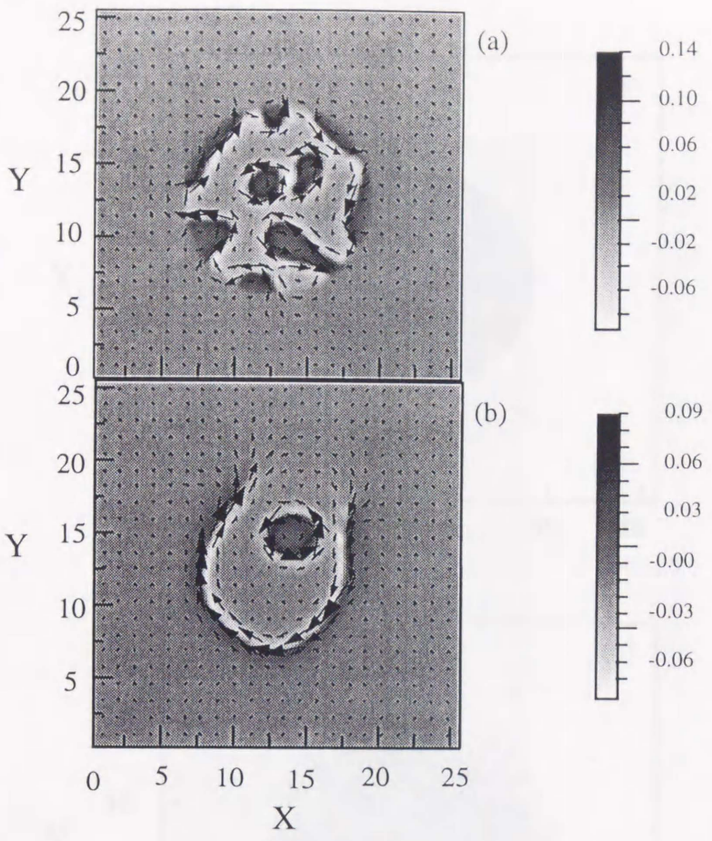
(a)
(b)
Y
X
25
20
15
10
5
0
0.14
0.10
0.06
0.02
-0.02
-0.06
0.09
0.06
0.03
-0.00
-0.03
-0.06

Figure. 7-4

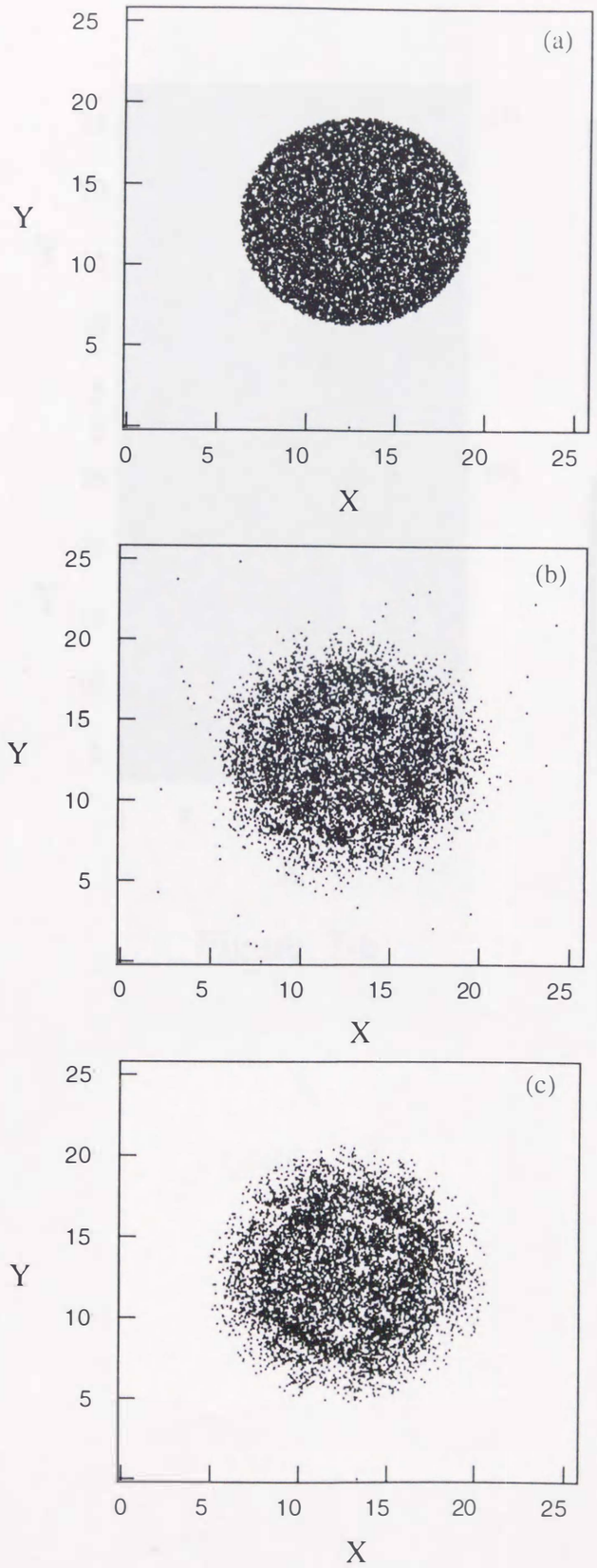
(a)
25
20
15
10
5
Y
0
5
10
15
20
25
X
(b)
25
20
15
10
5
Y
0
5
10
15
20
25
X
(c)
25
20
15
10
5
Y
0
5
10
15
20
25
X

Figure. 7-5

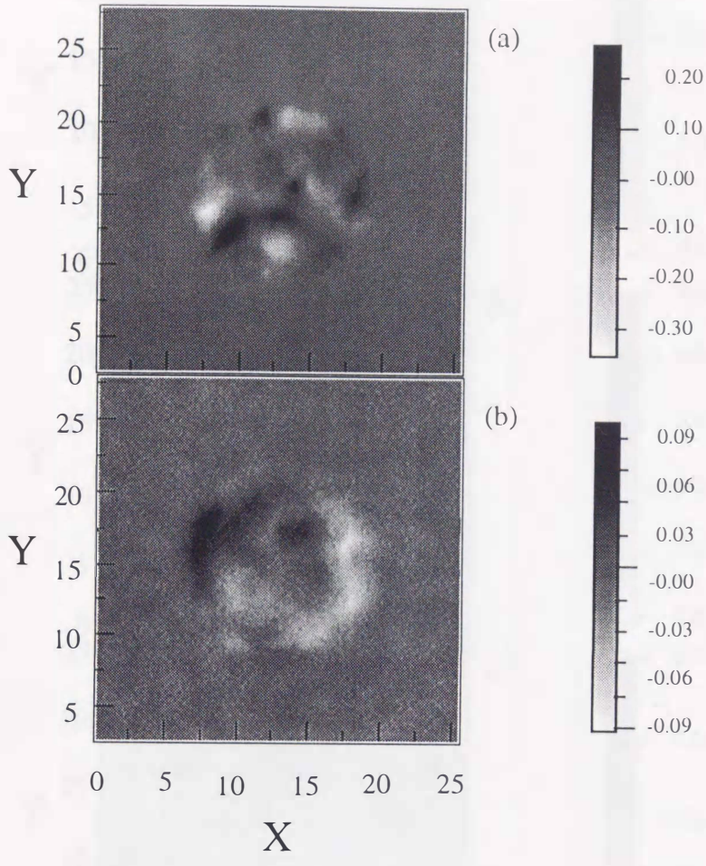
(a)
(b)
Y
X
25
20
15
10
5
0
0.20
0.10
-0.00
-0.10
-0.20
-0.30
0.09
0.06
0.03
-0.00
-0.03
-0.06
-0.09

Figure. 7-6

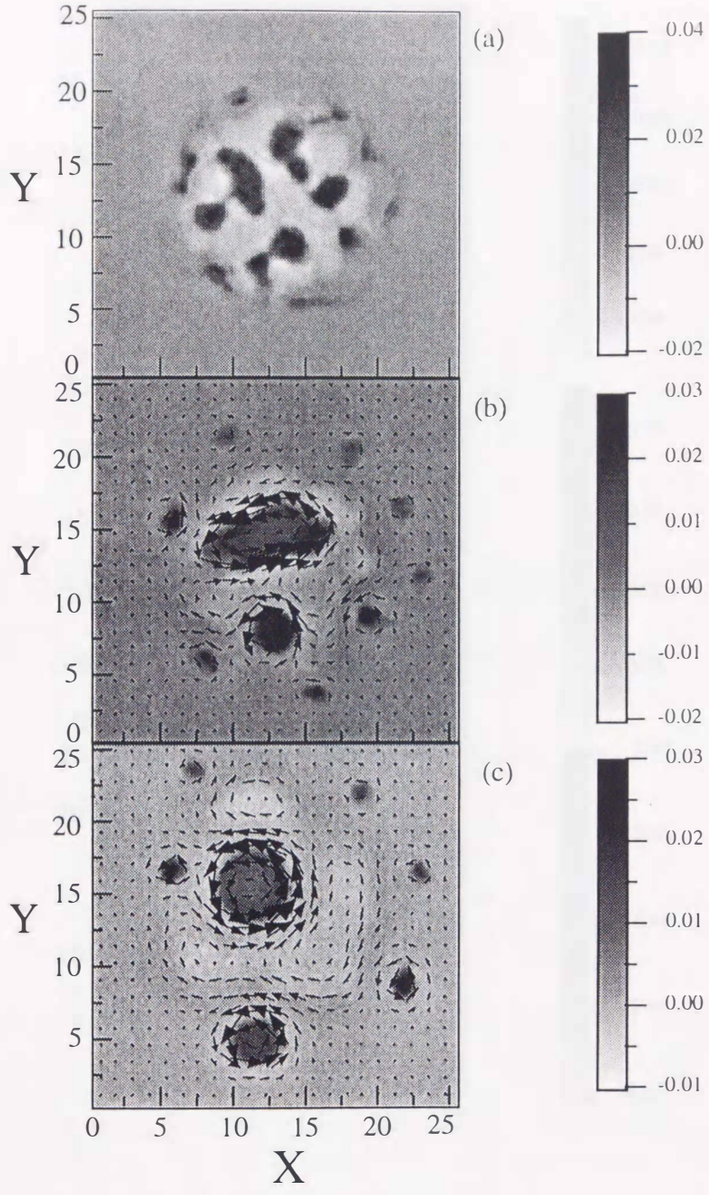

Figure. 7-7

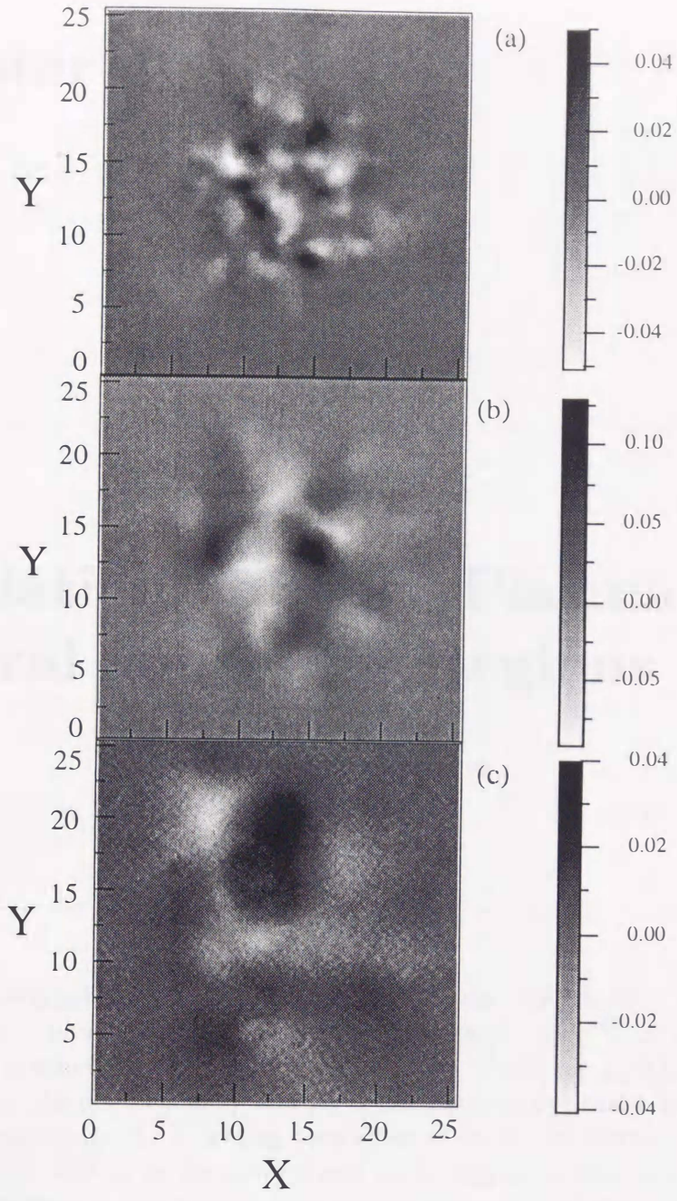

Figure. 7-8

Chapter 4

Simulation of Space Plasma in the Auroral and Polar Regions

Abstract

This part describes particle-in-cell simulations of electron/electron instabilities, using a two-dimensional fully relativistic electromagnetic code[16], in a homogeneous, collisionless, magnetized plasma model under the condition $\omega_e/|\Omega_e| \sim 1$ where ω_e is the electron plasma frequency and Ω_e is the electron cyclotron frequency. These simulations reproduce the following properties of enhanced electromagnetic fluctuations observed near ω_e in the auroral and polar regions of the terrestrial magnetosphere: 1) frequencies near the electron plasma frequency, 2) relatively large electric fields ($\delta E/\delta B \sim 20$), and 3) episodes of both right-hand and left-hand polarization. The simulations show that the right-hand polarized fluctuations are on the short wavelength beam mode and are excited by linear instability growth; the left-hand fluctuations are on the long wavelength domain of the Langmuir mode and appear to be excited by nonlinear wave-wave coupling.

8 ELECTROMAGNETIC FLUCTUATIONS NEAR THE ELECTRON PLASMA FREQUENCY FROM ELECTRON/ELECTRON INSTABILITIES

8.1 Introduction

The plasmas of the polar and auroral magnetosphere bear a strong terrestrial magnetic field and thus are often characterized by $\eta_e \equiv \omega_e/|\Omega_e| \lesssim 1$ [*Calvert*, 1981][35], where ω_e is the electron plasma frequency and Ω_e is the (signed) electron cyclotron frequency. In this plasma domain *Cairns and Menietti*[36] [1997] first reported the observation from the DE 1 spacecraft of intense electromagnetic radiation near the electron plasma frequency.

These plasma frequency events are observed to have the following properties. (1) They are relatively narrowband and intense in frequency about ω_e. (2) They typically have $|\delta E|/|\delta B| \sim 20$, which is substantially larger than the values observed for whistler waves in this plasma regime. (3) Their electric polarization varies: sometimes it is clearly right-hand, sometimes it is clearly left-hand, but most frequently observations yield an inconclusive result [*Menietti et al.*, 1998][38]. (4) They are sometimes accompanied by enhanced but weaker fluctuations near $2\omega_e$. *Cairns*[37] [1999] interpreted these events as corresponding to the enhancement of fluctuating electric fields of the z-mode near ω_e.

Menietti et al.[38] [1998] and *Gary and Cairns*[39] [1999] suggested that electron/electron instabilities may be the source of these enhanced plasma frequency fluctuations, but did not examine such instabilities in detail. The purpose of this manuscript is to describe theoretical and simulation research into the properties of electron/electron instabilities under parameters appropriate for the polar and auroral magnetosphere and to demonstrate that such properties well correspond to the observations of *Cairns and Menietti*[36] [1997] and *Menietti et al.*[38] [1998].

Electron/electron instabilities arise in collisionless plasmas when a tenuous electron beam (subscript b) propagates relative to a more dense electron core (subscript c) component with a sufficiently large beam/core relative drift velocity v_o. In an unmagnetized plasma these instabilities are electrostatic; that is, they have $\delta\mathbf{B} = 0$ and $\delta\mathbf{E}$ parallel to $\mathbf{k}$. In a magnetized plasma, if v_o is parallel to B_o, the background magnetic field, these instabilities remain electrostatic at propagation parallel to B_o, but gain an electromagnetic component (that is, $\delta\mathbf{E}$ and $\delta\mathbf{B}$ perpendicular to $\mathbf{k}$) at $\mathbf{k} \times \mathrm{B}_o \neq 0$.

Here we use fully electromagnetic particle-in-cell simulations to show that the oblique component of electron/electron instabilities can account for these magnetospheric observations. Previous electromagnetic simulations of these instabilities did not address this problem either because they considered only $\eta_e > 1$ [*Newman et al.*[45], 1988; *Yin et al.*[40], 1998; *Nambu et al.*[44], 1999] or because they assumed a large anisotropy on the beam, thereby exciting fundamentally electromagnetic instabilities [*Newman et al.*[45], 1988; *Winglee et al.*[41], 1992].

8.2 Linear Theory

For both our linear theory and the initial conditions of our simulations, we assume the following parameters: $\eta_e = 0.50$, $\beta_{\|e} = 0.0025$, $n_b/n_e = 0.10$, $v_o/v_e = 5.0$, and $T_e = T_c = T_b = T_i$. Although the beam density is exaggerated here because of computational constraints, the η_e and β_e values are representative of conditions in the auroral and polar magnetosphere. Figure 8-1 illustrates solutions to the fully electromagnetic linear Vlasov dispersion equation [*Gary*[42], 1993] using these parameters. Panel (a) shows results for $\theta = 0^o$, and panel (b) shows dispersion at $\theta = 30^o$.

For these parameters, we find only one linearly unstable mode, the electron/electron beam instability which is strictly electrostatic at parallel propagation. At $\mathbf{k} \times \mathbf{B}_o \neq 0$ we find three other modes, all stable: another electrostatic, Langmuir-like mode at $\omega_r \geq \omega_e$, and two electromagnetic modes, the right-hand polarized z/whistler mode, and the left-hand z/L-O mode. At oblique propagation the dispersion properties of each mode change, although the beam mode remains the sole unstable fluctuation. The beam instability develops an electromagnetic component, which is particularly strong at long wavelengths. The whistler remains right-hand polarized but becomes substantially electrostatic at relatively short wavelengths. At $\theta = 30^o$ the z-mode bears left-handed magnetic polarization at $\omega_r < \omega_e$, exhibits a substantial electrostatic component near the electron plasma frequency [*Cairns*[37], 1999], becomes predominantly electromagnetic with right-hand polarization at higher frequencies, and then becomes predominantly electrostatic at still higher frequencies and shorter wavelengths. The L-O mode is left-hand polarized for all frequencies shown here, but becomes substantially electrostatic as ω_r approaches the electron plasma frequency cutoff in the long wavelength limit.

8.3 Simulations

Gary et al.[43] [1999] reported particle-in-cell simulations of electron/electron instabilities at $\eta_e \sim 1$. These instabilities are fundamentally electrostatic at propagation parallel to $\mathbf{B}_o$, and have maximum growth rate at relatively short wavelengths. However, *Gary et al.*[43] [1999] showed that, as the angle between the wavevector and $\mathbf{B}_o$ is increased, these instabilities develop an electromagnetic component which is right-hand polarized. As the left-hand modes in this case are linearly stable, to account for the left-hand polarized observations, the wave energy has to get from the regime of maximum growth rate near $k/k_e = 0.25$ down to much longer wavelengths through some kind of nonlinear process. Here we extend the simulations of *Gary et al.*[43] [1999] to a larger system and to a longer time to permit nonlinear processes to accomplish this energy transfer.

We used a 2 1/2 dimensional fully relativistic electromagnetic particle-in-cell code [*Buneman*[16], 1993] for our simulations. The net electric charge and electric current are initially zero and the ion to electron mass ratio is equal to 64. The mesh size is taken to be $\Delta = c/\omega_e/10$, and the integration time step is $\delta t = 0.05\omega_e^{-1}$. The simulation size is $L_x = 18\Delta$ in the x-direction and $L_y = 1050\Delta$ in the y-direction. We used a simulation box which is long in the direction of the initial magnetic field

to permit the study of relatively long wavelengths. Periodic boundary conditions for the electromagnetic fields and particles were imposed in the $x-$ and $y-$ directions. The particle number density is about 25 particles per cell.

8.4 Simulation Results

Using the above parameters as initial conditions, we carried out a simulation of the electron/electron beam instability, and then did a detailed analysis of the results. Figure 8-2 shows the time history of the ratio of electric to magnetic field energy density. At early times, we found a large electric field energy compared with magnetic field energy, in agreement with observed property 2). After saturation of the fluctuating field energy, $|\delta E|^2/|\delta B|^2$ gradually decreased, suggesting a gradual transfer of fluctuation energy to longer wavelengths. Figure 8-3 shows the time development of the dispersion relation of δE_y propagating in the direction of B_o. Panels (a) through (d) show this dispersion at successively later times. At early times there are relatively intense fluctuations at the short wavelengths which correspond to the electron/electron beam instability. As time increases, the relatively intense fluctuations move to long wavelengths along a Langmuir-like mode near the plasma frequency.

Figure 8-4 shows the dispersion relation of δB_x and δB_z over $250 \leq \omega_e t \leq 300$. The beam mode still remains in both δB_x and δB_z components in later times. And relatively intense emission with long wavelength at the plasma frequency can be seen in Figure 8-4(b).

We checked polarization data at both short and long wavelengths. We got the polarization plots using data separated at each wavelength. It is difficult to confirm the polarization of electric component because it is mainly electrostatic. So we used the δB_x and δB_z components to determine magnetic polarization, using data translated from inverse Fourier analysis at each wavelength, long wavelengths, $-0.3 \leq kc/\omega_e \leq 0.3$ and small wavelengths, $1.4 \leq kc/\omega_e \leq 1.9$. In Figure 8-5 we show the polarization of Langmuir-like fluctuations with long wavelength, $-0.3 \leq kc/\omega_e \leq 0.3$. The intensity of the magnetic field in this figure is normalized by $B_0 = (c \cdot B)$. These two figures are polarization at different positions over $200 \leq \omega_e t \leq 220$. These show almost left-hand polarization. And its time development indicates almost the same statistics. Figure 8-6 shows the time development of statistics about right-hand polarization from (a) short wavelengths and (b) long wavelengths, respectively. At small wavelengths, this figure shows the right-hand polarization is dominant ,it is already known that polarization of beam mode is right-hand, and left-hand polarization exciting from the Langmuir-like fluctuation is dominant at long wavelength. And the statistics of left-hand property is increasing as time increases, that is why the the intensity of Langmuir-like mode gradually become large in consequence of translating energy from beam mode.

8.5 Summary

We have carried out fully electromagnetic particle-in-cell simulations of the electron/electron beam instability. These instabilities excite magnetic fluctuations at propagation oblique to $\mathbf{B}_o$, but don't change the dispersion because the fundamental unstable mode is still the electron/electron beam instability. So we hypothesize that narrowband electromagnetic plasma frequency fluctuations arise from the growth of electron/electron instabilities driven by tenuous electron beams.

The electron/electron modes are strongly electrostatic even in the presence of an electromagnetic component at oblique propagation. Thus, at oblique propagation, the fluctuating electric field is likely to have its two components transverse to $\mathbf{k}$ appear as uncorrelated, rather than correlated with right- or left- hand polarization as would an electromagnetic mode. So, most of the time the electric polarization is not defined well. We should conclude that the right-hand waves and other wave with inconclusive polarization which electrostatic component is dominant, are probably due to the electron/electron beam mode.

We reproduced the 3 of 4 properties of emission at near plasma frequency. (1) As we can see in Figure 8-3, it excites relatively narrowband and intense in frequency about ω_e. (2) That emission typically have intense $|\delta E|/|\delta B|$ in Figure 8-2. (3) Their polarization varies: sometimes it is clearly right-hand, sometimes it is clearly left-hand. In simulation, we found clearly differences of the magnetic polarization at different wavelength.

Our interpretation of these simulation results is that the right-hand and inconclusive polarization observations of *Menietti et al.*[38] [1998] are relatively short wavelength fluctuations driven directly by electron/electron instabilities, whereas the left-hand polarized observations correspond to relatively long wavelength fluctuations excited by these instabilities through wave-wave coupling. This interpretation raises the question as to why should not all such plasma frequency waves be observed to be right-hand or at best indeterminately polarized. Our hypothesis is that this category of fluctuations corresponds to direct observation; the spacecraft is immersed in, or very close to, the plasma bearing electron beams. However, if the spacecraft is remote from this source region, the short wavelength modes directly driven by the instability may not be able to propagate away from that source due to Landau damping, leaving only the long-wavelength, left-hand polarized modes to be observed.

Figure captions

Figure 8-1. Solutions of the linear Vlasov dispersion equation for the following parameters: $\eta_e = 0.50$, $\beta_e = 0.0025$, $n_b/n_e = 0.10$, $v_0/v_e = 5.0$, $T_e = T_c = T_b$ Real frequencies as function of wavenumber are shown as solid lines ($R_{es} \geq 0.5$, ;this means electromagnetic) and dashed lines ($R_{es} < 0.50$;this means electrostatic) ; the growth rate of the beam mode is shown as a dotted line. All other modes shown here are dumped. (a) $\theta = 0^o$. (b) $\theta = 30^o$.

Figure 8-2. Simulation results: The time history of electric to magnetic field energy density ratio and magnetic field energy density.

Figure 8-3. Simulation results: The time development of the dispersion relation for δE_y propagating in the direction of $\mathbf{B}_0$. (a) $50 \leq \omega_e t \leq 100$, (b) $100 \leq \omega_e t \leq 150$, (c) $150 \leq \omega_e t \leq 200$, (d) $250 \leq \omega_e t \leq 300$.

Figure 8-4. Simulation results: The dispersion relation of electromagnetic components δB_x and δB_z. (a) δB_x ,$250 \leq \omega_e t \leq 300$, (b) δB_z ,$250 \leq \omega_e t \leq 300$.

Figure 8-5. Simulation results: The polarization of electromagnetic component δB_x and δB_z from data at (a) $x = 9\Delta$, $y = 500\Delta$ (b) $x = 9\Delta$, $y = 600\Delta$. These are both Langmuir-like fluctuation with long wavelength, $-0.3 \leq kc/\omega_e \leq 0.3$.

Figure 8-6. Simulation results: The time history of statistics about the right-hand polarization of electromagnetic components δB_x and δB_z. (a) is percentage of right-hand polarization at short wavelength, $-0.3 \leq kc/\omega_e \leq 0.3$ and (b) is percentage of right-hand polarization at long wavelength, $1.4 \leq kc/\omega_e \leq 1.9$

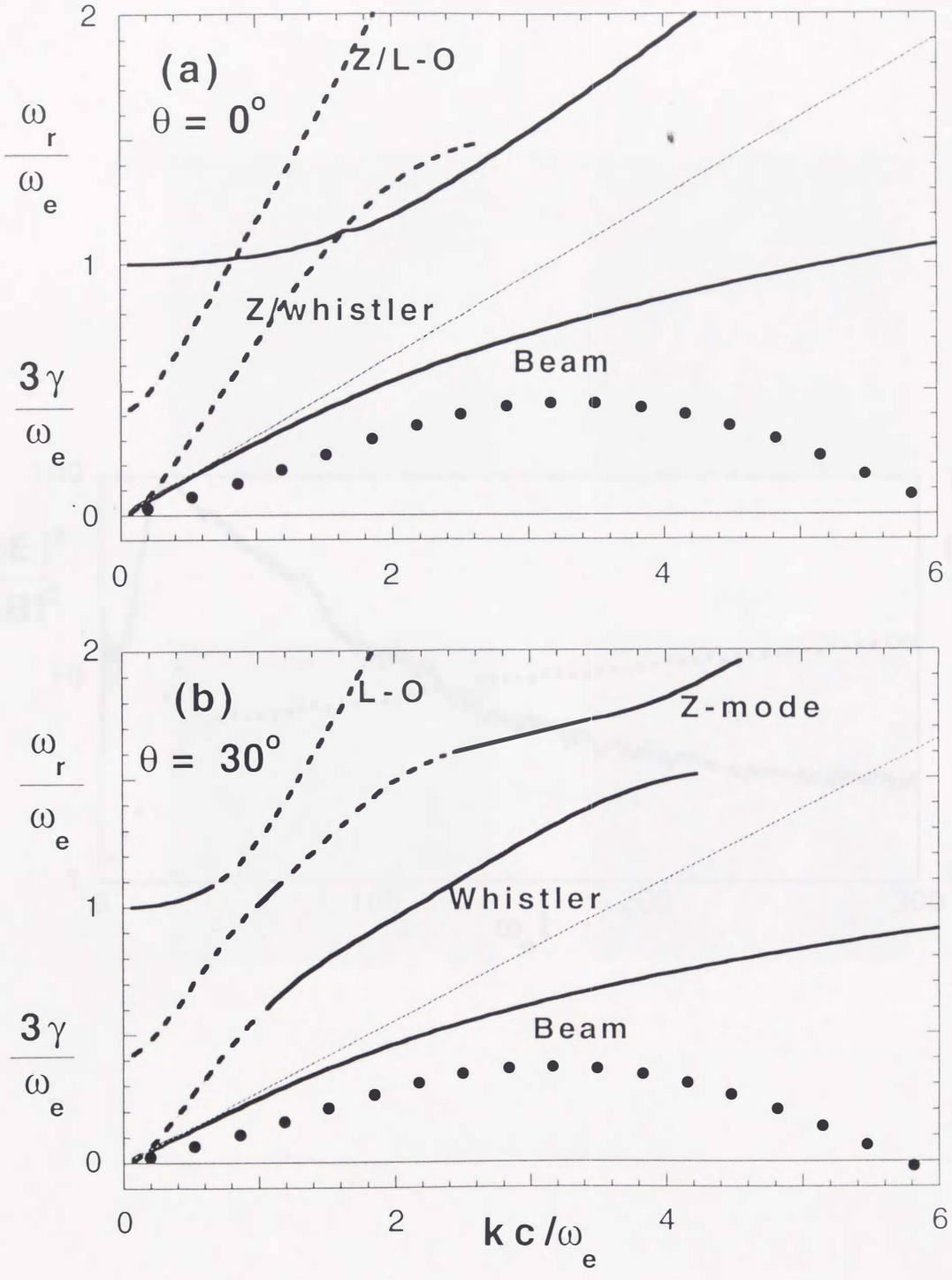
(a)
θ = 0°
Z/L-O
Z/whistler
Beam
(b)
θ = 30°
L-O
Z-mode
Whistler
Beam
ω_r / ω_e
3γ / ω_e
kc/ω_e
0
1
2
4
6

Figure 8-1

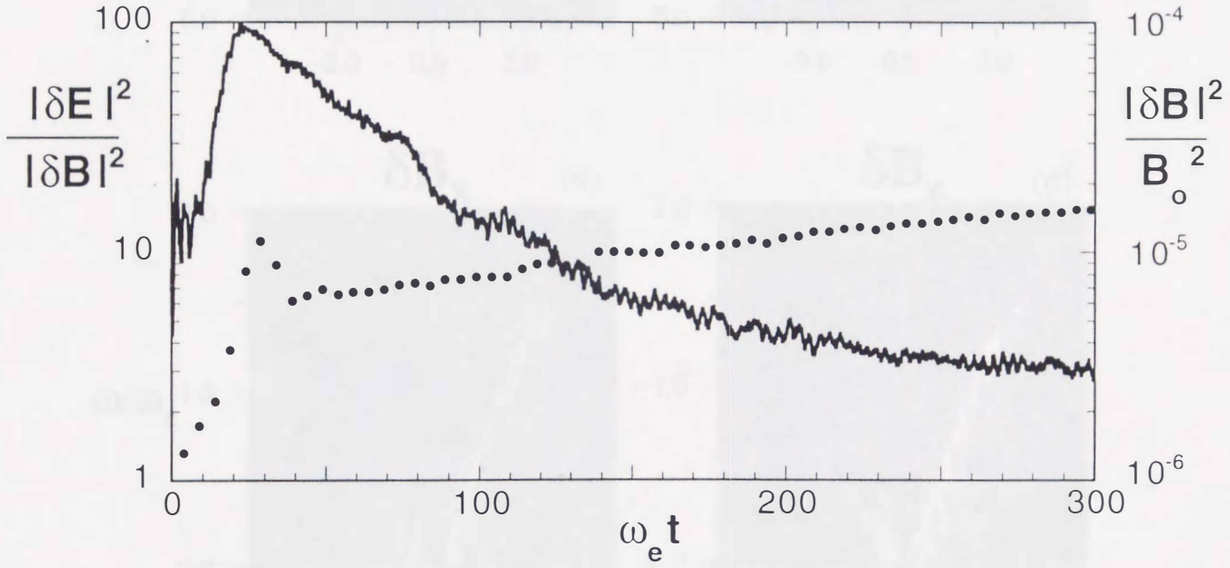
100
10
1
$\frac{|\delta E|^2}{|\delta B|^2}$
0
100
200
300
$\omega_e t$
10^{-4}
10^{-5}
10^{-6}
$\frac{|\delta B|^2}{B_o^2}$

Figure 8-2

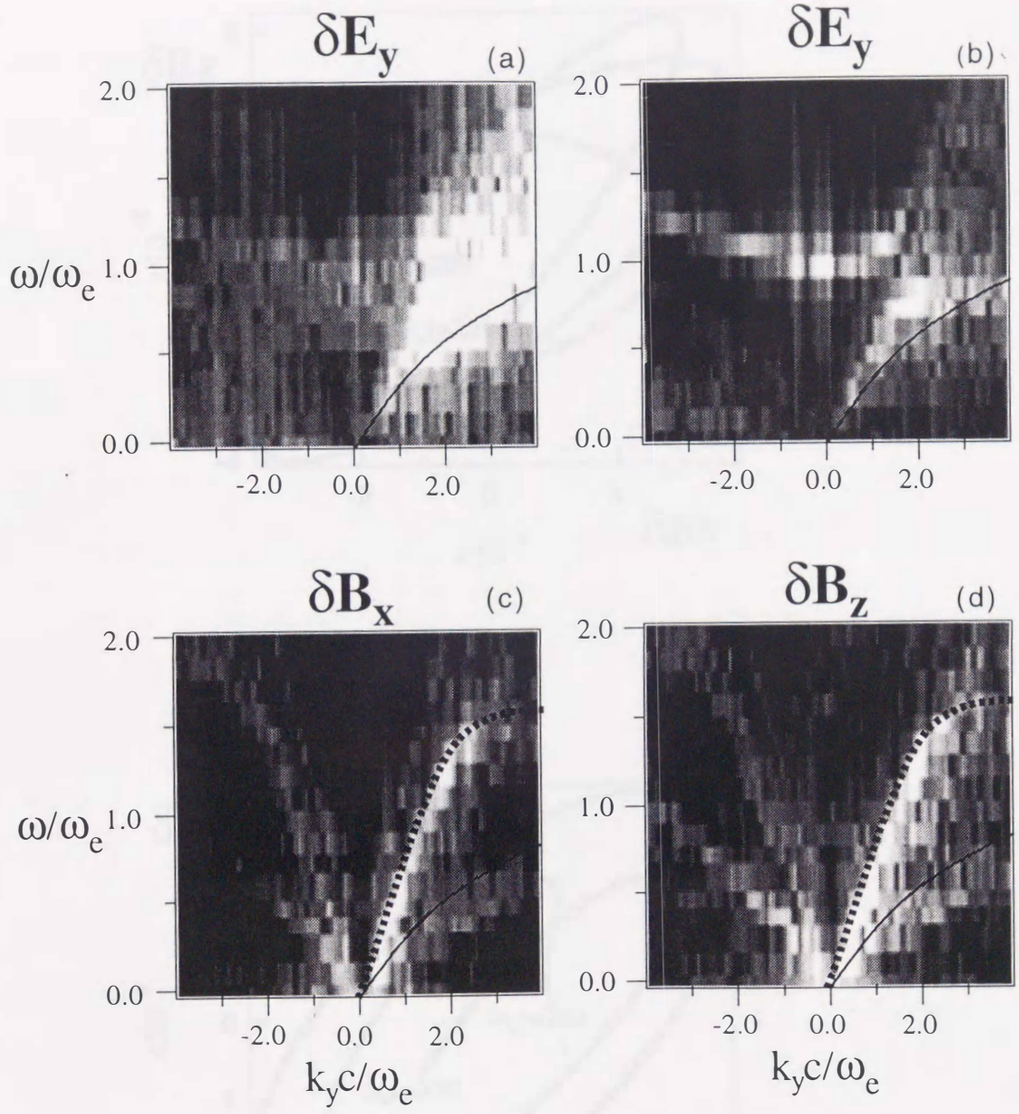

Figure 8-3 ,8-4

(a)

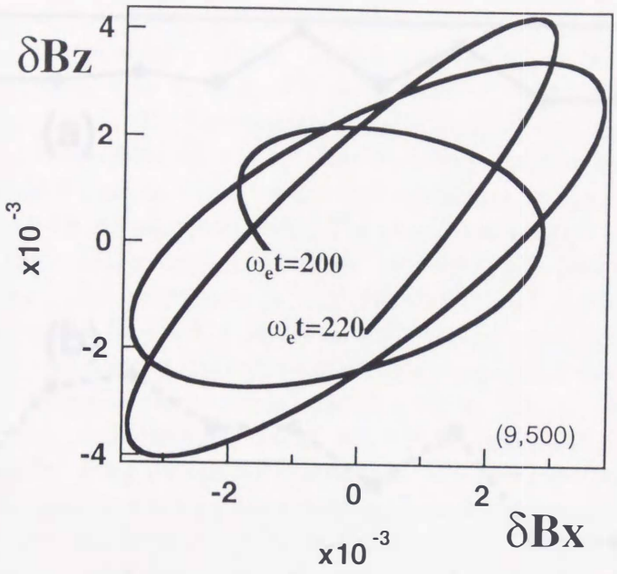
δBz
4
2
0
-2
-4
x10^-3
ω_e t=200
ω_e t=220
(9,500)
-2
0
2
x10^-3
δBx

(b)

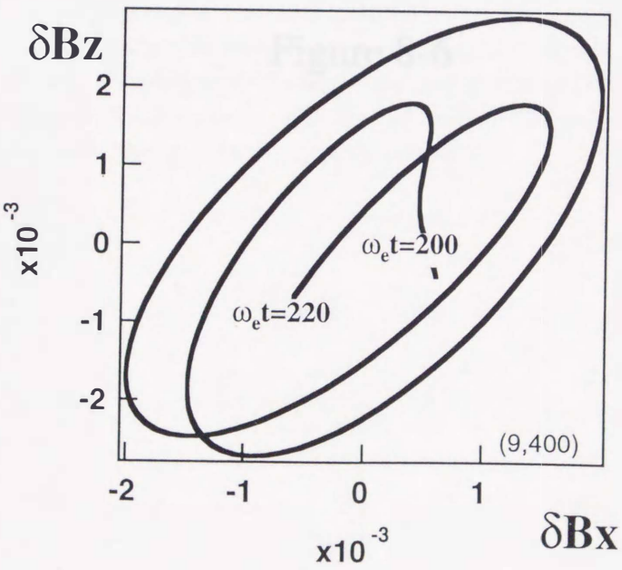
δBz
2
1
0
-1
-2
x10^-3
ω_e t=200
ω_e t=220
(9,400)
-2
-1
0
1
x10^-3
δBx

Figure 8-5

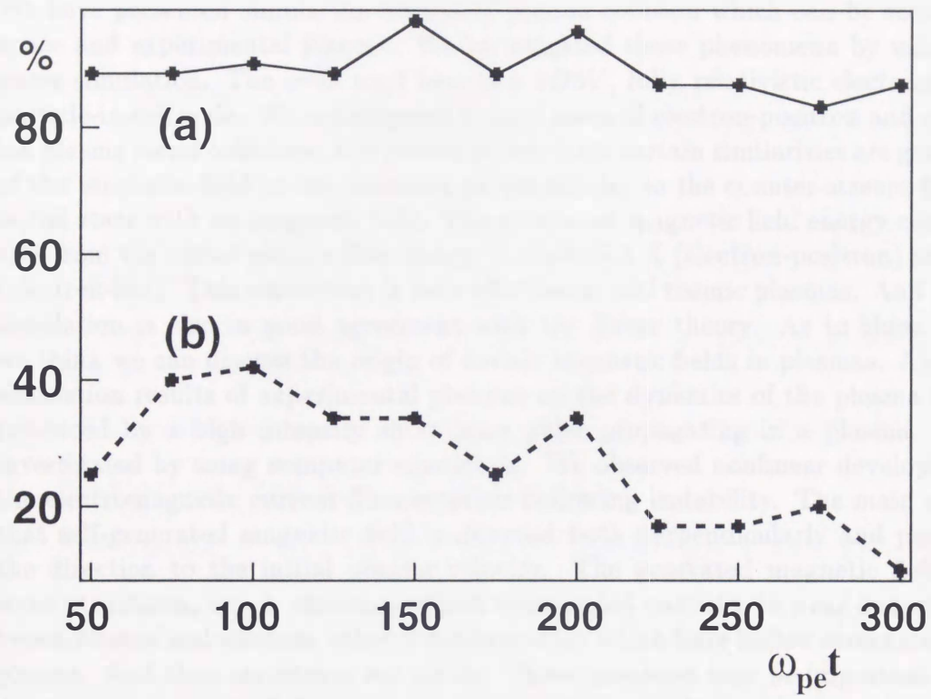

Figure 8-6

Summary

We have presented simulation results of plasma collision which can be seen in real space and experimental plasma. We investigated those phenomena by using computer simulation. The code used here is a $2D3V$, fully relativistic electromagnetic particle-in-cell code. We investigated several cases of electron-positron and election-ion plasma cloud collisions, and results which share certain similarities are generation of the magnetic field in the direction perpendicular to the counter-stream from the initial state with no-magnetic field. The generated magnetic field energy conversion rate from the initial plasma flow energy is about 5.3 % (electron-positron) and 3.7% (electron-ion). This conversion is very effective in real cosmic plasmas. And particle simulation is also in good agreement with the linear theory. As to these results, we think we can discuss the origin of cosmic magnetic fields in plasmas. About the simulation results of experimental plasmas on the dynamics of the plasma channel produced by a high intensity short laser pulse propagating in a plasma, we also investigated by using computer simulation. We observed nonlinear development of the electromagnetic current filamentation-hollowing instability. The main result is that self-generated magnetic field is directed both perpendicularly and parallel to the direction to the initial plasma velocity. The generated magnetic fields have some structures, one is structure which surrounded particles in near boundary between plasma and vacuum, other is configuration which have hollow structures inside plasma. And their structures are stable. These processes may be important for understanding magnetic field generation in plasmas interacting with strong laser pulses and the magnetic confinement in fusion plasma when a laser pulse heats a target. And I think these results are also helpful to realize the direct drive implosion by Laser pulse. Computer simulation, it makes great progress going with development of CPU efficiency and speed. I think computer simulation is useful in point of its costs and speed and accuracy. Because of these reasons, it will be a main style of development and research and study in the future.

References

[1] W.Becker, J.Trumper, S. C.Lundgren, J. M.Cordes, and A. F.Zepka *M. N. R. A. S.*, L33 (1996) 282.

[2] D. R.Lorimer, A. G.Lyne, M.Bailes, R.N.Manchester, N.D'Amico, B. W.Stappers, S.Johnston,and F.Camilo, *M. N. R. A. S.*,L1383 (1996) 283.

[3] E.W.Weibel, *Phys. Rev. Lett.*, 2 (1959) 83.

[4] G. A.Askar'yan,S. V. Bulanov, F.Pegoraro, A. M.Pukhov, *JETP Lett.* **60** (1994) 240.

[5] S. V.Bulanov, M.Lontano, Zh.T.Esirkepov, F.Pegoraro, A.M.Pukhov,*Phys. Rev. Lett.* **76** (1996) 3562.

[6] F.Califano, F.Pegoraro, & S.V.Bulanov, *Phys. Rev. E* 56 (1997) 963.

[7] P.P.Kronberg: Rep. Prog. Phys. (1994) 325.

[8] R.M.Kulsrud, R. Cen, J.P. Ostriker, and D.Ryu: Ap. J. **480** (1997) 481.

[9] Y. Kazimura, J. I. Sakai, T. Neubert and S. V. Bulanov: J. Phys. Soc. Japan, **67** (1998) 1079.

[10] M.D.Perry, and G.Mourou G.: Science **264** (1994) 917.

[11] V.S.Berezinskij, S.V.Bulanov, V.A.Dogiel, V.L.Ginzburg, and V.S.Ptuskin: *Astrophysics of Cosmic Rays* (North Holland Publ. Co., Elsevier Sci. Publ., Amsterdam, 1990).

[12] T.Tajima:*Experimental Plasma Astrophysics Using a T^3 (Table-Top Terawatt) Laser*, (IFSR# 765, 1996).

[13] G.A.Askar'yan, S.V.Bulanov, F.Pegoraro, and A.M.Pukhov: JETP Lett. **60** (1994) 294.

[14] F.Califano, R.Prandi, F.Pegoraro, S.V.Bulanov: Journal of Plasma Physics (1998) in press.

[15] F.Califano, F.Pegoraro, S.V.Bulanov, and A.Mangeney: Phys.Rev. E (1997) submitted;

[16] O.Buneman, 1993, in *Computer Space Plasma Physics, Simulation Techniques and Software*, (edited by H. Matsumoto & Y. Omura, Terra Scientific, Tokyo), p.67.

[17] S.V.Bulanov, M.Lontano, Esirkepov, Zh.T., F.Pegoraro, and A.M.Pukhov: Phys. Rev. Lett. **76** (1996) 3562.

[18] S.V.Bulanov, T.Zh.Esirkepov, M.Lontano, F.Pegoraro: Plasma Physics Reports **23** (1997) 660.

[19] S.V.Bulanov, F.Pegoraro, A.M.Pukhov, A.S.Sakharov: Phys. Rev. Lett. **78** (1997) 4205.

[20] J. F. Drake, R. G. Kleva and M. E. Mandt: Phys. Rev. Lett. **73** (1994) 1251.

[21] K. J. Reitzel and G. J. Morales: Phys. Plasmas **5** No. 11 (1998) 3806.

[22] A. I. Eriksson, B. Holback, P. O. Dover, R. Bostrom, G. Holmgren, M. Andre, L. Eliasson and P.M. Kintner: Geophys. Res. Lett. **21** (1994) 1843.

[23] Y. Kazimura, J. I. Sakai, T. Neubert and S. V. Bulanov: Ap. J. Lett. **498** (1998) L183;

[24] Y. Kazimura, J. I. Sakai, T. Neubert and S. V. Bulanov: J. Phys. Soc. Japan, **67** (1998) 1079.

[25] T. Haruki, J. I. Sakai, T. Neubert and M. Nambu : 9th International Toki Conference, Dec. 8-11, 1998, Toki city, Japan, JPFR Series Vol. 2, (1999) in press.

[26] Miller, R.B., *Intense Charged Particle Beams* (Plenum, New York, 1982).

[27] Lawson, J.D., *The Physics of Charged Particle Beams* (Clarendon Press, Oxford, 1988).

[28] Davidson,R., *Physics of Nonneutral Plasmas* (Addison-Wesley Publ. Co., New York, 1990).

[29] Tajima,T.and Shibata,K., *Plasma Astrophysics* (Addison-Wesley Reding, Massachussets, 1997)

[30] G. A. Mourou, C. P. J. Barty, and D. Perry, Phys. Today **51**, N1, 22 (1998).

[31] Korobkin, V.V. & Serov, R.V. *JETP Lett.* **4**, 70-72 (1962); Forslund, D.W., Kindel, J.M., Mori, W.B., Joshi,C. & Dawson, J.M. *Phys. Rev. Lett.* **54**, 558-561 (1985); Wilks, S.C., Kruer, W.C., Tabak, M. & Langdon, A.B. *Phys. Rev. Lett.* **69**, 1383-1386 (1992); M. Borghesi, A. J. MacKinnon, L. Barringer, R. Gaillard, L. A. Gizzi, C. Meyer, O. Willi, A. Pukhov, and J. Meyer-ter-Vehn, Phys. Rev. Lett. **78**, 879 (1997).

[32] Bell, A. R., *Phys. Plasmas*, **1**, 1643 (1994).

[33] Sarkisov, G. S., V. Yu. Bychenkov, V. N. Novikov, V. T. Tikhonchuk, A. Maksimchuk, S. Y. Chen, R. Wagner, G. Mourou, and D. Umstadter, Phys. Rev. E, accepted for publication.

[34] V. Yu. Bychenkov, *et al.*, Sov. Phys. JETP **71**, 79 (1990); F. Pegoraro, S. V. Bulanov, F. Califano, and M. Lontano, Physica Scripta **T63**, 262 (1996); F. Califano, F. Pegoraro, S. V. Bulanov, A. Mangeney, *Phys. Rev. E* **57**, 7048 (1998); F. Califano, R.Prandi, F. Pegoraro, S. V. Bulanov, *Phys. Rev. E* **58**, 7837 (1998); Y. Kazimura, J.I. Sakai, T. Neubert, and S.V. Bulanov, Ap. J. (Letter) **498**, L183 (1998); Y. Kazimura, F. Califano, J.I. Sakai, T. Neubert, F. Pegoraro, and S.V. Bulanov, J. Phys. Soc. Japan, Vol.67 , No.4, 1079 (1998).

[35] Calvert, W., The auroral plasma cavity, *Geophys. Res. Lett.*, *8*, 919, 1981.

[36] Cairns, I. H., and J. D. Menietti, Radiation near $2f_p$ and intensified emissions near f_p in the dayside and nightside auroral region and polar cap, *J. Geophys. Res.*, *102*, 4787, 1997.

[37] Cairns, I. H., Measurement of the plasma density using the intensification of z-mode waves at the electron plasma frequency, *Phys. Rev. Lett.*, *82*, 564, 1999.

[38] Menietti, J. D., I. H. Cairns, C. W. Piker, and T. F. Averkamp, Statistical study of emissions near f_p and $2f_p$ in the dayside and nightside auroral region and polar cap, *J. Geophys. Res.*, *103*, 14,925, 1998.

[39] Gary, S. P., and I. H. Cairns, Electron temperature anisotropy instabilities: Whistler, electrostatic, and z-mode, *J. Geophys. Res.*, *104*, 19,835, 1999.

[40] Yin, L., M. Ashour-Abdalla, M. El-Alaoui, J. M. Bosqued, and J. L. Bougeret, Plasma waves in the Earth's electron foreshock: 2. Simulations using time-of-flight electron distributions in a generalized Lorentzian plasma, *J. Geophys. Res.*, *103*, 29,619, 1998.

[41] Winglee, R. M., J. D. Menietti, and H. K. Wong, Numerical simulations of bursty radio emissions from planetary magnetospheres, *J. Geophys. Res.*, *97*, 17,131, 1992.

[42] Gary, S. P., *Theory of Space Plasma Microinstabilities*, Cambridge Univ. Press, New York, 1993.

[43] Gary, S. P., Y. Kazimura, H. Li, and J.-I. Sakai, Simulations of electron/electron instabilities: Electromagnetic fluctuations, *Phys. Plasmas*, submitted, 1999.

[44] Nambu, M., B. J. Saikia, D. Gyobu, and J. I. Sakai, Nonlinear plasma maser driven by electron beam instability, *Phys. Plasmas*, *6*, 994, 1999.

[45] Newman, D. L., R. M. Winglee, and M. V. Goldman, Theory and simulation of electromagnetic beam modes and whistlers, *Phys. Fluids*, *31*, 1515, 1988.

Acknowledgments

I greatly appreciate the thoughtful comments and suggestions of Dr. Jun-ichi Sakai ,Dr. Shinji Koide, Dr. S. V. Bulanov, Dr. F. Califano, Dr. F. Pegoraro. I also appreciate to Dr. S. Peter Gary and Dr. Fui-li. They and I collaborated in writing papers in Los Alamos National Laboratory New Mexico for three months. (July 1999-Sep 1999) And Prof.Nambu is acknowledged for useful comments on this thesis. In my PAFS life for four years, all the members who I met and collaborated in PAFS laboratory (D. Gyobu, T.Haruki, T. Nakayama, D. Sugiyama, H. Mae, K. Furusawa) were very kind and friendly, they made me cheer and happy. I give all credit to them for my success. Specially,I would like to thank my supervisor, Prof.J.I.Sakai. His advice and comment has been helpful and important for me. I want to make an efforts for the purpose of his kindness is not wasted upon me. Thanks. (Feb 28, 2000)

1 Appendix 1

We derive the dispersion relation of electron-positron counterstreaming by the following method.

The basic equations of electron-positron two counter-streamings are described by the following equations.Here and below $\mathbf{v}_{ea}$ are the electron velocities, $e =$ denotes electrons and $a = 1, 2$ are the two counterstreaming components.

$$\frac{\partial \mathbf{P}_{ea}}{\partial t} = -\mathbf{v}_{ea} \cdot \nabla \mathbf{P}_{ea} - (\mathbf{E} + \mathbf{v}_{ea} \times \mathbf{B}), \tag{1}$$

$$\frac{\partial \mathbf{P}_{pa}}{\partial t} = -\mathbf{v}_{pa} \cdot \nabla \mathbf{P}_{pa} + (\mathbf{E} + \mathbf{v}_{pa} \times \mathbf{B}), \tag{2}$$

$$\frac{\partial (n_{pa} - n_{ea})}{\partial t} + \nabla \cdot (n_{pa}\mathbf{v}_{pa} - n_{ea}\mathbf{v}_{ea}) = 0, \tag{3}$$

$$\frac{\partial \mathbf{B}}{\partial t} = -\nabla \times \mathbf{E}, \tag{4}$$

$$\frac{\partial \mathbf{E}}{\partial t} = \nabla \times \mathbf{B} - \sum_a (\mathbf{J}_{pa} + \mathbf{J}_{ea}), \tag{5}$$

$$\nabla \cdot \mathbf{E} = \sum_a (n_{pa} - n_{ea}), \tag{6}$$

$$\mathbf{v}_{ea} = \frac{\mathbf{P}_{ea}}{(1 + \mathbf{P}_{ea}{}^2)^{\frac{1}{2}}}, \tag{7}$$

$$\mathbf{v}_{pa} = \frac{\mathbf{P}_{pa}}{(1 + \mathbf{P}_{pa}{}^2)^{\frac{1}{2}}}, \tag{8}$$

$$\mathbf{J}_{ea} = -n_{ea}\mathbf{v}_{ea}, \tag{9}$$

$$\mathbf{J}_{pa} = n_{pa}\mathbf{v}_{pa}. \tag{10}$$

By inserting $\mathbf{v} = \mathbf{v}_0 + \mathbf{v}_1$ into equations(7) or (8) and linearizing, we find

$$\mathbf{v}_0 + \mathbf{v}_1 = \frac{\mathbf{P}_0 + \mathbf{P}_1}{(1 + (\mathbf{P}_0 + \mathbf{P}_1)^2)^{\frac{1}{2}}}, \tag{11}$$

$$\begin{aligned} \mathbf{v}_1 &= \frac{\mathbf{P}_1}{(1 + \mathbf{P}_0^2)^{\frac{1}{2}}} - \frac{\mathbf{P}_0^2 \cdot \mathbf{P}_1}{(1 + \mathbf{P}_0^2)^{\frac{3}{2}}}, \\ &= \frac{\mathbf{P}_1}{(1 + \mathbf{P}_0^2)^{\frac{1}{2}}} - \mathbf{v}_0 \frac{\mathbf{P}_0 \cdot \mathbf{P}_1}{1 + \mathbf{P}_0^2}, \\ &= \frac{\mathbf{P}_1}{(1 + \mathbf{P}_0^2)^{\frac{1}{2}}} - \mathbf{v}_0 \frac{\mathbf{v}_0^2}{\mathbf{P}_0^2}(\mathbf{P}_0 \cdot \mathbf{P}_1). \end{aligned} \tag{12}$$

As the initial flow velocity v_x is in x direction, we get

$$\mathbf{v}_{1x} = \frac{P_1}{(1+(P_0)^2)^{\frac{1}{2}}} - v_{0x}\frac{v_{0x}^2}{P_0}P_{1x}, \tag{13}$$

$$= \frac{v_0}{P_0}P_{1x} - \frac{v_0}{P_0}v_{0x}^2 P_{1x},$$

$$= \frac{v_0}{P_0}P_{1x}(1-v_{0x}^2),$$

$$= \frac{v_0}{v_0\Gamma}P_{1x}\frac{1}{\Gamma^2},$$

$$= \frac{P_{1x}}{\Gamma^3}$$

where $\Gamma = (1-v_0^2)^{-1/2}$.

We obtain the following relations,

$$P_{1x} = \Gamma^3 v_x, \tag{14}$$

$$P_{1y} = \Gamma v_y, \tag{15}$$

$$P_{1z} = \Gamma v_y. \tag{16}$$

The next we linearize equations of motion and expand as Fourier components,

$$\frac{\partial \mathbf{P}_{1a}}{\partial t} = -\mathbf{v}_{0a}\cdot\nabla\mathbf{P}_{1a} - (\mathbf{E_1} + \mathbf{v}_{0a}\times\mathbf{B_1}), \tag{17}$$

$$-i\omega\mathbf{P}_{1a} = -\mathbf{v}_{0a}ik_x\mathbf{P}_{1a} - \mathbf{E_1} - \mathbf{v}_{0a}\times\mathbf{B_1}. \tag{18}$$

Here,B is given from the induction equation,

$$\frac{\partial \mathbf{B}}{\partial t} = -\nabla\times\mathbf{E}, \tag{19}$$

$$-i\omega\mathbf{B_1} = -i\mathbf{K}\times\mathbf{E_1}, \tag{20}$$

$$= -i(k_yE_z, -k_xE_z, k_xE_y - k_yE_x), \tag{21}$$

$$\mathbf{B_1} = \frac{1}{\omega}(k_yE_z, -k_xE_z, k_xE_y - k_yE_x). \tag{22}$$

Hence the equation(24) is written as follows.

$$-i\omega\mathbf{P}_{1a} = -\mathbf{v}_{0a}ik_x\mathbf{P}_{1a} - \mathbf{E_1} - (v_{0a},0,0)\times\mathbf{B_1}, \tag{23}$$

$$-i\omega\mathbf{P}_{1a} = -\mathbf{v}_{0a}ik_x\mathbf{P}_{1a} - \mathbf{E_1} - (0, -\frac{v_0}{\omega}(k_xE_y - k_yE_x), -\frac{v_0k_x}{\omega}E_z). \tag{24}$$

And each x,y,z component is

$$-i\omega P_{1x} = -v_{0a}ik_xP_{1x} - E_x, \tag{25}$$

$$-i\omega P_{1y} = -v_{0a} i k_x P_{1y} - E_y + \frac{v_0}{\omega}(k_x E_y - k_y E_x), \tag{26}$$

$$-i\omega P_{1z} = -v_{0a} i k_x P_{1z} - E_z + \frac{v_0 k_x}{\omega} E_z. \tag{27}$$

And,

$$-i\Omega P_{1x} = -E_x, \tag{28}$$

$$-i\Omega P_{1y} = -\frac{1}{\omega}(k_y v_{0a} E_x + \Omega_a E_y), \tag{29}$$

$$-i\Omega P_{1z} = -(\frac{\Omega_a}{\omega}) E_z, \tag{30}$$

where $\Omega_a = \omega - k_x v_{0,a}$. Here equation (28)-(30) are written as follows by using equations (14)-(16).

$$v_{1ex} = -\frac{1}{i\Omega_{ea}\Gamma^3} E_x, \tag{31}$$

$$v_{1ey} = -\frac{1}{i\Omega_{ea}\Gamma}(E_x k_y v_{0ea} + \Omega_{ea} E_y), \tag{32}$$

$$v_{1ez} = -\frac{1}{i\Omega_{ea}\Gamma}(\frac{\Omega_{ea}}{\omega}) E_z. \tag{33}$$

The next we use the equation(2) in positron cases.

$$\frac{\partial \mathbf{P}_{pa}}{\partial t} = -\mathbf{v}_{pa} \cdot \nabla \mathbf{P}_{pa} + (\mathbf{E} + \mathbf{v}_{pa} \times \mathbf{B}). \tag{34}$$

And,

$$v_{1px} = -\frac{1}{i\Omega_{pa}\Gamma^3} E_x, \tag{35}$$

$$v_{1py} = -\frac{1}{i\Omega_{pa}\Gamma}(E_x k_y v_{0pa} + \Omega_{pa} E_y), \tag{36}$$

$$v_{1pz} = -\frac{1}{i\Omega_{pa}\Gamma}(\frac{\Omega_{pa}}{\omega}) E_z. \tag{37}$$

From the continuity equation and $v_{ia} = (v_{0ea} + v_{1xa}, v_{1ya}, v_{1za})$, we find

$$\frac{\partial(n_{pa} - n_{ea})}{\partial t} - \mathbf{div}(n_{0pa} v_{1pxa} + n_{1pa} v_{0pa}, n_{0pa} v_{1pya}, n_{0pa} v_{1pza}) = 0, \tag{38}$$

By using the condition, $v = v_{0p} = v_{0e}$, and Fourier expansion of equation (40),we obtain

$$\Omega(n_{p1} - n_{e1}) = n_{0pa}(k_x v_{1px} + k_y v_{1py}) - n_{0pa}(k_x v_{1ex} + k_y v_{1ey}). \tag{39}$$

From the Maxwell's equations,

$$\frac{\partial \mathbf{E}}{\partial t} = \nabla \times \mathbf{B} - \sum_a (\mathbf{J}_{pa} + \mathbf{J}_{ea}), \tag{40}$$

we get by differentatiry it by t,

$$\frac{\partial^2 \mathbf{E}}{\partial t^2} = \nabla \times \frac{\partial \mathbf{B}}{\partial t} - \sum_{i,a} \frac{\partial \mathbf{J}_{ia}}{\partial t}, \tag{41}$$

$$= \nabla \times (-\nabla \times \mathbf{E}) - \sum_{i,a} \frac{\partial \mathbf{J}_{ia}}{\partial t},$$

$$= -(grad\mathbf{div}\mathbf{E} - \Delta \mathbf{E}) - \sum_{i,a} \frac{\partial \mathbf{J}_{ia}}{\partial t},$$

$$(-i\omega)^2 \mathbf{E} = -(ik_x, ik_y, 0)(ik_x, ik_y, 0)\mathbf{E} + ((ik_x)^2 + (ik_y)^2)\mathbf{E} - \sum_{i,a} \frac{\partial \mathbf{J}_{ia}}{\partial t}, \tag{42}$$

$$\omega^2 \mathbf{E} = ({k_x}^2 E_x - k_x k_y E_y, -k_x k_y E_x - {k_y}^2 E_y, 0) - (-{k_x}^2 - {k_y}^2, -{k_x}^2 - {k_y}^2, -{k_x}^2 - {k_y}^2)\mathbf{E} + \sum_{i,a} \frac{\partial \mathbf{J}_{ia}}{\partial t}, \tag{43}$$

And each E_x, E_y, E_y component is

$$-\omega^2 E_x = ({k_x}^2 - {k_x}^2 - {k_y}^2) + k_x k_y E_y - \sum_{i,a} \frac{\partial J_x}{\partial t} \tag{44}$$

$$-\omega^2 E_y = k_x k_y E_x + {k_y}^2 E_y - {k_x}^2 E_y - {k_y}^2 E_y - \sum_{i,a} \frac{\partial J_y}{\partial t} \tag{45}$$

$$-\omega^2 E_z = (-{k_x}^2 - {k_y}^2) E_z - \sum_{i,a} \frac{\partial J_z}{\partial t} \tag{46}$$

Hence,

$$(\omega^2 - {k_y}^2) E_x + k_x k_y E_y - \sum_{i,a} \frac{\partial J_x}{\partial t} \tag{47}$$

$$k_x k_y E_x + (\omega^2 - {k_x}^2) E_y - \sum_{i,a} \frac{\partial J_y}{\partial t} \tag{48}$$

$$(\omega^2 - {k_x}^2 - {k_y}^2) E_z - \sum_{i,a} \frac{\partial J_z}{\partial t} \tag{49}$$

Here $\sum_{i,a} \frac{\partial \mathbf{J}_{ia}}{\partial t}$ is derived as follows, We use the relation of $\mathbf{J} = -(n_p \mathbf{v}_p - n_e \mathbf{v}_e)$. At first, x-component is

$$J_x = (n_{0pa} v_{1pax} + n_{1pa} v_{0pa} - n_{0ea} v_{1eax} - n_{1ea} v_{0ea}). \tag{50}$$

Here we use the relation $v_{0a} = v_{0e} = v$,and substitute the equation (39), then J_x become

$$J_x = -(1 + \frac{k_x}{\Omega} v)(n_{0p} v_{1px} - n_{0e} v_{1ex}) + \frac{k_y}{\Omega} v (n_{0a} v_{1py} - n_{0ea} v_{1ey}). \tag{51}$$

By using the (31),(32),(33),it is rewritten as

$$J_x = (n_{0p} + n_{0e})\frac{E_x}{i\Omega\Gamma^3} + (n_{0p} + n_{0e})\frac{vk_xE_x}{i\Omega^2\Gamma^3} + (n_{0p} + n_{0e})\frac{v^2{k_y}^2E_x}{i\omega\Omega^2\Gamma} + (n_{0p} + n_{0e})\frac{vk_yE_y}{i\omega\Omega\Gamma}. \quad (52)$$

And,after differentity t and summing up for each species, we get

$$-\sum_{i,a}\frac{\partial J_x}{\partial t} = (\sum(n_{0p}+n_{0e})\frac{\omega}{\Omega\Gamma^3}+\sum(n_{0p}+n_{0e})\frac{vk_x\omega}{\Omega^2\Gamma^3}+\sum(n_{0p}+n_{0e})\frac{v^2{k_y}^2}{\Omega^2\Gamma})E_x+\sum(n_{0p}+n_{0e})\frac{vk_y}{\Omega\Gamma}E_y. \quad (53)$$

Substituting this equation(53) to (47), we find

$$[\omega^2(1-\Omega_{2p}^{-2}-\Omega_{2e}^{-2})-{k_y}^2(1+\Omega_{4p}^{-2}+\Omega_{4e}^{-2})]E_x+[k_xk_y-(\Omega_{3p}^{-2}+\Omega_{3e}^{-2})\Omega k_y]E_y=0 \quad (54)$$

And similarly,

$$J_y = -(n_{0pa}v_{1pay} - n_{0ea}v_{1eay}) \quad (55)$$

$$-\sum\frac{\partial J_y}{\partial t} = \sum(n_{0p}+n_{0e})\frac{k_yv}{\Omega\Gamma}E_x + \sum(n_{0p}+n_{0e})\frac{E_y}{\Gamma} \quad (56)$$

$$[k_xk_y-(\Omega_{3p}^{-2}+\Omega_{3e}^{-2})\Omega k_y]E_x+[\omega^2(1-\Omega_{1p}^{-2}-\Omega_{1e}^{-2})-{k_x}^2(1+\Omega_{4p}^{-2}+\Omega_{4e}^{-2})+2(\Omega_{3p}^{-2}+\Omega_{3e}^{-2})\omega k_x]E_y=0 \quad (57)$$

And z component is,

$$J_z = -(n_{0pa}v_{1paz} - n_{0ea}v_{1eaz}) \quad (58)$$

$$[\omega^2(1-\Omega_{1p}^{-2}-\Omega_{1e}^{-2})-{k_x}^2(1+\Omega_{4p}^{-2}+\Omega_{4e}^{-2})-{k_y}^2+2(\Omega_{3p}^{-2}+\Omega_{3e}^{-2})\omega k_x]E_z=0 \quad (59)$$

where,

$$\Omega_{1e}^{-2}=\sum_a\frac{n_{0,ea}}{\Gamma_{ea}\Omega_{ea}^2},\quad \Omega_{2e}^{-2}=\sum_a\frac{n_{0,ea}}{\Gamma_{ea}^3\Omega_{ea}^2},\quad \Omega_{3e}^{-2}=\sum_a\frac{n_{0,ea}v_{0,ea}}{\Gamma_{ea}\Omega_{ea}^2},\quad \Omega_{4e}^{-2}=\sum_a\frac{n_{0,ae}v_{0,ae}^2}{\Gamma_{ae}\Omega_{ae}^2},$$

$$\Omega_{1p}^{-2}=\sum_a\frac{n_{0,pa}}{\Gamma_{pa}\Omega_{pa}^2},\quad \Omega_{2p}^{-2}=\sum_a\frac{n_{0,pa}}{\Gamma_{pa}^3\Omega_{pa}^2},\quad \Omega_{3p}^{-2}=\sum_a\frac{n_{0,pa}v_{0,pa}}{\Gamma_{pa}\Omega_{pa}^2},\quad \Omega_{4p}^{-2}=\sum_a\frac{n_{0,pa}v_{0,pa}^2}{\Gamma_{pa}\Omega_{pa}^2},$$

$$a=1,2.$$

Here the following notations are used:

$$\Omega_{pa}=\omega-k_yv_{0,pa},\qquad \Gamma_{pa}=(1-v_{0,pa}^2)^{-1/2},$$

$$\Omega_{ea}=\omega-k_yv_{0,ea},\qquad \Gamma_{ea}=(1-v_{0,ea}^2)^{-1/2},$$

$$a=1,2.$$

Here the equations (54),(57),(59) are summarized as follow,

$$\begin{cases} AE_x+BE_y+0E_z=0 \\ CE_x+DE_y+0E_z=0 \\ 0E_x+0E_y+FE_z=0 \end{cases}$$

Hence,

$$\epsilon(\omega,k)\cdot\mathrm{E}=0. \quad (60)$$

From the condition of $E \neq 0$ we finally find the dispersion equation

$$det\ \epsilon(\omega, k) = 0, \tag{61}$$

$$F(AD - BC) = 0. \tag{62}$$

Then we obtain the following dispersion equation:

$$(1 - \Omega_{2p}^{-2} - \Omega_{2e}^{-2})\{(1 + \Omega_{4p}^{-2} + \Omega_{4e}^{-2})k_y^2 - \omega^2(1 - \Omega_{1p}^{-2} - \Omega_{1e}^{-2}) - 2\omega k_y(\Omega_{3p}^{-2} + \Omega_{3e}^{-2})\}$$

$$+k_x^2\{(1 + \Omega_{4p}^{-2} + \Omega_{4e}^{-2})(1 - \Omega_{1p}^{-2} - \Omega_{1e}^{-2}) + (\Omega_{3p}^{-2} + \Omega_{3e}^{-2})^2\} = 0. \tag{63}$$

2 Appendix 2

We show here the calculation method of linear growth rate of magnetic field.

$$B_z = B_0 e^{\gamma t}. \tag{64}$$

where γ is growth rate of magnetic field B_z,and t, γ normalized by ω_{pe}.

$$B_z = B_0 e^{\frac{\gamma}{\omega_{pe}} t\omega_{pe}}. \tag{65}$$

The magnetic field energy is

$$B_z{}^2 = B_0^2 e^{2\gamma t}. \tag{66}$$

And at time t_1, t_2,magnetic field energy is

$$B_z{}^2(t_1) = B_0^2 e^{2\gamma t_1}. \tag{67}$$

$$B_z{}^2(t_2) = B_0^2 e^{2\gamma t_2}. \tag{68}$$

Then,

$$\frac{B_z{}^2(t_1)}{B_z{}^2(t_2)} = e^{2\gamma(t_1 - t_2)}. \tag{69}$$

$$log(\frac{B_z{}^2(t_1)}{B_z{}^2(t_2)}) = log(e^{2\gamma(t_1 - t_2)}). \tag{70}$$

$$= 2\gamma(t_1 - t_2)log(e). \tag{71}$$

$$log(B_z{}^2(t_1)) - log(B_z{}^2(t_2)) = 2\gamma(t_1 - t_2)log(e). \tag{72}$$

Here we put $y_1 = log(B_z{}^2(t_1)), y_2 = log(B_z{}^2(t_2))$,

$$y_1 - y_2 = 2\frac{\gamma}{\omega_{pe}}(t_1\omega_{pe} - t_2\omega pe)log(e). \tag{73}$$

$$y_1 - y_2 = 2\bar{\gamma}(\bar{t}_1 - \bar{t}_2)log(e). \tag{74}$$

Hence, the growth rate we used is

$$\bar{\gamma} \equiv \frac{y_1 - y_2}{2(\bar{t}_1 - \bar{t}_2)log(e)}, \tag{75}$$

$$= \frac{y_1 - y_2}{0.868(\bar{t}_1 - \bar{t}_2)}. \tag{76}$$

By using the data show in the figure ,we get

$$= \frac{7.48 - 6.05}{0.868(0.87 - 0.03)} = 0.67. \tag{77}$$

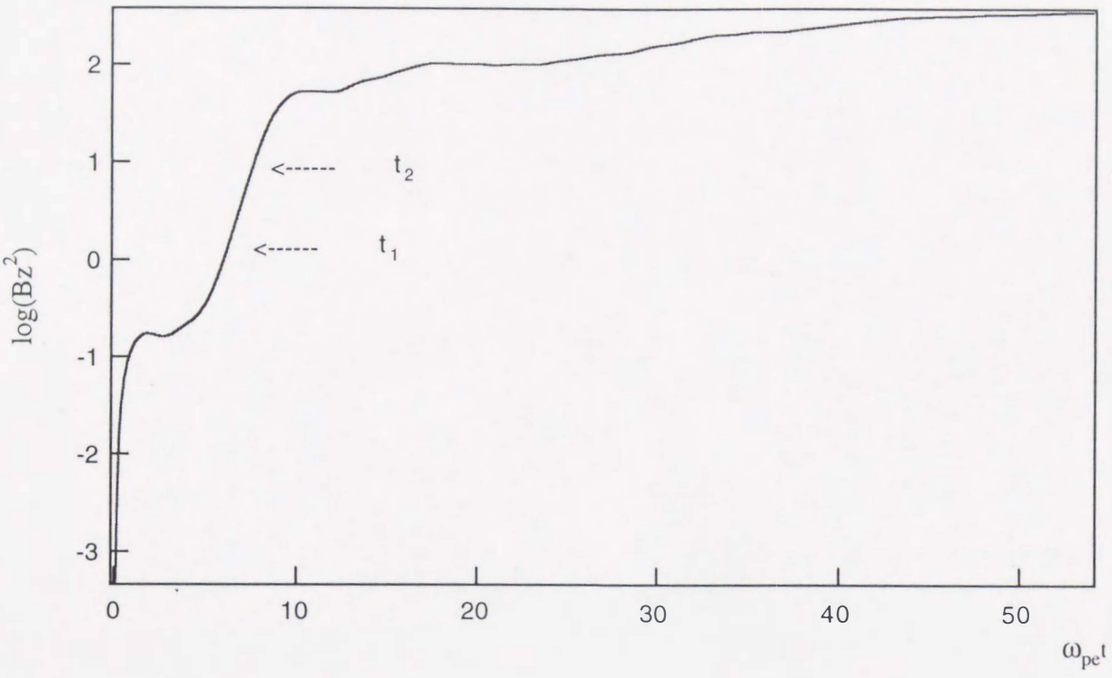

Time history of megnetic field B_z.
t_1=6.05, t_2=7.48
$\log B_z^2(t_1)$=0.03, $\log B_z^2(t_2)$=0.87.

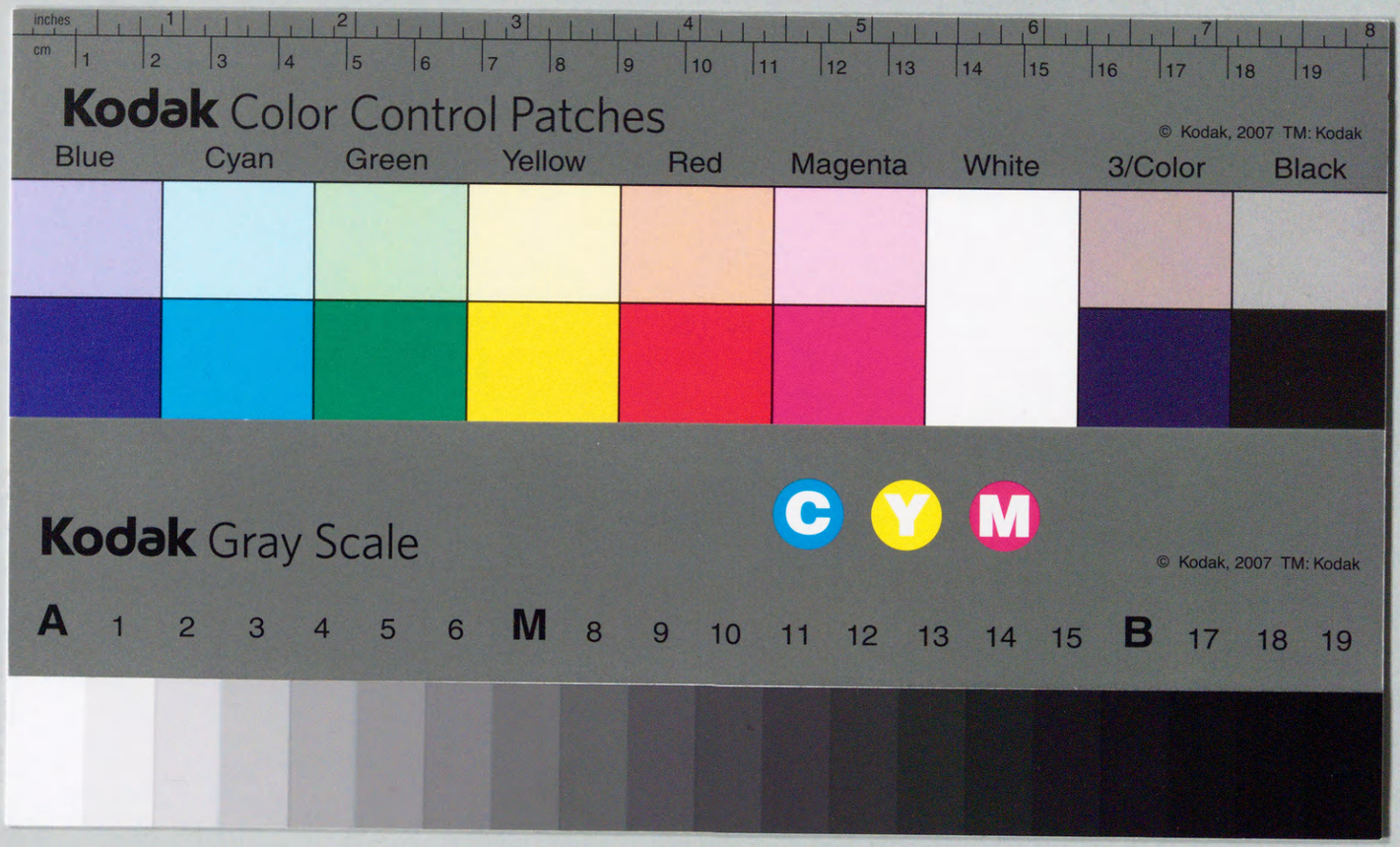
inches
cm
Kodak Color Control Patches
© Kodak, 2007 TM: Kodak
Blue
Cyan
Green
Yellow
Red
Magenta
White
3/Color
Black
Kodak Gray Scale
C
Y
M
© Kodak, 2007 TM: Kodak
A 1 2 3 4 5 6 M 8 9 10 11 12 13 14 15 B 17 18 19